Spin and Density Resolved Microscopy of Hubbard Chains

Martin Boll

München 2016

Spin and Density Resolved Microscopy of Hubbard Chains

Martin Boll

Dissertation
an der Fakultät für Physik
der Ludwig–Maximilians–Universität
München

vorgelegt von
Martin Boll
aus Hachenburg

München, den 21.10.2016

Erstgutachter: Prof. Immanuel Bloch
Zweitgutachter: Prof. Lode Pollet
Tag der mündlichen Prüfung: 22.11.2016

Contents

Zusammenfassung

Diese Dissertation berichtet von der mikroskopischen Untersuchung antiferromagnetischer Ordnung in Hubbard Ketten, die mit ultrakalten, repulsiv wechselwirkenden Fermionen in optischen Gittern realisiert wurden. Durch die Erweiterung eines Quantengasmikroskops um Spin Auflösung, eröffnete sich die Möglichkeit, die komplette Dichte- und Spinstatistik eines stark korrelierten fermionischen Vielteilchensystems auszulesen. Durch Anwendung dieser Technik haben wir antiferromagnetische Korrelationen, die sich über drei Gitterplätze erstrecken, nachgewiesen.

Angefangen mit einer entarteten zwei-komponentigen Mischung von ^{6}Li Atomen, die in einer einzelnen Ebene eines vertikalen Gitters gefangen waren, laden wir die Atome in eindimensionale Subsysteme eines transversalen optischen Supergitters. Durch adiabatisches Anrampen des Gitterpotentials entlang des letzten verbliebenen Bewegungsfreiheitsgrades geht das System in das Regime des stark korrelierten ein-dimensionalen Fermi-Hubbard Hamiltonians über. Anschließend trennten wir die Atome unterschiedlichen Spins räumlich in entgegengesetzte Gitterplätze lokaler Doppelmulden senkrecht zur Gitterrichtung, bevor die Atome mit einzel-Atom und Gitterplatz sensitiv abgebildet wurden. Dadurch konnten wir den Spin jedes einzelnen Gitterplatzes auslesen und Spin-Spin Korrelatoren berechnen. Die zweikomponentigen entarteten Gase wurden mit sub-Poisson Atomzahlfluktuationen hergestellt, und zwar mithilfe von magnetisch unterstützter evaporativer Kühlung in Gegenwart einer Feshbach Resonanz, die benutzt wurde um die Streulänge einzustellen. Die Abhängigkeit der antiferromagnetischen Korrelationen von der Austauschwechselwirkung wurde experimentell untersucht indem die Streulänge zwischen den Atomen vor dem Laden in das optische Gitter eingestellt wurde. Das dem optischen Gitter zugrundeliegende Fallenpotential modellierte die Dichte- und Entropieverteilung, sodass der Einfluss von Dichteanregungen und verschiedenen Entropien auf Spin-Korrelationen gemessen werden konnten. Durch Selektion der Hubbard Ketten, basierend auf deren durchschnittlichen Besetzung und lokalen Atomzahlfluktuationen, konnten Spin Korrelationen, die 58% des vorrausgesagten Wertes im Rahmen des Heisenberg Modells bei $T = 0$ entsprechen, gemessen werden. Durch Vergleich der erhaltenen Korrelationen mit Quanten-Monte-Carlo Vorhersagen für unser System konnte die niedrigste Entropie pro Teilchen von $s = 0.51(4)k_{\mathrm{B}}$ nachgewiesen werden, die damit deutlich unter der für länger-reichweitige Korrelationen notwendigen Entropie von $s = \ln(2)k_{\mathrm{B}}$, liegt. Für Entropien unterhalb dieser kritischen Entropie hängen diese Spin Korrelationen stark von der Entropie des Systems ab, im Gegensatz zu lokalen Dichtefluktuationen. Daher könnte ein solches Spin-Thermometer in der

Zukunft dazu genutzt werden, neuartige Kühlmethoden zu charakterisieren, welche nötig sind, um das Temperaturregime der d-Wellensupraleitung zu erreichen. Der Zugang zur kompletten Atomzahl- und Spinstatistik ermöglicht es uns Multipunkt-Korrelatoren zu berechnen, welche solche exotischen Materiezustände charakterisieren.

Abstract

This thesis reports on the microscopic investigation of antiferromagnetic order in Hubbard chains, realized with ultracold repulsively interacting fermions in an optical lattice. Extending a quantum gas microscope on spin resolution opened the possibility to access the full charge and spin statistics of a strongly correlated fermionic many body system. Using this technique, we measured antiferromagnetic correlations over distances up to three lattice sites.

Starting with a repulsive degenerate two component mixture of ^{6}Li atoms trapped in a single plane of a vertical lattice, we loaded the atoms into one-dimensional tubes of a transverse optical superlattice. By adiabatically ramping up the lattice potential along the tubes, we isentropically entered the strongly correlated regime of the one-dimensional Fermi-Hubbard Hamiltonian. We spatially separated the two spin states into opposite sites of local double wells orthogonal to the direction of the lattice before single atom and site sensitive imaging. In this way we extracted the spin information of every single lattice site and were able to evaluate spin-spin correlations.

The two component degenerate gases were produced with sub-Poissonian atom number fluctuations by magnetically driven evaporative cooling in vicinity of a Feshbach resonance, used to set the scattering length. The dependence of antiferromagnetic correlations on the driving superexchange coupling was experimentally investigated by varying the interparticle scattering length before loading the atoms into the optical lattice. Taking advantage of the underlying trapping potential of the optical lattice, which shaped the filling and the entropy of the gases, the influence of density excitations and different entropies on spin correlations was observed. By post-selecting the Hubbard chains based on their average filling and local atom number fluctuations, spin correlations corresponding to 58% of the zero temperature predictions in the Heisenberg regime were measured. By comparing the obtained antiferromagnetic correlations to Quantum-Monte-Carlo predictions for our system the lowest measured entropy per particle could be stated as $s = 0.51(4)k_{\mathrm{B}}$, clearly below the critical value of $s = \ln(2)k_{\mathrm{B}}$, which is required to form longer ranged correlations.

Below this critical entropy, in contrast to local density fluctuations, these spin correlations strongly depend on the entropy of the system. In the future, such a spin thermometer can be used to benchmark novel cooling techniques, which are required to enter the temperature regime of d-wave superconducting states. The access to the full particle and spin statistics will enable us to read out multi-point correlation functions, which characterize such exotic states of matter.

Chapter 1

Introduction

Many discoveries in solid state physics in recent decades, such as high temperature superconductivity [1], can not be treated within the very successful framework of Fermi-liquid theory [2, 3] anymore. The correlations between the involved electrons are so strong [4] that the description based on weakly interacting quasi-particles breaks down. Among the models [5, 6] which govern the basic physics of these so called strongly correlated materials, the Hubbard model delivers a paradigmatic description of the essential ingredients [7]. The competition of the electrons kinetic energy and their interactions is sufficient to describe quantum many-body phenomena such as the onset of a Mott insulator at a half filled band [8]. When doping the system, despite of its conceptual simplicity, the Hubbard model can not be solved analytically in more than one dimension [9]. Since the Hilbert space of N interacting quantum mechanical particles scales at least as 4^N, which is in stark contrast to the classical particles ($\sim N$), their numerical treatment not only requires enormous resources, but is also limited by the available storage. The simulation of 265 spins needs already more storage than the predicted number of protons in the universe ($\approx 10^{80}$).

Quantum simulation with ultracold atoms

Instead of numerical simulating the system with a classical computer, Feynman proposed to use another quantum system, which can be experimentally accessed more easily, but is governed by the same physics [10]. Although being visionary in 1981, in the recent years ultracold atoms, trapped in optical lattices [11] have been used successfully to mimic the physics of condensed matter materials [12, 13]. The provided experimental platform is clean, flexible and due to the diluteness and the low temperatures of the used gases, it offers timescales of physical processes in the millisecond range. Bose-Einstein condensates of various [14–16] alkali-atomic species offered the basic source of ultracold atomic samples. Loading a repulsively interacting BEC of $^{87}\mathrm{Rb}$ into a cubic optical lattice of varying depth, led to the observation of the superfluid to Mott transition of bosonic particles [17]. In another example, the theoretically predicted Tonks-Girardeau gas in one dimension [18] was experimentally realized by increasing the interparticle

interactions until trapped bosonic particles fermionized [19, 20]. Whereas in these measurements the trapping potential of the system was used to increase the interparticle interactions while reducing their kinetic energy, Feshbach resonances [21] provide the possibility to directly tune the magnitude and the sign of the interparticle scattering length by varying a magnetic field [22]. Since these interactions are van-der-Waals like and therefore short-ranged, recent experimental developments have approached longer-range interactions from different directions. Besides using atomic species with high permanent magnetic moments [23–25], interparticle interactions can be enhanced by inducing a large dipole moment via excitation to Rydberg states [26–28]. Other approaches load ground state polar molecules, providing anisotropic long range interactions, into optical lattices [29–32]. However, this approach still lacks reasonable lifetimes and temperatures at densities which are required to enter the Hubbard-regime. Besides the interparticle interactions, the geometry and the parameters of the trapping potential are other knobs to tune the characteristics of ultracold atomic systems. Tuning the dimensionality, by inhibiting mobility of the trapped particles along a direction, allowed for the observation of the Berezinskii-Kosterlitz-Thouless (BKT) transition [33, 34] in a two-dimensional atomic gas [35]. The use of more complex lattice geometries [36–38] and their excellent control [39–41] enabled the study of non-trivial band topologies with ultracold atoms [42–47].

In contrast to the most of the atomic species which were used to obtain these numerous results, electrons are fermions. After the first realization of a quantum degenerate Fermi gas [48] numerous investigations on ultracold Fermi gases were driven forward, where the BEC-BCS crossover [49, 50] was of central interest. By decreasing the magnitude of the interparticle scattering length of an attractively interacting fermi gas, the system featured a crossover from a Bose-Einstein condensate of tightly bound di-atomic molecules $^6\mathrm{Li}_2$ to Cooper paired weakly attracting independent fermionic $^6\mathrm{Li}$ atoms [51–53]. In the environment of an optical lattice potential, the first fermionic Mott insulators were experimentally probed in 2008. Whereas Schneider et. al probed the macroscopic incompressibility [54], Jördens et. al used the strong global suppression of density excitations [55], to show the transition from a metallic to a Mott insulating state driven by repulsive interactions [8]. Further development of cooling techniques and the control of optical potentials even enabled the first observations of short-range antiferromagnetic correlations [56–58] in optical lattice systems. However, all so far presented investigations dealt with experimental signatures which were obtained from the bulk, very similar to traditional methods used in condensed matter as the determination of heat capacities and susceptibilities. Even though these global measurements have been proven to be extremely powerful, they are lacking the possibility to access local properties as density fluctuations which play an important role in inhomogeneous quantum many body systems.

Quantum gas microscopy

One basic method which is commonly used to observe and distinguish the constituents of a sample, is light microscopy. Even by using the simplest possible setup of a microscope, a single magnifying lens, groundbreaking discoveries as the observation Brownian motion have

been made [59]. Among modern microscopes, one approach is to optically excite the internal electronic structure of the investigated particles or attached markers and collect their emitted fluorescence. Across many fields of natural sciences, this method has been extremely successful. State of the art fluorescence microscopes are able to capture the nanoscale dynamics [60] and measure the temperature of living cells with milli-Kelvin resolution [61]. The technique of fluorescence microscopy has been also applied to image atomic systems, such as trapped single ions [62] and atoms [63, 64] with high fidelity. However, single-atom and site-sensitive detection of dense samples in optical lattices, which allow to explore the regime of strong correlations, came along with certain challenges. Obtaining a sufficient amount of fluorescence by scattering photons on the atoms while keeping them fixed to their original lattice sites is complicated by the small interparticle distance given by the optical lattice. By freezing the atomic distribution in optical lattices as deep as $300\,\mu$K per axis and adjusting the parameters of the scattered photons such that the atoms were cooled at the same time, two groups succeeded to overcome this challenge using bosonic $^{87}\mathrm{Rb}$ atoms [65, 66]. This advance opened the path to detect and manipulate [67] many body systems on the single atom level. The study of density [68] and spin correlations [69, 70], non-local order parameters [71] and entanglement [72, 73] in the Bose-Hubbard model, are only a selection among the achievements of these pioneering setups. To combine the benefits of a quantum gas microscope with the properties of ultracold fermions in optical lattices, many research groups invested a lot of effort. Just in the last year the first *Fermi gas microscopes* succeeded to image sparse and non-degenerate samples of ^{40}K and $^{6}\mathrm{Li}$ [74–77]. By using the local density fluctuations as a measure of temperature [78] to improve the preparation processes, it did not take long until the quantum degenerate regime was entered and strongly correlated fermionic systems as band- [79] and Mott-insulating states [80, 81] were locally studied. In the framework of this thesis, the density resolving *Fermi gas microscope* in [79] was extended about the possibility to read out the full spin statistics of a strongly interacting many-body system of $^{6}\mathrm{Li}$. This opens the route towards future studies of the interplay between spin and charge degrees of freedom in the Fermi Hubbard model, which is expected to contain basic features of high temperature superconductors [4].

Outline

This thesis reports on the observation of antiferromagnetic correlations in Hubbard chains with a novel spin and density resolving quantum gas microscope. The used two dimensional samples of fermionic lithium atoms have entropies low enough to observe correlations extending up to three lattice sites. We prepare and detect these samples by utilizing a superlattice potential. We could benchmark our experimental results on the influence of interparticle interactions by comparison to Quantum-Monte-Carlo predictions, which were done for our system parameters [82]. Based on these theoretical results, the measured spin-spin correlations were used to extract the entropy per particle as well as the temperature of the system. The thesis is structured into six additional chapters:

- Chapter 2 recalls the main ingredients of the Hubbard model and presents its formulation

in the limit of strong interactions. Basic ground-state properties and their dependence on doping are presented. Finally, the peculiarities of one dimensional strongly correlated gases are presented.

- Chapter 3 describes the parts of the experimental setup which are relevant to understand the preparation of one-dimensional Hubbard chains (see chapter 4) and their spin-resolved quantum gas detection. The experimental setup which is required to prepare two-dimensional degenerate gases and investigate them with the quantum gas microscope, is described in [83].

- Chapter 4 informs about the experimental procedure to produce one dimensional Hubbard chains of low entropy. In addition, the calibration of the lattice and interaction parameters are discussed.

- Chapter 5 presents the spin and density resolving quantum gas microscope. The spin detection fidelity is benchmarked.

- Chapter 6 presents the measurements which show antiferromagnetic correlations in one-dimensional systems, extending up to three lattice sites. The experimental results are compared to numerical QMC predictions.

- Chapter 7 summarizes the obtained results and outlooks into future applications of the experimental setup.

The central results of this thesis have been published already:
Spin- and density-resolved microscopy of antiferromagnetic correlations in Fermi-Hubbard chains
M.Boll, T.A. Hilker, G.Salomon, A.Omran, J.Nespolo, L.Pollet, I.Bloch and C.Gross
Science, Vol 353, Issue 6305, (2016)

In addition, the basic experimental setup and the density resolving quantum gas microscope have been used already in:
Microscopic Observation of Pauli-Blocking in Degenerate Fermionic Lattice Gases
A.Omran, M.Boll, T.A. Hilker, K.Kleinlein, G.Salomon, I.Bloch and C.Gross
Phys. Rev. Lett, Vol 115, Issue 263001, (2015)

Chapter 2

The Fermi Hubbard model

This thesis reports the detection of spin correlations at distances larger than three sites in Fermi Hubbard chains [82]. Therefore, the basic theoretical context to understand the emergence of these correlations needs to be given. After general remarks about the origin of the Hubbard model (section 2.1) [9, 84], the simulation of the Fermi Hubbard (FH) models using ultracold fermions trapped in optical lattices is introduced (section 2.1.1) [85]. The mapping of the FH Hamiltonian to two different models describing the low temperature physics, is explained afterwards: the Heisenberg model at half filling (section 2.1.3) and the t-J model when the system is doped (section 2.1.2) [86]. A brief view on the driving force of interactions, the superexchange mechanism [87], is given before focusing on properties which are specific to one-dimensional systems (section 2.2) [88, 89], which are experimentally investigated in chapter 6. The following discussions are based on the given references.

2.1 The Hubbard model: Origin and its limits

First, we review the derivation of the single band Fermi Hubbard model describing fermions trapped in optical lattices to highlight its limits [84]. Assuming non-interacting atoms with mass m and spins σ in a periodic lattice potential $V_{\text{latt}}(\mathbf{r})$ with an underlying trapping potential $V_{\text{trap}}(\mathbf{r})$, the bare single particle Hamiltonian $\hat{\mathcal{H}}_0$ describing the system is given by

$$\hat{\mathcal{H}}_0 = \sum_{\sigma} \int d^3r \, \hat{\Psi}_\sigma^\dagger(\mathbf{r}) \left[-\frac{\hbar^2}{2m}\Delta + V_{\text{latt}}(\mathbf{r}) + V_{\text{trap}}(\mathbf{r}) \right] \hat{\Psi}_\sigma(\mathbf{r}) \ , \tag{2.1}$$

whereas the field operators $\hat{\Psi}_\sigma^\dagger(\mathbf{r})$ and $\hat{\Psi}_\sigma(\mathbf{r})$ create and annihilate an atom with spin σ at position $\mathbf{r}$, respectively. To reduce the kinetic energy (first term), the atoms tend to delocalize within the system. However, when adding interactions the situation changes. A corresponding interaction Hamiltonian $\hat{\mathcal{H}}_{\text{int}}$ which breaks the single particle picture can be written as

$$\hat{\mathcal{H}}_{\text{int}} = \frac{g}{2} \sum_{\sigma,\sigma'} \int d^3r \, \hat{\Psi}_\sigma^\dagger(\mathbf{r}) \hat{\Psi}_{\sigma'}^\dagger(\mathbf{r}) \hat{\Psi}_{\sigma'}(\mathbf{r}) \hat{\Psi}_\sigma(\mathbf{r}) \ , \tag{2.2}$$

with the parameter g, which parametrizes the strength of the interactions. Repulsive interactions favor the opposite behavior as the single particle Hamiltonian: it becomes more favorable to localize the atoms on different sites of the lattice, to minimize their interaction energy. The competition of those two energy scales gives rise to strongly correlated phases. Expansion of the field operators in terms of localized Wannier states [90] $w_{(n)}(\mathbf{r}-\mathbf{r}_j)$ and restricting the this evolution only to the ground band, one can express the field operator in terms of an operator $c^\dagger_{j,\sigma}$ which creates a fermion of spin σ at site j [1]

$$\hat{\Psi}^\dagger_\sigma(\mathbf{r}) = \sum_j w_0^*(\mathbf{r}-\mathbf{r}_j)c^\dagger_{j,\sigma} \ . \tag{2.3}$$

Using equation 2.3 together with the fermionic commutation relations the Hamiltonian is reduced to

$$\hat{\mathcal{H}} = -\sum_{ij\sigma} t_{ij}c^\dagger_{i\sigma}c_{j\sigma} + \frac{1}{2}\sum_{\sigma\sigma'}\sum_{ijkl} U_{ijkl}c^\dagger_{i\sigma}c^\dagger_{j\sigma'}c_{k\sigma'}c_{l\sigma} + \sum_{i\sigma}\epsilon_i n_{i\sigma} \ , \tag{2.4}$$

where $n_{i\sigma} = c^\dagger_{i\sigma}c_{i\sigma}$ is the number of particles on site i. The different terms of the Hamiltonian will be described in the following.

- **Tunneling:** t_{ij} denotes the kinetic energy a particle saves when it hops from site i to j. It is expressed as the matrix element of the kinetic energy operator with respect to the Wannier states of two lattice sites:

$$t_{ij} = -\int d^3r\, w^*(\mathbf{r}-\mathbf{r}_i)\left[-\frac{\hbar^2}{2m}\Delta + V_{\text{latt}}(\mathbf{r})\right] w(\mathbf{r}-\mathbf{r}_j) \ . \tag{2.5}$$

  Whereas in the limit of deep optical lattices the nearest neighbor hopping term dominates, the sum in equation 2.4 only considers adjacent sites i and j. Under the assumption of a simple one-dimensional lattice with spacing a_L and expanding the localized Wannier states in the delocalized Bloch basis [91], one can express the dispersion relation of the ground band as [90]

$$E_q = -2t\cos(q\cdot a_\text{L}) \ , \tag{2.6}$$

  where q is the quasimomentum. In the tight binding limit, the tunneling-element t is therefore connected with the width $\mathcal{W}$ of the ground band

$$\mathcal{W} = E_{\pm\hbar k} - E_0 \approx 4\mathcal{D}t \ , \tag{2.7}$$

  with the dimensionality $\mathcal{D}$ of the system.

- **Interactions:** The temperature regime of ultracold atoms allows us to restrict the interparticle interactions to s-wave scattering processes, being parametrized by the s-wave

[1] I restrict myself here to the fermionic operators, since we only use fermions in our system. The same expansion can be done using bosonic operators, obeying bosonic commutation relations.

scattering length a_s [92]. Since the maximal investigated value was on the order of $a_s \approx 900\, a_B = 47$,nm [2], the interaction on a lattice with a spacing of $a_{\mathrm{L}} = 1.15\,\mu$m can be assumed to act only on-site. Therefore they can be expressed by the product of the integrals of the local state densities along the lattice axes x_i: [3]

$$U = g \prod_i \int dx_i |w(x_i)|^4 \ . \tag{2.8}$$

- **Trapping potential:** The curvature of the trapping potential V_{trap} is given by the waist of the laser beam producing it. Since the beam waists of our lattices ($\approx 125\,\mu$m) are much larger than the extension of a single lattice site ($a_L = 1.15\,\mu$m), the trapping potential within a single lattice site can be assumed to be constant. Using the orthogonality of Wannier states of different sites i and j, the energy offsets due to the trapping potential are simply given by the potential evaluated at the respective lattice site i

$$\epsilon_i = \int d^3r\, |w(\mathbf{r} - \mathbf{r}_i)|^2 V_{\text{trap}}(\mathbf{r}) \approx V_{\text{trap}}(\mathbf{r}_i) \ . \tag{2.9}$$

  The influence of the trapping potential on the density distribution is covered in the next chapter.

2.1.1 The Fermi Hubbard model

For fermionic interacting particles, with spins $\sigma \in \{\uparrow, \downarrow\}$, trapped in a lattice potential, the Hamiltonian (2.4) in a single band of the optical lattice reduces to:

$$\hat{\mathcal{H}} = -t \sum_{\langle i,j\rangle,\sigma} (c^\dagger_{i,\sigma} c_{j,\sigma} + h.c.) + U \sum_i \hat{n}_{i,\uparrow}\hat{n}_{i,\downarrow} + \sum_{i,\sigma} \epsilon_i \hat{n}_{i,\sigma} \tag{2.10}$$

The kinetic energy is reduced when the particles delocalize. Contrary, paying interaction energy is avoided by localizing the particles and therefore minimizing their overlap. Two fermions with the same spin cannot populate the same lattice site in the same energy band due to Pauli's exclusion principle, are not included in the Hamiltonian because of its single band character. These excitations are anyway strongly suppressed since the temperature of the investigated systems are lower than the energy gap between the ground and the first excited band. For fermions, the interaction parameter g and the s-wave scattering length a_s are related as:

$$g = \frac{4\pi\hbar^2 a_s}{m} \tag{2.11}$$

Experimentally we are able to control the sign and magnitude of the scattering length via Feshbach resonances [22], by tuning a magnetic offset field. By changing the lattice depth, all three

[2] For larger scattering lengths we observed strong three body losses outside the lattice phase.

[3] For a separable Hamiltonian the 3D Wannier function reduces to the product of 1D Wannier states.

terms are affected: The kinetic energy and the interaction energy of the particles by tuning the overlap of the wavefunctions with the localized Wannier-states and the site-to-site energy offset since changing the lattice potential also changes the external confinement V_{trap}.

Since the lattice potentials along the different directions can be tuned independently we are also able to change the dimensionality $\mathcal{D}$ of the system. For very strong lattice potentials in one direction, the tunneling coupling along this direction is strongly suppressed and particles will behave like a system of reduced dimensionality. These experimental knobs give us the possibility to explore large parts of the phase diagram of the Fermi-Hubbard Hamiltonian which is schematically depicted in figure 2.1 [4, 85, 93, 94].

By checking the symmetry properties of the Fermi Hubbard Hamiltonian one can already learn a lot about the contained physics. The Hamiltonian fulfills a particle-hole symmetry, which can be easily shown by the invariance of kinetic and interaction energy under the transformation [88]:

$$c_{i,\sigma} \rightarrow (-1)^i \, c^\dagger_{i,\sigma} \tag{2.12}$$

Therefore it is enough to investigate the phase diagram for either hole or particle doping since the physics does not change. By only applying the particle-hole transformation to a single spin, only the kinetic energy is invariant, but the interaction U switches its sign. This effectively maps the charge sector onto the spin sector and changes the interactions from repulsive to attractive.

Repulsive interactions

In the following, the transitions are described, from the metallic to the Mott-insulating state and by further lowering the temperature (entropy), to the Antiferromagnet (AFM, Néel state) in the case of a 3D system and a half filled band. Aspects of doped antiferromagnets will be described in the framework of the t-J model (2.1.2).

- **Metal to Mott-insulator:** For large temperatures (large T/t and $T > U$) the system is metallic according to band theory [95]. The atoms are delocalized and the thermal energy is the dominant energy scale. When lowering the temperature of the system and tuning the interaction energy U on the order of the bandwidth $4t\mathcal{D}$, the system undergoes a crossover to the paramagnetic Mott-insulator state. Charge excitations of the system are suppressed by the interaction energy gap U, which is to be overcome to create a doubly occupied site. For a trapped system, the potential shape can lead to coexistence of these three phases. In the wings of the system $n_{\text{tot}} = (n_{i,\uparrow} + n_{i,\downarrow}) < 1$ the system is metallic, surrounding a Mott-insulating disk, fulfilling $n_{\text{tot}} = 1$. If the number of particles is large enough that the offset energy by the trapping potential is higher than the interaction energy U, atoms can tunnel to the center of the trap, causing double occupancies ($1 < n_{\text{tot}} < 2$). For a central density of $n_{\text{tot}} = 2$ the system is band insulating as already mentioned. To sum up, the sufficient requirements to form a Mott-insulating states in a trap are:

$$k_{\text{B}}T < U \ , \ 4t\mathcal{D} < U \ , \ \epsilon_i < U \ : \ \text{U is the dominant scale} \tag{2.13}$$

$$U < \text{Bandgap} \ : \ \text{Single band physics} \tag{2.14}$$

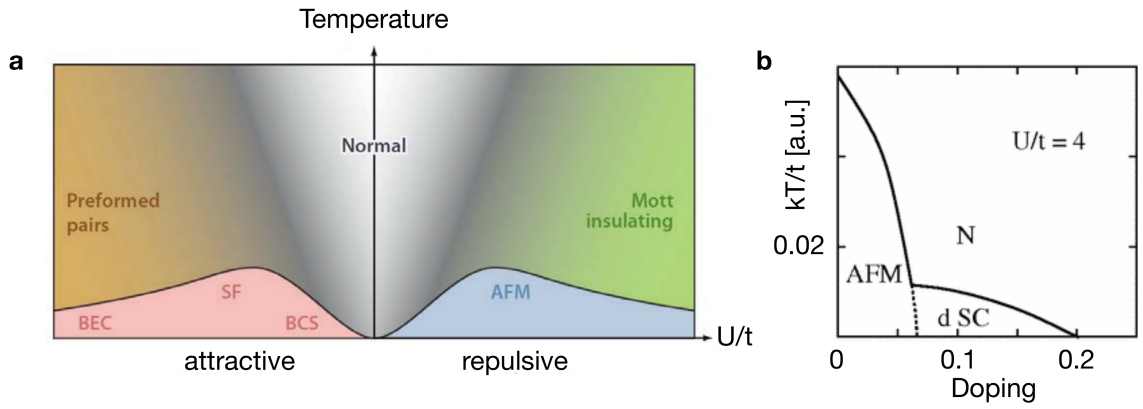

Figure 2.1: **Phase diagrams of the for the Fermi-Hubbard model(a)** Schematic phase diagram of the 3D Fermi Hubbard model on a simple cubic lattice for the case of half filling (adapted from [85]). In the case of interacting free systems, the system shows a normal, metallic behavior over the entire temperature range, except $T = 0$. For strong repulsive interactions and T on the order of the bandwidth of the lowest band, the system features a crossover to the Mott-insulating regime [8]. When lowering the temperature, antiferromagnetic order starts to emerge. For attractive interactions ($U < 0$, $|U| > \mathcal{W}$) on average atoms are favored to form pairs (preformed pairs). Since the temperature in this regime is still too high, the local density fluctuates strongly. However, when the temperature is lowered the situation changes. For strong attractive interactions strongly bound pairs can be regarded as repulsively interacting hard-core bosons, which condense below temperatures on the order of $t^2/|U|$ (BEC), corresponding to the tunneling energy of a pair. For weak interactions ($U < t$) the atoms are delocalized within the lattice and can be described in the BCS picture [50]. **(b)** Phase diagram of moderately repulsively interacting ($U/t = 4$) ^{6}Li atoms trapped in a 2D-lattice for different concentrations of doping (adapted from [93]). When increasing the fraction of particle excitations in a antiferromagnet (AFM) the spin order is destroyed. However, for temperatures $k_\mathrm{B}T < 0.02t$ and a fraction of doping between 7% and 20% the Fermi-Hubbard model features a d-wave superconducting state [4].

- **Mott insulator to antiferromagnet:** By lowering the temperature of the system even more also the entropy of the system decreases. Hopping processes can't be handled in first order perturbation theory($\propto t$), since the subset of single occupancies would be left. In second order perturbation theory ($\propto t^2$), virtual tunneling processes lift the degeneracy of the system [96]. In case of two sites, a spin singlet is the ground state, gaining energy of $-3/4J_\mathrm{ex}$ by anti-parallel spin alignment. The exchange coupling J_ex is given by [87]

$$J_\mathrm{ex} = \frac{4t^2}{U} \quad . \tag{2.15}$$

For larger systems the ground state is called the antiferromagnet (AFM) or Néel state. The transition temperature to observe the AFM phase is therefore on the order of the superexchange constant $k_{\mathrm{B}}T_{\mathrm{AFM}} \approx J_{\mathrm{ex}}$. The non-linear dependence on U/t explains the maximum of the transition temperature for moderate values of U/t in figure 2.1 **(a)**. In the limit of strong interactions, the system is fully driven by spin-exchange coupling J_{ex} which itself gets smaller for increasing interactions. In stark contrast, for very low interactions the system features also charge excitations, which lead to reduced spin-correlations. For intermediate interactions spin correlations are maximally robust against temperature. Since even for half filling the exact ground state properties of the Fermi Hubbard Hamiltonian can't be analytically assigned besides for one-dimensional systems, powerful numerical methods were developed and used to calculate transition temperatures T_{AFM} which are required to reach the antiferromagnetic state.[4].

Whereas the onset of these states was so far discussed in the language of temperatures, the valid assumption of treating atoms in optical lattices as a closed system, allows to use the entropy. Generally, the entropy of a system described by a density matrix ρ can be obtained via [98]

$$S = -k_{\mathrm{B}}\,\mathrm{tr}(\rho \ln(\rho)) \quad . \tag{2.16}$$

One can gain a lot of information about a Hubbard system by calculating the entropy per particle and lattice site. These calculations, already performed in [99], are repeated in the following for the case of infinitely strong repulsive interactions between the two spin components. The density matrix of the system is diagonal within the Hilbert space of holes $|0\rangle$, singly occupancies of up-spins $|\uparrow\rangle$ or down-spins $|\downarrow\rangle$ and doublons $|\downarrow\uparrow\rangle$:

$$\rho = p_h \left|0\right\rangle \left\langle 0\right| + p_s \left(\left|\uparrow\right\rangle \left\langle\uparrow\right| + \left|\downarrow\right\rangle \left\langle\downarrow\right|\right) + p_d \left|\downarrow\uparrow\right\rangle \left\langle\downarrow\uparrow\right| \tag{2.17}$$

Since the Hilbert space has four dimensions $\mathcal{D} = 4$ the maximal entropy per site $s = S/N_{\mathrm{latt}}$ is limited to $s_{=}k_{\mathrm{B}}\ln(4)$. However, for certain fillings the strong repulsion reduces the Hilbert space even more, by zeroing the probabilities p_i of some configurations to occur. If the filling is smaller than one half $n_\sigma \leq 0.5$, doublon excitations are not present, whereas for larger fillings ($0.5 < n_\sigma \leq 1$) every lattice site is singly or doubly occupied. Then the double occupied fraction scales as $p_{\mathrm{d},n>0.5} = 2 - \frac{1}{n_\sigma}$ with the filling. Away from the special cases of zero-,half- and full filling the maximum entropy per site is therefore $s = k_{\mathrm{B}}\ln(3)$. At zero (full) filling only holes (doublons) are permitted, and the entropy per site vanishes. Even though only singly occupied sites are allowed at half filling, the entropy capacity per site does not vanish, since this configuration is reached by placing either a up-spin or a down-spin. Therefore the maximum entropy capacity per lattice site is $s = k_{\mathrm{B}}\ln(2)$. The strong influence of the interactions on the probabilities p_i is a central aspect of strongly correlated systems. The entropy capacity per particle $s^* = S/N_{\mathrm{at}}$ is defined by normalization to the number of particles among which the total entropy can be distributed. The behavior of both magnitudes over the entire range of

[4] In three dimensions the maximum transition temperature $T_{\mathrm{AFM}}/t = 0.33$ was located for $U/t = 8$ [97])

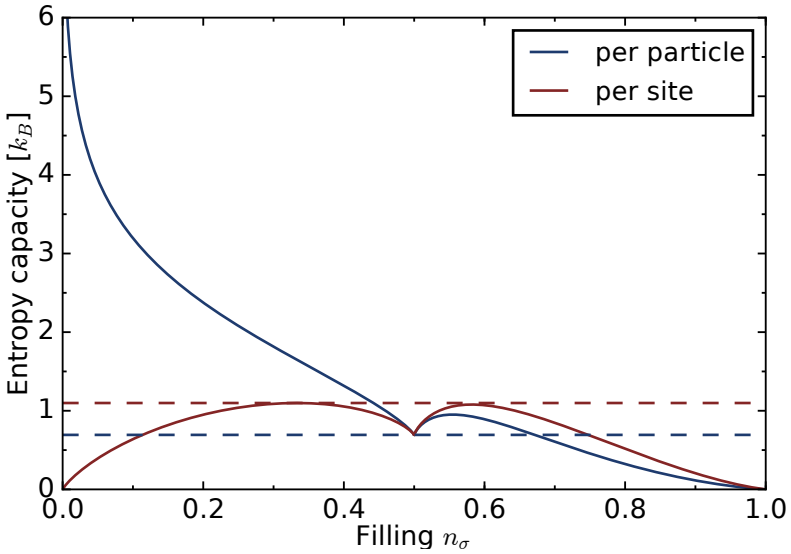

Figure 2.2: **Entropy capacities for infinitely strong repulsive interactions** The red curve represents the entropy capacity per lattice site $s = S/N_{\text{latt}}$ for different filling fractions n_σ per spin state σ. The blue curve describes the entropy per particle $s^* = S/N_{\text{at}}$. The dashed lines indicate $S = k_{\text{B}}\ln(2)$ (blue) and $S = k_{\text{B}}\ln(3)$ (red).

fillings from zero to one is shown in figure 2.2. For a Mott insulator the capacities per site and per atom are equal to $s = k_{\text{B}}\ln(2)$. However, the entropy per particle can be lower than this value when the interaction of the spins energetically favors their alignment. When placing an atom on a lattice site, its spin is not random anymore but depends on the spin of the atom on a neighboring site. This gives an intuitive picture why spin correlations onset for entropies per particle below $s^* \leq k_{\text{B}}\ln(2)$. The remaining entropy is stored in the spin-degrees of freedom. Experimental realizations have used this effect to cool a gas by storing more entropy in the spin degree by enlarging the number of spin states [100].

For a trapped system, the filling of the system is shaped by the trapping potential $V_{\text{trap}}(r)$ relative to the interactions U. This has also consequences on the distribution of the entropy in the trap. The filling of a lattice $n_i\,(T, \mu_i)$ site i is governed by an adapted Fermi-Dirac distribution taking the local chemical potential μ_i and the interactions into account [101]

$$n_i\,(T, \mu_i) = \sum_\sigma n_{i,\sigma} = \frac{2e^{\mu_i/T} + 2e^{(2\mu_i - U)/T}}{1 + 2e^{\mu_i/T} + e^{(2\mu_i - U)/T}} \quad , \tag{2.18}$$

where the local chemical potential is given in the local density approximation (see equation 2.9) by

$$\mu_i = \mu_0 - V_{\text{trap}}(r_i) \quad . \tag{2.19}$$

When combining the shaped filling with the dependence of the entropy per particle on the filling

(blue curve in figure 2.2) it follows that an atom at the edge of a trapped cloud, where the filling is low, carries more entropy compared to one in the center. Intuitively, an atom in these regions can choose among many empty lattice sites which are not blocked by the interaction energy. The total entropy of the system S which is linked to the systems' temperature T is distributed among the atoms depending on the average filling $s^*(T, n_i(r))$. The distribution of the entropy allowed people to produce and probe first fermionic Mott-insulators [54, 55] or short range antiferromagnetism [56, 57] in an optical lattice, even though the average entropies per particle within the systems were too high. They all relied on global measurement signals which are affected by these high entropy regions at the edges of the samples. However, with a quantum gas microscope we can probe these systems locally and discriminate the signals depending on the local entropy. In addition, the non-uniform entropy distribution has triggered an enormous amount of proposals to use this effect for novel cooling techniques [101, 102].

Attractive interactions

For negative U, the interaction energy favors pairwise occupation of lattice sites with two atoms of opposite spins. Again, the competing energy scale is the kinetic energy, which tends to delocalize the atoms. The physics of attractive interacting fermions on a lattice is linked to the repulsive regime via a canonical Bogoliubov transformation [86, 103]:

$$c_{i,\uparrow} \rightarrow \tilde{c}_{i,\uparrow} \tag{2.20}$$

$$c_{i,\downarrow} \rightarrow \tilde{c}^{\dagger}_{i,\downarrow} \tag{2.21}$$

This transformation maps $U \rightarrow -U$ while keeping $t \rightarrow t$. This symmetry of the Hubbard Hamiltonian explains the symmetric phase diagram 2.1. The behavior of the spin degree of freedom in the repulsive case, as the transition to AFM order, is in strong correspondence to spatial ordering of the charge degree of freedom for attractive interactions. For high temperatures ($k_{\mathrm{B}}T > U$) and weak interactions ($U < t$) the atoms are described by a metallic state. When increasing the interactions and for sufficiently low temperatures ($k_{\mathrm{B}}T < U$) pairing two atoms with opposite spin becomes energetically favorable. These preformed pairs can be described by a disordered charge density wave, showing no spatial ordering. However, when lowering the temperature of the system even further ($T_{\mathrm{cdw}} \sim 4t^2/|U|$), the pairs a strongly bound with respect to any energy scale in the system and can be described as composite hard-core bosons, which condense to a BEC. Since the pairs are repulsively interacting and the filling is one half, the pairs localize on every second lattice site. This transition has its correspondence at repulsive interactions in the spin sector, when the spins of a Mott insulator antiferromagnetically order.

For weak attraction ($|U| < 4\mathcal{D}t$) the atoms are delocalized on the lattice and can still be described by BCS theory [50] as in the free-space. The link between repulsive and attractive interactions, also shows up when doping the system. It was mentioned already, that a doped antiferromagnet is believed to provide d-wave superconductivity. Correspondingly for attractive interactions, a spin doped superfluid (spin imbalance) supports d-wave superfluidity [103]. The observation of these spatial ordered charge density wave is exacerbated by the an underlying

trapping potential of the optical lattice potentials. Whereas repulsive interactions counteract the trapping potential, which favors occupation the in center, attractive interactions even favor doubly occupied sites. Instead of an ordered charge density wave just a band insulating state of pairs in the low entropy region of the trap would be observed. Flattening the potential by using a blue detuned lattice [104] or direct implementation of box-like uniform potential [105] could overcome this limitation in the future, enabling the study of attractively interacting fermions in optical lattices [103].

2.1.2 The t-J model

The above given qualitative arguments apply nicely to the cases of perfect half-filling. Due to the non-uniform density distribution and finite entropies in the system the occurrence of holes and doubly occupied sites can not be suppressed completely. The influence of holes on a antiferromagnetic state is widely under debate and one of the candidates of the basic principles of high temperature superconductivity, see figure 2.1 **b**, [93]. By inducing a single hole into a two-dimensional system the ground state properties can change dramatically. For infinite strong interactions the ground state of this system is ferromagnetic, proven in Nagaokas theorem [106], in contrast to the half-filled case, where an antiferromagnet driven by superexchange interactions is the ground state. An intuitive picture is given in figure 2.3. The derivation of the t-J model from the Fermi Hubbard Hamiltonian follows an idea which was used to obtain an expression for the superexchange coupling in equation 2.15. A very detailed description is given in [108]. Given a uniform system, in the limit of strong interactions U, the hopping t is treated in perturbation theory. If one allows holes and double occupancies the Hilbert space is larger compared to the case of half filling. A hopping event can couple the two population subsets. Perturbation theory is stopped after the second order. The resulting effective Hamiltonian $\mathcal{H}_{\text{t-J}}$ is the sum of three different contributions [86]

$$\mathcal{T} = -\sum_{ijs} t_{ij} c_{is}^{\dagger} c_{js} \tag{2.22}$$

$$\mathcal{H}_{\text{QHM}} = \frac{1}{2}\sum_{ij} \frac{4t_{ij}^2}{U}\left(\mathbf{S}_i \cdot \mathbf{S}_j - \frac{n_i n_j}{4}\right) \tag{2.23}$$

$$\mathcal{J}' = \frac{1}{2U}\sum_{ijk}^{i\neq k} t_{ij} t_{jk} \left[\sum_s \left(c_{is}^{\dagger} c_{ks} n_j\right) - c_i^{\dagger}\vec{\sigma} c_k \cdot c_j^{\dagger}\vec{\sigma} c_j\right] \quad , \tag{2.24}$$

where the spin operators $\mathbf{S}_i$ are linked to the fermionic field operators and the Pauli-matrices $\vec{\sigma}$ via

$$\mathbf{S}_i = \frac{1}{2}\sum_{ss'} c_{is}^{\dagger}\vec{\sigma}_{ss'} c_{is'}. \tag{2.25}$$

The first term describes hopping events in the subspace of singly occupied sites and holes. An atom can hop from a site j to an empty site i. The second term describes the full kinetic

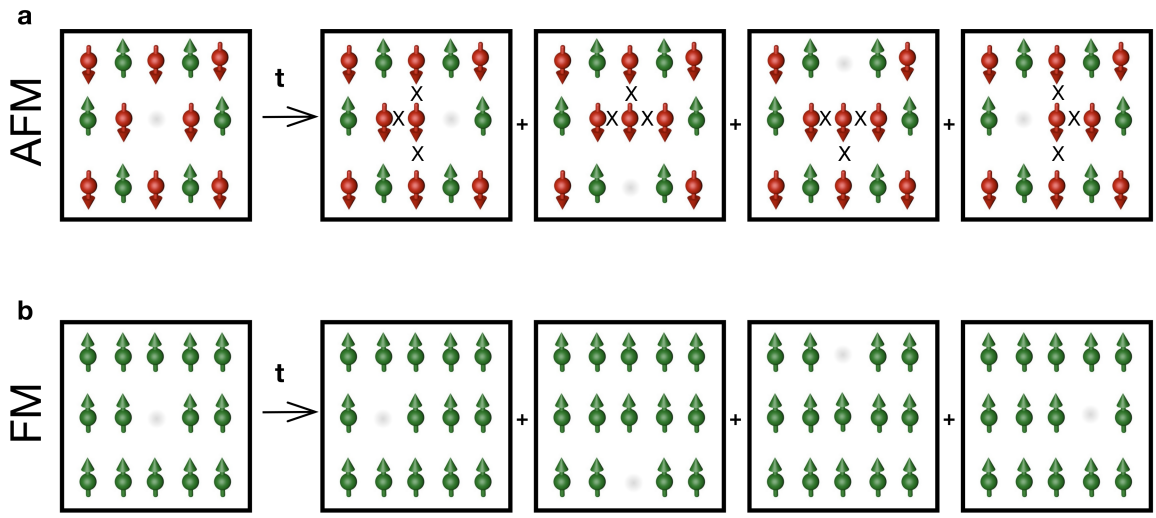

Figure 2.3: **Influence of a hole onto ground-state properties(a)** Assuming an antiferromagnetic background a hole can not reduce its kinetic energy by delocalizing, without breaking antiferromagnetic bonds. In the illustrated case of two dimensions, the hole has four neighboring sites to which it can delocalize to reduce the kinetic energy. If the atom tunnels it would break three antiferromagnetic bounds, increasing the energy by $3J_{\text{ex}}$. **(b)** In case of a ferromagnetic background the hole can reduce its kinetic energy by delocalizing, since the ferromagnetic background persists. Holes favor ferromagnetic environment. A semi-classical version of the t-J model describes a hole in antiferromagnetic background as a spin-hole polaron [86, 107].

exchange path driven by the superexchange mechanism. The third term contains three site hopping processes. Either tunneling processes occur and the involved atoms persist their spin, or the spin is flipped, dependent on the (spin-)population of the third site. For exactly half filling the first and the third term cancel and the Hamiltonian reduces to the Heisenberg model, which will be discussed in the next subsection. A hole which is circumvented by $\mathcal{Z}$ number of sites, can gain the kinetic energy $\mathcal{Z}t$ by delocalizing among these sites. In the regime $U/t >> 1$, where tunneling dominates the superexchange $t > J$, this effect can not be neglected. As depicted in figure for a 2D system 2.3, a tunneling event would destroy three antiferromagnetic bounds, increasing the energy of the system by $+3J_{\text{ex}}$. A semi-classical treatment of a single hole in a half filled system [107] illustrates the behavior in two dimensions ($\mathcal{Z} = 4$). For $1 < t/J_{\text{ex}} < 4$, corresponding to interactions of $1 < U/t < 4$, the hole can be treated as a localized five-site polaron. The excitation in the charge degree of freedom is localized and effects the spin degree of freedom in its environment $R \sim (t/J_{\text{ex}})^{1/4}$. For infinite interactions $U = \infty$, this radius tends towards infinity, revealing the Nagaoka limit. In this limit, it costs no energy anymore to excite a spin degree of freedom, the spins are fully polarized to delocalize the hole among the whole system. Note, that this behavior changes in one-dimensional systems

[109, 110], as will be pointed out in section 2.2.

2.1.3 The Heisenberg model

As already mentioned, the Heisenberg model is contained in the t-J model for the case of half filling and repulsive interactions, which are so strong that the charge degree of freedom can be assumed to be frozen. The spins of the trapped particles play the major role within the system. Since the t-J model itself was formulated from the Fermi-Hubbard model in the regime of strong interactions, it seems intuitively consistent that there exists a direct mapping of the Fermi-Hubbard Hamiltonian onto the Heisenberg Hamiltonian. The Heisenberg model describes the interaction of spins $\mathbf{S}_i$ and $\mathbf{S}_j$ driven by a coupling J [86]:

$$\mathcal{H} = J \sum_{i,j} \mathbf{S}_i \cdot \mathbf{S}_j \tag{2.26}$$

For a negative coupling $J < 0$ the Hamiltonian supports a ferromagnetic ground state, whereas for positive coupling ($J > 0$) the spins on neighboring sites are favored to anti-align. By assuming the single band Fermi-Hubbard model (see equation 2.10) in the case of half filling and strong repulsive interactions, which restrict the occupation to singly occupied sites, the Hamiltonian can be mapped on a spin-$1/2$ version of equation 2.26 with antiferromagnetic interactions $J = J_{\text{ex}} = 4t^2/U$.

2.2 One dimensional systems

All experimental results presented in chapter 6 were obtained in one-dimensional Hubbard chains. Since the reduced dimensionality comes with some specialties, it is worth to recapitulate them here very briefly (see section 2.2.1). The interested reader is recommended to the summary about one dimensional systems by T.Giarmachi [88]. In addition results of Quantum-Monte-Carlo simulations of one-dimensional systems and their possible use as a thermometric tool are presented (section 2.2.2). More detailed informations about the Monte-Carlo simulations, which were kindly provided by the group of Prof. Lode Pollet, can be found in the appendix 7 and the supplementary material of our publication [82].

2.2.1 Peculiarities of one-dimensional systems

A major difference between one- and two-/three dimensional systems of interacting particles is their response on excitations. Assuming a chain of interacting atoms, a movement of a single atom will affect all other components due to the interactions. Therefore, even for small interactions a Fermi-liquid description [2] does not apply. These collective excitations were successfully treated in a Tomonaga-Luttinger liquid (TL) description [111–113]. The TL model handles the collective response to excitations as charge (holon) and spin-waves (spinon), which independently spread throughout the system due to their different velocities. The independence of these two excitations, also known as spin-charge separation [88, 112], is in stark contrast to the Bogoliubov quasiparticle description in higher dimensions, which carry both, spin and charge. The spin-charge separation has important consequences for excitations in antiferromagnetic environments, as considered in two dimensions in section 2.1.2 and figure 2.3. Another specialty of one dimensional systems is the absence of long range-order even at zero temperature. For finite temperatures $T > 0$ the Mermin-Wagner theorem proofs the absence of long-range correlations for $\mathcal{D} \leq 2$ [114]. Any small thermal excitation destroys the long range order. For $\mathcal{D} = 1$ the absence of long range order even applies for absent thermal excitations [86].

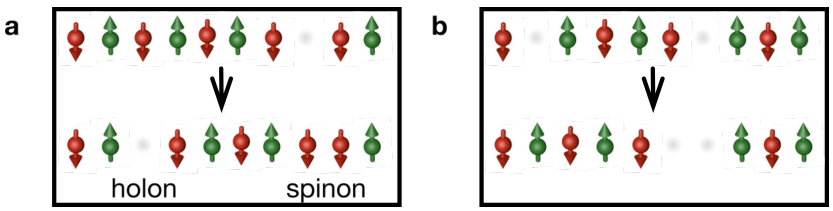

Figure 2.4: **Excitations in one dimension a** Spin- charge separation. An excitation (top row) consists of spin and charge degree of freedom which spread independent of each other in the environment. **b** Spatial condensation of holes for large J_{ex}. For two holes, the energy cost by breaking antiferromagnetic bounds, corresponds to $4J_{ex}$ for separated holes and $3J_{ex}$ if the holes accumulate in the same spatial region.

Since the one-dimensional Hubbard model can be solved analytically via Bethe-ansatz, correlation functions can be calculated. The spin-spin correlations are found to decay algebraically [115, 116].

2.2.2 Using spin correlations as a thermometer

In general, thermometry of atoms which are trapped in optical lattices is much less experimentally investigated than its counterpart for harmonic trapped systems in absence of a lattice potential. In the latter case, a fermionic sample is released from the trapping potential and its temperature can be extracted by fitting the cloud size with a Fermi-Dirac distribution [117]. From the steepness of the Fermi-edge the degree of degeneracy of the sample can be deduced. For fermions in an optical lattice with an underlying trapping potential, the obtained momentum distribution after release from the trapped is dominated by the trapping potential rather than its temperature [118]. One method to estimate the temperature of a system used the number of detected doublons for known repulsive interaction energies, allowing to set an upper bound on the temperature of the system [55]. However, even though this approach used a local quantity, it was measured globally and therefore averaged among the coexisting phases in the inhomogeneous sample. Recent experimental efforts which repeated the same type of experiments with enhanced optical resolution and methodology to detect the doublons was able to characterize the temperature of fermions in an optical lattice via the fluctuation dissipation theorem [78], which relates local fluctuations with global thermodynamic properties as the compressibility of the system. However, in contrast to these local particle number fluctuations which show only a very weak dependence on the temperature once the regime of quantum magnetism is reached, spin correlations show a strong dependence on the temperature and entropy of the system [119, 120]. As already mentioned and will be shown in section 5, our spin and density resolved quantum gas microscope is able to reconstruct the full number and spin statistics. This makes it feasible to probe the relative local entropies in our systems without perfect knowledge of the trapping potential. Sciollia et. al presented a phenomenological model to describe fermions in one-dimensional systems, which will be used in the following to described evolution of charge and spin degree of freedoms for various interactions and entropies, obtained with QMC. The charge density in the system is defined as the sum of the total atom density:

$$\rho = \hat{n}_\uparrow + \hat{n}_\downarrow \quad . \tag{2.27}$$

In contrast the spin operator along the z-projection is the difference of the spin occupations:

$$S^z = (\hat{n}_\uparrow - \hat{n}_\downarrow) \quad . \tag{2.28}$$

In one dimension any small repulsive interaction is sufficient to drive the system being Mott insulating. The charge gap Δ_C is in this case exponentially small:

$$\Delta_C \sim \exp(-t/U) \quad \text{for} \;\; U/t << 1 \tag{2.29}$$

In the limit of strong interactions the charge gap is linear proportional to the interaction energy U, such that any charge fluctuations in the system are strongly suppressed given sufficiently low temperatures. In the limit of very strong interactions $U/t \approx 10$ and half filling the system can be again mapped onto a Heisenberg model, which was already mentioned as a special case of the t-J model in three dimensions 2.1.2. Due to spin- charge separation, the system is described by a Hamiltonian which sums of the ground state Hamiltonian E_{GS} with the spin $\mathcal{H}_s$ and the charge part $\mathcal{H}_c$, all being independent. The spin Hamiltonian

$$\hat{\mathcal{H}}_s = \sum_{\sigma,k} \epsilon_s(k) \hat{s}^\dagger_\sigma(k) \hat{s}_\sigma(k) \tag{2.30}$$

is described by a linear gapless dispersion relation $\epsilon_s(k) = \hbar v_s |k|$ with spin velocity v_s. The operators $\hat{s}_\sigma(k), \hat{s}^\dagger_\sigma(k)$ annihilate and create a spin σ with momentum k, respectively and obey bosonic commutation relations. In contrast the creation and annihilation of particles $(\hat{p}^\dagger_k, \hat{p}_k)$ and holes $(\hat{h}^\dagger_k, \hat{h}_k)$ obey fermionic statistics and has a massive dispersion relation which also includes the interaction gap Δ_c:

$$\epsilon_c(k) = \sqrt{(\hbar v_c k)^2 + \Delta_c^2} \ . \tag{2.31}$$

Therefore the Hamiltonian describing the charge part can be written as:

$$\hat{\mathcal{H}}_c = \sum_k \epsilon_c(k) \left[\hat{p}^\dagger_k \hat{p}_k + \hat{h}^\dagger_k \hat{h}_k \right] \ . \tag{2.32}$$

The corresponding velocities of spin v_{s} and charge excitations v_{c} can be evaluated by Bethe ansatz and are given in reference [120]. The free energy in the system can be calculated directly, since the Hamiltonians are quadratic [120]:

$$F_{\mathrm{s}} \sim \frac{k_{\mathrm{B}} T^2}{v_{\mathrm{s}}} \tag{2.33}$$

$$F_{\mathrm{C}} \sim \frac{k_{\mathrm{B}} T}{v_{\mathrm{s}}} \frac{1}{\Delta_{\mathrm{c}}} ln \left(1 + e^{-\Delta_c / k_{\mathrm{B}} T}\right) \tag{2.34}$$

The latter expression shows that for the limit of strong interactions ($U > T$), the free energy in the charge sector vanishes. In contrast the free energy of the spin sector becomes larger and larger when interactions are increased. This is caused by the behavior of the velocity of a spin excitation. It diverges for small U/t and tends slowly towards zero when U is increased. In figure 2.5 the QMC results showing the dependence of the number of doublons on the entropy and interactions of the system. Two clear trends are visible. The number of doublons strongly decreases when the interactions are increased and below entropies of about $k_{\mathrm{B}} \mathrm{ln}(2)$ the doublon fraction saturates. The remaining energy in the system is not sufficient to overcome the charge gap anymore, spin excitations which are gapless store the entropy of the system. The minimal required entropy $k_{\mathrm{B}} \mathrm{ln}(2)$ to excite a charge excitation seems however roughly constant across

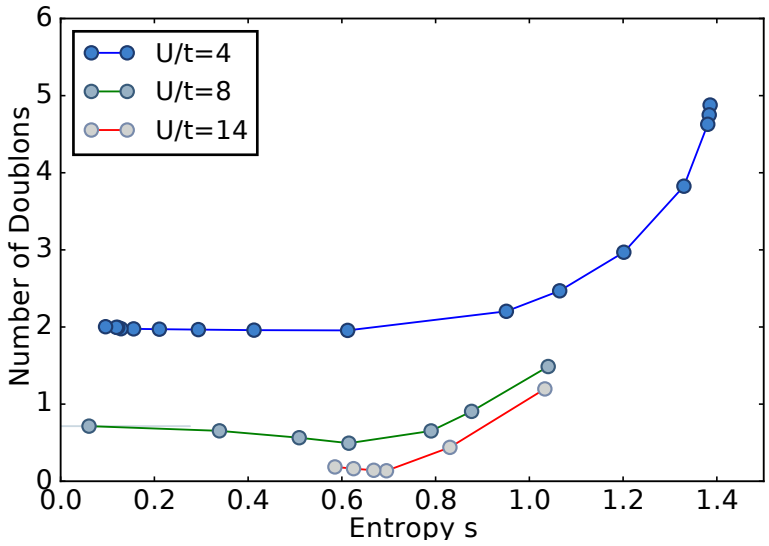

Figure 2.5: **QMC results- Doublon fraction for different entropies and interactions** For a one-dimensional Hubbard chain loaded with a fixed number of atoms $N = 22$ the number of doublons at various entropies and interactions was calculated. For all three values of interactions the doublon number seems to saturate in the low entropy limit. A closer look shows the number of expected doublons to support minima at intermediate entropies ($0.6 < s < 0.8$ for $U/t = 8, 14$) which support the Pomeranschuk effect [121, 122].

the different interactions regimes. This is directly linked to the behavior of the free energy of the spin sector when changing the interactions. The interplay of the sectors free energies cause a minimum of charge excitations at the point maximal relative free energy of the spin sector, which is also contained in the QMC predictions at about $k_{\mathrm{B}}\ln(2)$. The QMC predictions of the spin sector itself, precisely the behavior of nearest-(NN) and next-nearest-neighbor (NNN) correlations in the center of a trapped system, is presented in figure 2.6. For sufficiently strong interactions ($U/t > 6$) the spin correlations strongly increase when the entropy of the system is lowered. The entropy of the system can not be distributed among charge fluctuations anymore. The read out of spin correlations offer a sensitive method to dedicate an entropy of the (sub-)system when the charge-degree of freedom is frozen and is used in chapter 6 to estimate the local entropy and temperature of our Hubbard chains.

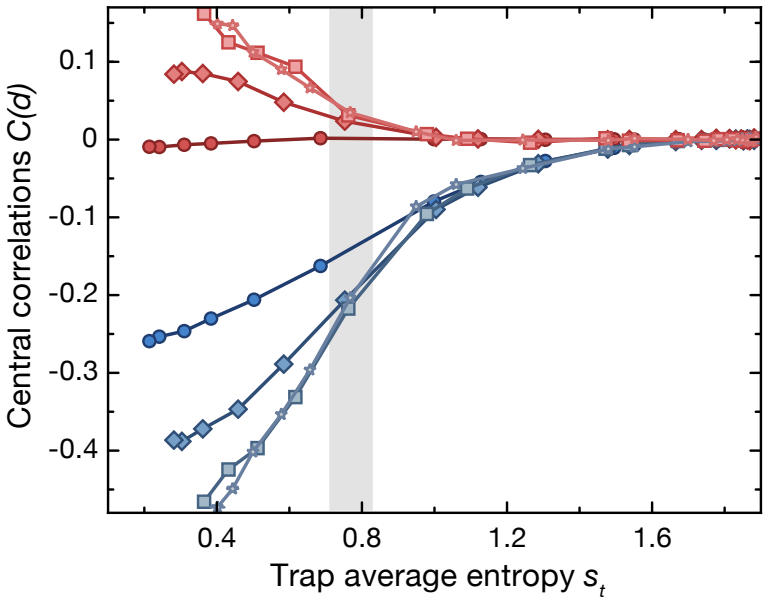

Figure 2.6: **QMC results- Spin correlations NN and NNN for different entropies and interactions** QMC calculations of spin correlations in the trap center. The trap average entropies correspond to the estimated trap average entropy in the experiment for constant particle number of $N \approx 22$. The blue lines correspond to nearest-neighbor (NN) correlations, whereas the red lines represent next-nearest-neighbor (NNN) correlations. The interaction parameter is decoded in the shape of the markers: $U/t = 4$ (circle), 6 (diamond),8 (square), 10 (star). The grey shaded area marks the expected entropy regions of our experiment.

Chapter 3

Experimental setup

The reader who is interested in the setup can refer to the thesis of my colleague Ahmed Omran [83], who described the whole setup to produce low entropy single component Fermi gases, which are investigated in an optical lattice by a quantum gas microscope. With respect to this thesis, the processes of the single plane preparation and the application of optical superlattices to prepare (chapter 4) and investigate two component interacting fermions with a spin resolving quantum gas microscope (chapter 5) have been added. In this chapter, the parts of the experimental setup which are relevant to understand these processes are presented. In figure 3.1, a schematic view on the science cell is shown. It demonstrates the relative position of the high resolution objectives as well as the aspheric lenses to project the optical superlattice and trapping potentials onto the atoms.

3.1 Magnetic field dependence of ^{6}Li

The non-monotonic magnetic field dependence of different hyperfine levels is widely used in atomic physics. The essential magnetic field characteristics of the ^{6}Li electronic ground state $|F = 1/2, m_F = \pm 1/2\rangle$ is shown in a Breit Rabi diagram in figure 3.2. Most of the experiments presented in this thesis were done in an incoherent balanced mixture of the two energetically lowest states labeled $|1\rangle$ and $|2\rangle$. Being energetically degenerate at zero magnetic field, the splitting of the two states increases up to $27\,$G where the Zeeman energy of state $|2\rangle$ has a local maximum. For magnetic fields larger than $70\,$G, in the so called Paschen-Back regime, the two lowest states show the same high field seeking magnetic field behavior with a nearly constant splitting of $70\,$MHz. In this thesis, atoms in the states $|1\rangle$ and $|2\rangle$ in the Paschen-Back regime were evaporated from an optical trap by applying a magnetic field gradient in presence of a homogeneous offset field. The trapping frequency is strongly reduced along the direction of the magnetic field gradient and the hottest atoms escape from the trap.

To guarantee thermalization of the remaining atoms during an evaporation process, scattering processes are needed. Fortunately, ^{6}Li provides a wide range of possibilities to change the sign as well as the magnitude of the scattering length via magnetic Feshbach resonances [22].

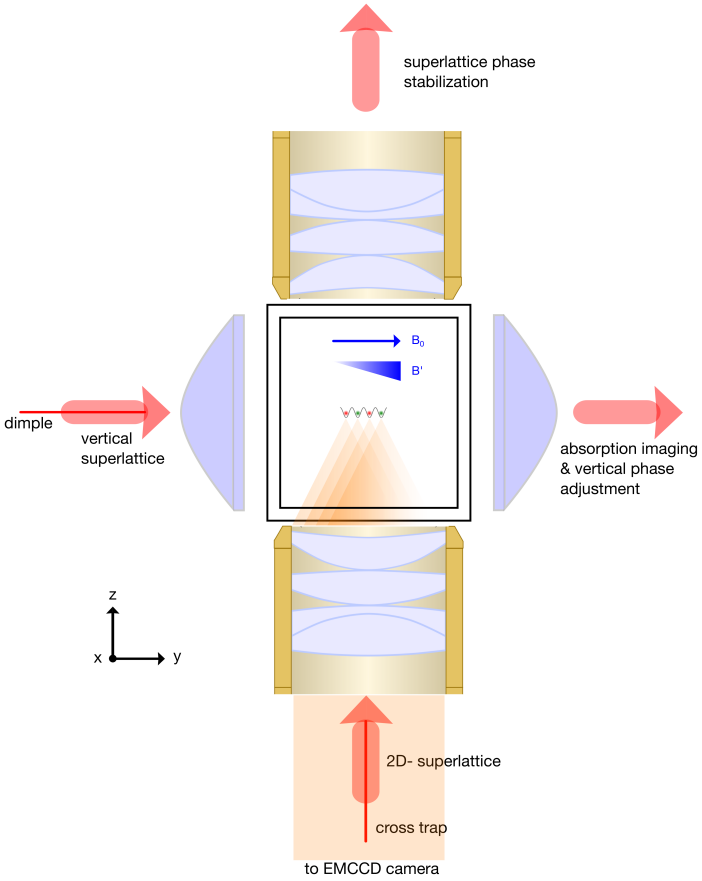

Figure 3.1: **Schematic view onto the glass cell along the x-direction**. The optical superlattices and the cross trap beam are projected through the high resolution objective (custom made NA $= 0.5$, $f = 28.1$ mm triplet lens system) from below. Another objective of the same model recaptures the beams and the optical superlattices are imaged on a CCD to set the relative phase. The vertical lattices and the dimple trap are projected onto the atoms through an aspheric lens (custom made NA $= 0.45$, $f = 40$ mm) along the y-direction. The vertical lattices get recollimated by a lens of the same type and are imaged on a CCD camera to stabilize the relative phase of the vertical superlattice components. The relevant magnetic fields, the Feshbach field and the gradient field are also oriented along the y-direction.

All combinations of the three energetically lowest states $|1\rangle$, $|2\rangle$ and $|3\rangle$ provide a broad Feshbach resonance [123], which are shown in figure 3.3. Additionally, some narrow resonances exist, of which only the one including the states $|1\rangle$ and $|2\rangle$ at 543.1 G [124] was relevant for this thesis. The broad resonance between the states $|1\rangle$ and $|2\rangle$, located at 843 G, was used to tune the scattering length during the evaporation processes to guarantee thermalization as well as during the physics lattice phase to set the onsite interaction energy U.

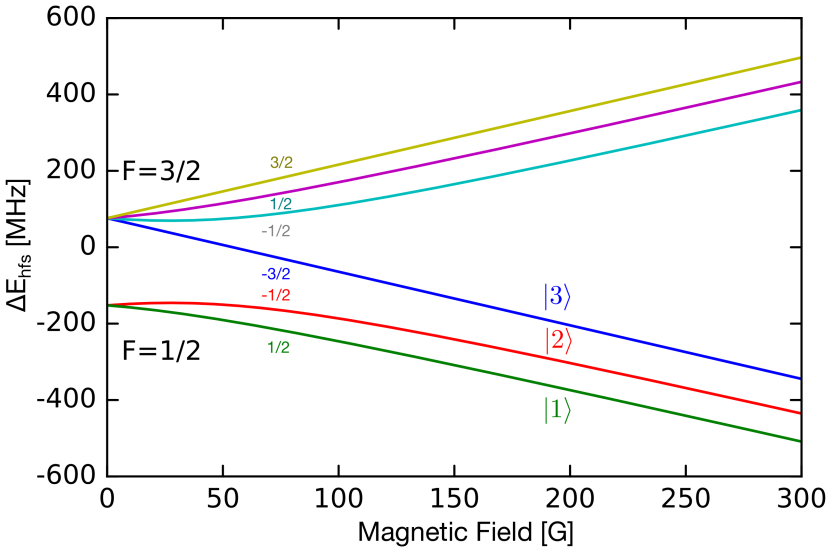

Figure 3.2: **Breit Rabi diagram of the** ^{6}Li $2S_{1/2}$. At zero magnetic field the two fine-structure levels are split by 228 MHz. Up to magnetic fields of 27 G the two hyperfine states $|F = 1/2, m_F = \pm 1/2\rangle$ have opposite magnetic moments. Within each fine structure the hyperfine levels develop parallel within the Paschen-Back regime ($B > 100$ G).

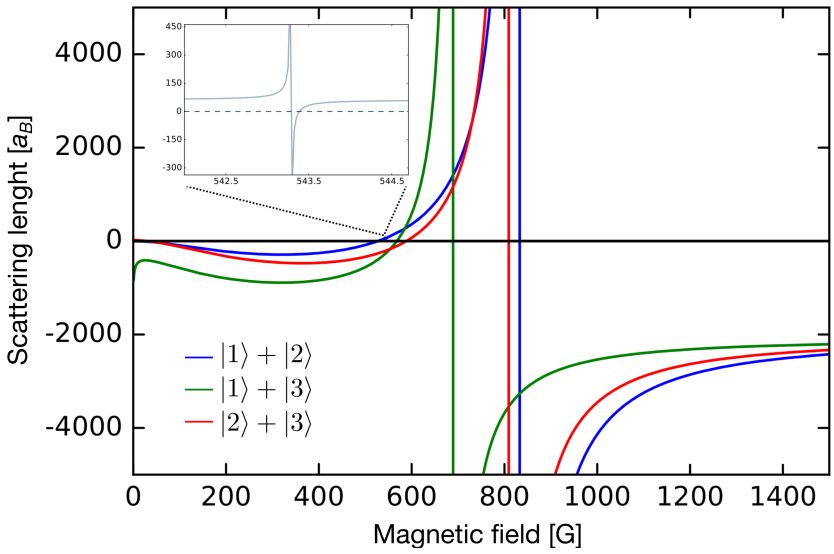

Figure 3.3: **Feshbach resonances of the three energetically lowest states** The data for the resonances were taken from the supplementary material of [123]. The narrow resonance between the states $|1\rangle$ and $|2\rangle$ which is presented in the inset, is located at 543.1 G and has a width of 100 mG only. This resonance needs to be crossed as fast as possible, otherwise it leads to three-body losses. We used this loss to calibrate the magnetic field (see section 4.2.2).

3.2 Optical superlattices

In contrast to the common approach to generate an optical lattice by retro-reflecting a focused laserbeam with wavelength λ, we use two beams which interfere under an angle ϑ creating a one-dimensional standing wave potential with lattice constant:

$$a_{\text{latt}} = \frac{\lambda}{2\sin\left(\frac{\vartheta}{2}\right)} \tag{3.1}$$

Besides recovering the counter-propagating case of $a_{\text{latt}} = \lambda/2$ for $\vartheta = 180°$, one can extract from equation 3.1 the possibility to tune the lattice spacing by choosing the intersection angle ϑ. Using two additional beams of the same wavelength λ which intersect under approximately half the angle $\vartheta/2$ enables the possibility to operate an additional optical lattice with half the lattice period. Overlapping these two lattice potentials in combination with the control of the lattices relative phase φ_{rel} is called an optical superlattice.

3.2.1 Optical superlattices potentials

The potential of an optical superlattice in one dimension is given by:

$$V = V_{\text{l}}\cos^2\left(k_{\text{l}}y\right) + V_{\text{sl}}\cos^2\left(\frac{k_{\text{l}}}{2}y + \varphi_{\text{rel}}\right) \tag{3.2}$$

where V_l and V_{sl} represent the potential depths of the short and long scale lattice respectively and $k_l = \pi/a_{\text{latt}}$ the wavevector of the short scale lattice. The potential heights of the superlattice components can be tuned individually via the power of the beams involved. Together with control over the relative phase of the lattice components, this gives access to a wide range of potentials. Figure 3.4 illustrates the behavior of the superlattice potential for different relative phases φ_{rel} including the full asymmetric $\varphi_{\text{rel}} = \pi$ as well as the full symmetric case $\varphi_{\text{rel}} = \pi/2$.

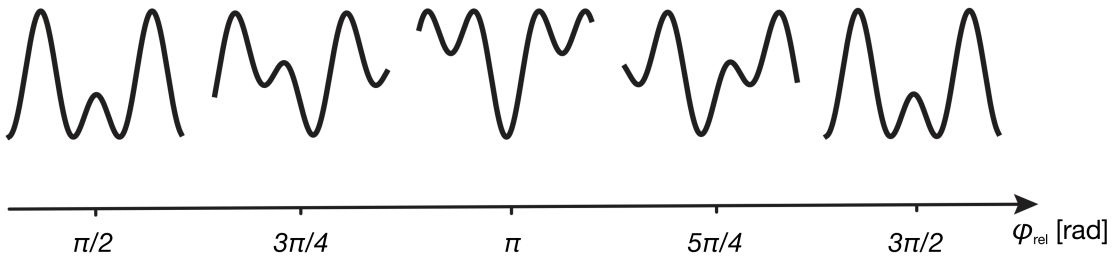

Figure 3.4: **Schematic view of a one-dimensional superlattice potential for different relative phases φ_{rel}.** Local double wells are symmetric for $\varphi_{\text{rel}} = \pi/2$ totally antisymmetric for $\varphi_{\text{rel}} = \pi$. The two depicted symmetric points are degenerate in their density.

3.2.2 Experimental realization of a two-dimensional superlattice

To realize interfering beam pairs under an angle ϑ and $\vartheta/2$ we directly use the high resolution objective ($f_{\text{eff}} = 28.1\,\text{mm}$, NA $= 0.5$), which is also used for the single-site resolved fluorescence imaging. A perfectly parallel pair of beams, each with a distance of δ to the optical axis of the objective, is sent to the microscope and gets projected under the relative opening angle:

$$\vartheta = 2 \cdot \arctan\left(\frac{\delta}{f}\right) . \tag{3.3}$$

According to equation 3.1 with a distance of $\delta = 13\,\text{mm}$ to the optical axis, the one-dimensional lattice has a lattice constant of $a_{\text{latt}} = 1.15\,\mu\text{m}$. Extending the potential to an optical superlattice was done by adding a second pair of beams [1] with half the distance to the optical axis, resulting in twice the lattice constant compared to the short scale component. The principle of the setup is illustrated in figure 3.5. Due to the radial symmetry of the microscope

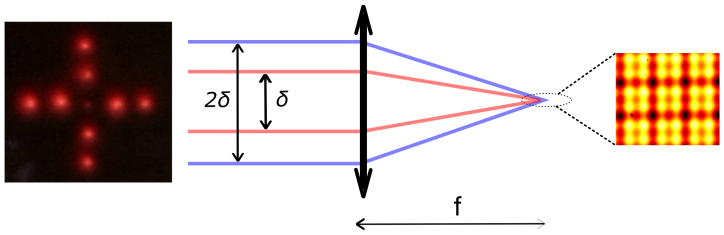

Figure 3.5: **Projected superlattice.** Schematic view of the projection technique of a two- dimensional superlattice. A beam pair (blue) of distance $2\delta = 26\,\text{mm}$ is refracted by the high resolution objective with focal length $f = 28.1\,\text{mm}$. The resulting potential is a one-dimensional lattice with a spacing of $a_{\text{latt}} = 1.15\mu\text{m}$. Adding a second beam pair with half the distance (red) results in a one-dimensional superlattice. The photography (left) of the full input pattern shows the extension of the setup to a two-dimensional superlattice potential (right), by adding two more beam pairs in a perpendicular plane.

lens, the extension to a two-dimensional square superlattice is achieved by adding two other pairs of beams with the same distances to the optical axis but rotated by $90°$ around it. This simple extension of the lattice potential also shows the strength and flexibility of the projection method, for example three interfering beams with intersection angles of $120°$ would result in a triangular lattice potential.

The biggest challenge is the production of the input pattern which consists of eight parallel beams. The beams of each pair need to be phase coherent, and the Gaussian beam sizes should be the same. Using a modified type of Michelson interferometer we produce the four beam pairs

[1] Using an AOM the long scale lattice beams are shifted by 110 MHz relative to the short scale component to avoid interference cross talk

which are sent to the microscope objective. The working principle is shown and explained in figure 3.6. Single beams which propagate parallel to the optical axis, which by itself is defined by a collimated beam, are each split into two parts at a polarizing beam splitter (PBS). Both arms get retro-reflected whereas one arm consists a aspheric lens which inverts the relative orientation of the lattice beams with respect to the optical axis. This way, we produced four parallel beam pairs out of four ingoing single beams. The whole interferometer is defined by its optical axis, which we not only used to align the setup by also to stabilize the relative arm lengths with the piezo electric element driving the common mirror in the lens arm of the interferometer, depicted as ③ in figure 3.6. The stabilization scheme will be reviewed in more detail in section 3.2.4.

3.2.3 Vertical lattice

The same interferometric technique is used to produce a vertical superlattice potential with lattice constants of $a_{z,\text{short}} = 1.56\,\mu$m and $a_{z,\text{long}} = 3.12\,\mu$m. The beams leaving the interferometer are projected onto the atoms by a custom made aspheric lens of focal length $f = 40\,$mm as illustrated in figure 3.1. For the experiments presented in this thesis, only the simple lattice potential with plane distances of $a_{z,\text{long}}$ have been used. The atoms are transferred from the dimple sheet of vertical waist $w_z = 1.7\,\mu$m into a single plane of the vertical lattice where they are kept during the whole evaporation and lattice and imaging phase. Two main effects can reduce the signal to noise ratio during the fluorescence imaging which are linked with the vertical lattice. Non perfect overlap of the dimple trap and the chosen lattice plane will lead to some atoms getting trapped in neighboring planes. Since they are not in focus during the imaging process, they cause parasitic background signal reducing the signal to noise ratio. Secondly, a drift of the lattice planes during the imaging process as well as from shot to shot leads to an enlarged obtained point-spread function of an atom, again reducing the signal to noise ratio of the imaging process [125].

3.2.4 Phase stabilization and control

The stabilization of the lattice phases plays an important role for the experiments. In the following, our realization and its peculiarities regarding the realization of a spin resolving quantum gas microscope, will be given. More detailed informations about the setup and the characterization can be found in the diploma thesis of my colleague Michael Lohse [126]. The interferometric approach (figure 3.6) generates each beam pair out of the different single beams. Since the components of the beam pairs propagate along different arms of the interferometer, the phase they pick up is not the same. Non-common optical elements or airflow will cause an unstable relative phase of the lattice components and therefore result in moving lattice potentials. In case of the simple x-y-lattice this might be still tolerable if the frequency of the relative phase drifts and fluctuations is lower than the trapping frequencies and therefore does not induce heating in the system. But already in the case of the simple vertical lattice potential an unstable phase reduces the long term stability of the single plane preparation process (subsection 4.1.1) dramatically.

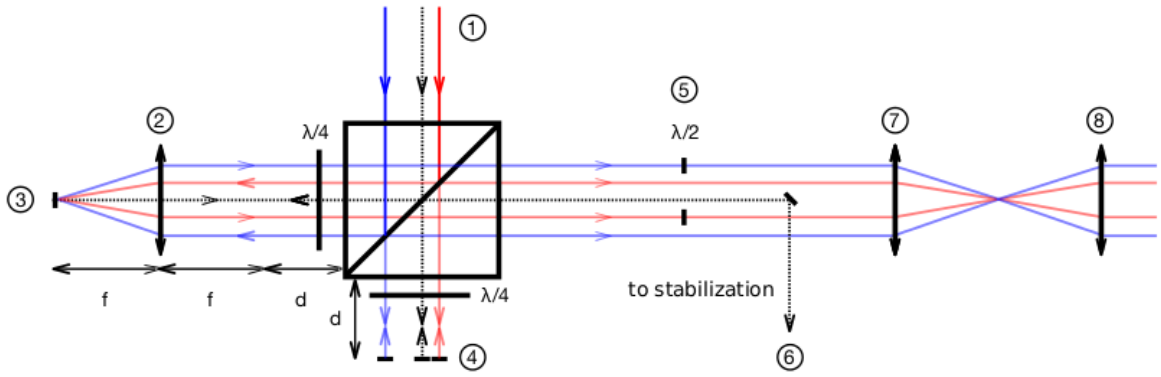

Figure 3.6: **Interferometer setup to produce the superlattice beams.** ① The optical axis (black, dashed line) is defined by a collimated beam and sets also the optical axes of all transmissive elements in the lattice setup. Two beams of distance δ (blue,short component) and $\frac{\delta}{2}$ (red,long component) to the optical axis are sent to a polarizing beamsplitter cube (PBS) where they each get split into two parts of equal intensity. The reflected beams get focused by an aspheric lens ② and converge on a retro-reflecting mirror ③ which can be driven by a piezoelectric element to control the arm length of the interferometer. Since the mirror is placed in the focal point of the lens, the retro-reflected beams switch their relative orientation but remain parallel and have the same distances to the optical axis again after being transmitted through the lens. The position of the lens was chosen such that the length of the optical path is the same as for the transmitted components which get retro-reflected at the array of independent mirrors ④. The mirrors of the array which retro-reflect the long lattice components (red) are also piezo driven which opens the possibility to control the relative phase φ_{rel} of the superlattice potential. In both arms of the interferometer, the beams have to pass through $\lambda/4$- waveplates twice turning the polarizations such that the beams leave at the same port of the PBS. An array of small $\lambda/2$ waveplates ⑤ matches the polarizations of the components of each beam pair to ensure their interference after the high resolution objective ⑦. The optical axis beam is removed from the interferometer before the objective ⑥ to the stabilization setup. The superlattice beams interfere at the position of the atoms and get collimated by an equivalent microscope ⑧ where they are imaged onto a CCD to measure the relative phase of the superlattice components.

In case of an optical superlattice a drifting and fluctuating relative phase of the components not only induces a global movement of the potential but also changes the shape of the superlattice potential. The basic stabilization scheme is shown in figure 3.7. The main principle of the scheme is to read out the relative phase of the two components of the alignment beam by interfering them on a photodiode. Since the interference signal does not contain information of the sign of the relative phase $\Delta\varphi$ a lock in-detection scheme was used. After propagating through the two interferometer arms, the two components were overlapped again but have orthogonal

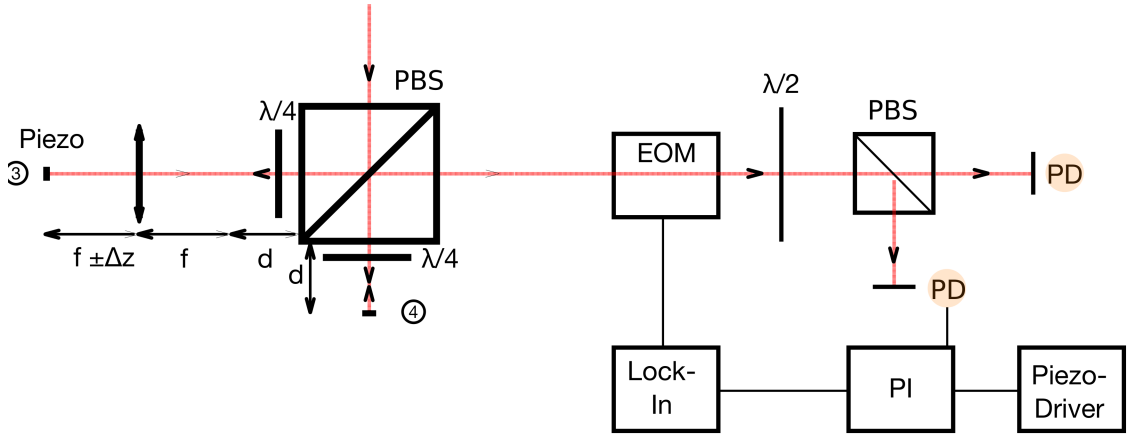

Figure 3.7: **Schematic of the arm length stabilization setup.** The alignment beam entering the interferometer was split at the cube. After passing through the two arms the beams were overlapped again and pass through and EOM which modulates only the polarization component parallel to its electrical field. The polarization is rotated and the two beams interfere on a fast photodiode (PD). By using a lock-in technique and a PI controller a feedback signal driving the piezo was generated.

polarizations. They are passing through an electro-optical modulator which only modulated one of the polarizations. A $\lambda/2$-waveplate rotated the polarizations and the two components were overlapped on a fast photodiode. The lock-in photodiode signal was demodulated at the EOM driving frequency to produce a error signal which is sensitive to the sign of the relative phase. A feedback signal which was generated from the error signal in a home built PI controller was sent to a piezo driver that changes the optical path length. The full error signal has an amplitude of $1.8\,\mathrm{V}$ and a standard-deviation during closed loop operation of $6.5\,\mathrm{mV}$. This corresponds to a phase error of $3\,\mathrm{mrad}$. Of course this stabilization scheme corrected only for global effects on the phase, since the lattice beams did not propagate on the exact same path as the alignment beams and even have non-common optical elements and mounts. In addition the alignment beams which are sent to the stabilization were picked up directly behind the interferometer, so it could not correct for effects on the optical path ($\approx 1\,\mathrm{m}$) from the interferometer to the atoms in the glass cell. Therefore an additional active stabilization scheme using the superlattice potential directly was used. The beams interfering at the position of the atoms in the glass cell were collected by an objective above the glass cell (see figure 3.1) and imaged with an additional lens on a CCD camera [2]. The recorded intensity pattern was fitted with a linear superposition of two lattices with wavevectors k_i, phases φ_i, amplitudes I_i and background signal B:

$$I(x) = I_1 \cos^2(k_1 x - \pi\varphi_1) + I_2 \cos^2(k_2 x - \pi\varphi_2) + B \quad . \tag{3.4}$$

Movements of the global φ_{cms} and the relative phase φ_{rel} which were defined as:

[2] Guppy PRO F-031 by Allied Vision

$$\varphi_{\text{cms}} = (\varphi_1 + 2\varphi_2)/2 \tag{3.5}$$

$$\varphi_{\text{rel}} = \varphi_1 - 2\varphi_2 \tag{3.6}$$

could be directly measured. Since the beams of the short lattice components were retro-reflected at mirrors which are mounted on sensitive piezo shifters [3] (see ④ in figure 3.6) the relative superlattice phases φ_{rel} can be tuned. This opened not only the possibility to change the shape of the superlattice potential (see figure 3.4) but also to monitor the long term stability of the relative lattice phases and correct for errors at each shot before atoms were loaded into the optical superlattice. The fitted images were also employed to correct for small errors of the parallelism of lattice beams in the interferometer, resulting in non-commensurate wavevectors k_i. This effect shows up as a spatial gradient of the relative phase, changing the shape of the superlattice potential along the cloud. The ratio of the wavevectors was matched such that the lattice constant of the large component was twice the constant of the short component. Technically this was achieved by fine adjustment of the parallelism of the short and long lattice component beams entering the interferometer. The spin splitting process which is described in chapter 5 required a symmetric superlattice configuration along 15 long component lattice sites. Since the maximum Zeeman shift to tilt the double wells for the different spin states is $\Delta E_{\text{LR}} = \pm h \times 6.2(6)\,\text{kHz}$, energy shifts due to phase fluctuations and spatial phase gradients need to be smaller than ΔE_{LR}. A calculation in chapter 5 translates this energy into a phase, which needed to be more stable than $\pm 100\,\text{mrad}$. We observed the relative phase in different experimental environments by using the imaging onto the CCD camera. First of all we probed the phase stability outside the real experimental sequence, allowing for a high repetition rate and a easy access to the interferometer and the lattice beams. Unfortunately first measurements showed fluctuations larger than $200\,\text{mrad}$. Most important was a quick check that the sensitivity of the phase measurement was not limited by the optical path from the position of the atoms to the CCD camera onto which the atoms were imaged. A quick measurement of the relative phase fluctuations immediately behind the interferometer gave the same results, which pointed strongly towards the interferometer itself where parasitic phases were picked up. We successively reduced the phase fluctuations by mechanical decoupling the interferometer setup from its environment. A shielding out of massive cardboard blocked airflow from the flowboxes, which are part of the air conditioning system. Whereas uniform airflow by itself would have not caused trouble, its combination with complex mechanical setups produced turbulences which locally change the refraction index and therefore induced different optical path lengths for the different lattice beams [127]. Additionally we isolated the system with sound absorbing material to avoid excitation of the piezo electrical actuators due to ambient noise from the laboratory. These installations decreased phase fluctuations by a factor of two. Finally the phase noise was reduced to $50\,\text{mrad}$ (see figure 3.8) by lowering the strength of the flowbox. A test to completely turn the airflow off failed, since the temperature of the table became unstable during the real measurement sequence, which operates all sources of heat as magnetic fields and high power lasers. The temperature instability had a direct negative effect on the single plane loading

[3] S-303, Physik Instrumente, closed loop resolution 0.03 nm.

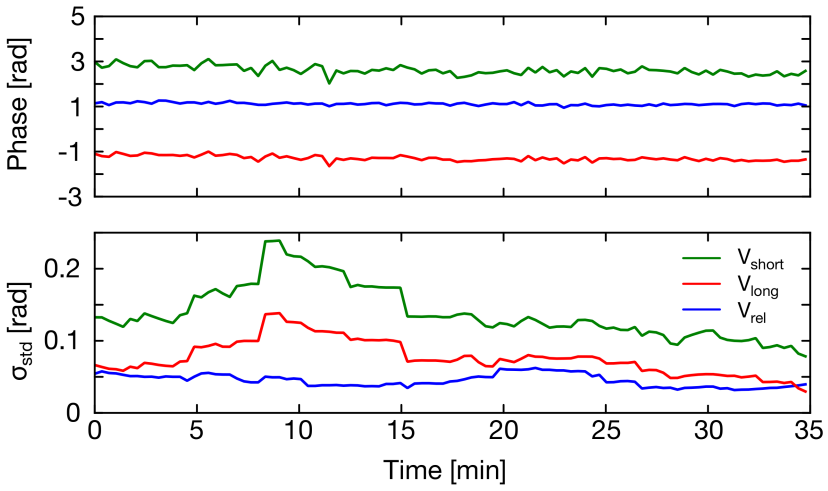

Figure 3.8: **Passive relative phase stability of the optical superlattice potential.** By Fourier transformation of the imaged superlattice potential on a CCD camera, we extract the absolute lattice phases. **Upper plot:** The absolute phase of the short scale component was set to 3 rad. We read out the temporal evolution of the absolute as well as the relative lattice phases, with a probing cycle of 20 s. **Lower plot:** Deviations from the set phases. Most of the deviations occurred commonly on the large and short scale component. As expected common errors show up twice as large in the phase of the short scale component compared to the long scale component and cancel in the derivation of the error of the relative phase. The mean value of the relative phase error was in this case $53(4)$ mrad.

and the focusing of the high resolution microscope, rendering the operation of the experimental setup impossible.

Chapter 4

Preparation of fermionic Hubbard chains

A fast and robust preparation of ultracold atomic samples is the basis of every experimental setup dealing with ultracold atoms in optical lattices. Our setup employs many different steps to cool and shape the density of the atomic cloud, to load low entropy samples in the optical lattice with high fidelity. The processes, which are relevant extensions to the status presented by my colleague Ahmed Omran [83], are presented in this chapter.

Given a degenerate cloud of $2 \cdot 10^4$ atoms at $T/T_F \approx 0.20(7)$, which we estimated by fitting absorption images of the cloud with a Fermi-Dirac distribution [117],trapped in the dimple sheet, the experimental production of ultracold fermionic Hubbard chains, which are feasible for the investigation with a quantum gas microscope, can be divided into two parts. The first step is to transfer the atoms into a single plane of the vertical lattice potential. The aspect of single plane loading is most important for the microscopic investigation of the lattice gas, to avoid parasitic fluorescence from atoms trapped in planes out of focus. This two-dimensional gas is further cooled with magnetically supported evaporation. The second step is the ramp up of the lattice potential. The atoms were first isolated in 1 dimensional tubes before the lattice potential along these tubes was ramped up. The resulting Hubbard chains were studied with the spin resolving quantum gas microscope. Details of the preparation processes are given in this chapter.

4.1 Production of two-dimensional degenerate spin mixtures

The description of the preparation process begins with atoms trapped in the dimple light sheet. The experimental steps to prepare the cloud in the dimple were already described in detail in the thesis of my colleague Ahmed Omran [83]. These processes are briefly summarized in a chronological order given by their appearance during the experimental cycle:

- Evaporation of solid $^6\mathrm{Li}$ in an oven with small output aperture, Zeeman slowing of the resulting atomic beam.

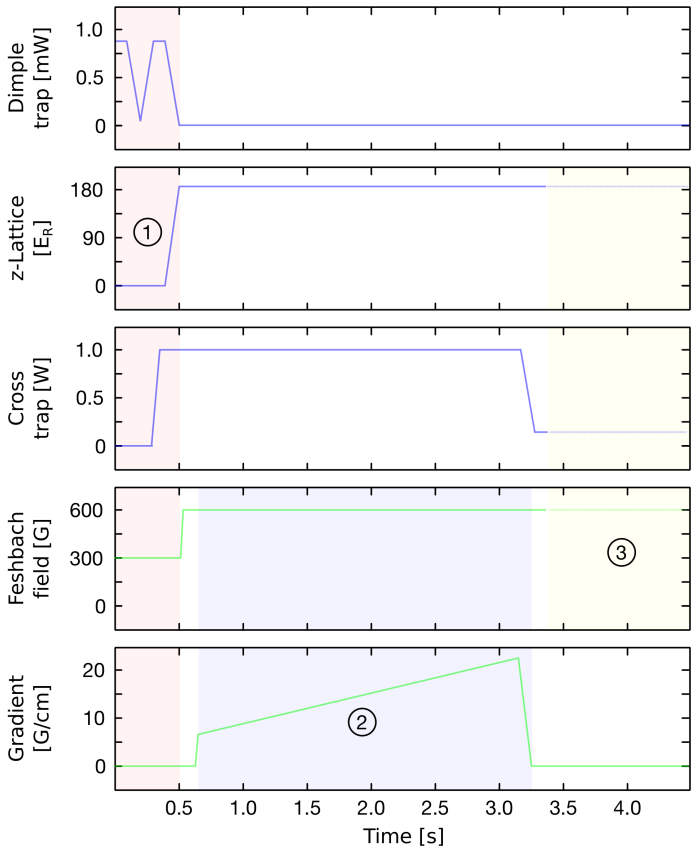

Figure 4.1: **Timetable of relevant parameters involved in the preparation process of the two-dimensional degenerate gas** ①: After the spill-out process in the dimple trap, the atoms are transferred into a single plane of the z-lattice. ②: Before the evaporation process starts, the scattering length is changed. Afterwards the trapping frequency is lowered along the direction of the magnetic field gradient by increasing its magnitude in 2.5 s. ③: At the end of the evaporation the magnetic field gradient is ramped to zero and the transverse confinement is lowered by decreasing the cross trap intensity. This reduces the density to prevent three body losses.

- Laser cooling and trapping in the MOT chamber, first on the broad (red) cooling transition $\left|2S_{1/2}\right\rangle \rightarrow \left|2P_{3/2}\right\rangle$ and secondly employing the narrow transition in the ultraviolet $\left|2S_{1/2}\right\rangle \rightarrow \left|3P_{3/2}\right\rangle$ at 323 nm.
- Loading into the large volume magic-wavelength dipole trap ($P = 60$ W (of a 100 W output power multi-mode fiber amplifier), $\lambda = 1070(3)$ nm, $w_0 = 100\,\mu$m), pre-evaporation and transfer into the small volume tightly confining transport trap ($P = 3.5$ W, $\lambda = 1064$ nm, $w_0 = 28\,\mu$m).
- Optical transport into the science cell, thermalization of the atomic cloud in the crossed

dipole trap by ramping up the cross beam ($P = 3.0$ W, $\lambda = 1064\,\text{nm}$, $w_0 = 78\,\mu\text{m}$) at moderate attractive interactions ($a_s = -290\,a_B$).

- Ramping up the dimple potential during the optical evaporation. Adiabatic ramp down of the crossed dipole trap and transfer into the dimple potential.

The upcoming processes which transform the cloud into a degenerate sample trapped in a single plane are shown in figure 4.1. The illustration shows all traps and magnetic fields which are involved in the single plane loading process ①, the magnetic evaporation ② as well as the density matching before the lattice phase ③. The different phases are explained in more detail in the next sections.

4.1.1 Single plane preparation

An incoherent balanced mixture of about $2 \cdot 10^4$ atoms in the states $|1\rangle$ and $|2\rangle$ was trapped in the elliptical shaped dimple light sheet. The Feshbach field was adapted such that interactions were moderately attractive ($a_s = -290\,a_B$). To guarantee single plane loading of the vertical lattice potential, the dimple trap was spilled out in presence of this field. The spill out process reduced the number of atoms and the cloud size which minimized the overlap of the atomic cloud with neighboring planes. To illustrate this the measured Gaussian cloud sizes of the full cloud ($\sigma_{\text{full}} = 2.4\,\mu\text{m}$) and the spilled-out cloud ($\sigma_{\text{s-o}} = 1.3\,\mu\text{m}$) are compared with the plane to plane distance of the vertical lattice $d_z = 3.1\,\mu\text{m}$. Therefore the spill-out process reduces the ratio of atoms transferred into neighboring planes compared to the central plane population from 20% below 1%. Additionally, the total number of atoms was reduced by only about a factor of two during this process, guaranteeing good starting conditions for the upcoming evaporation process. After the spill-out process the z-lattice potential was linearly ramped up in $100\,\text{ms}$ to $178\,E_R$. When the vertical confinement had reached its maximum value the dimple trap was adiabatically turned off. Transverse confinement was controlled with the power of the cross beam. Therefore we loaded about $N = 8000$ atoms at temperatures of $T = 1\,\mu\text{K}$ into a single plane of the vertical lattice. Note that the scattering properties of the system can still be regarded as three dimensional, since the sufficient conditions to describe the system as quasi two-dimensional [128–130] are not given. The vertical harmonic confinement length l_z of the system is still comparable with the thermal wavelength λ_{dB} and the measured transversal average interparticle distance $n^{-1/2}$.

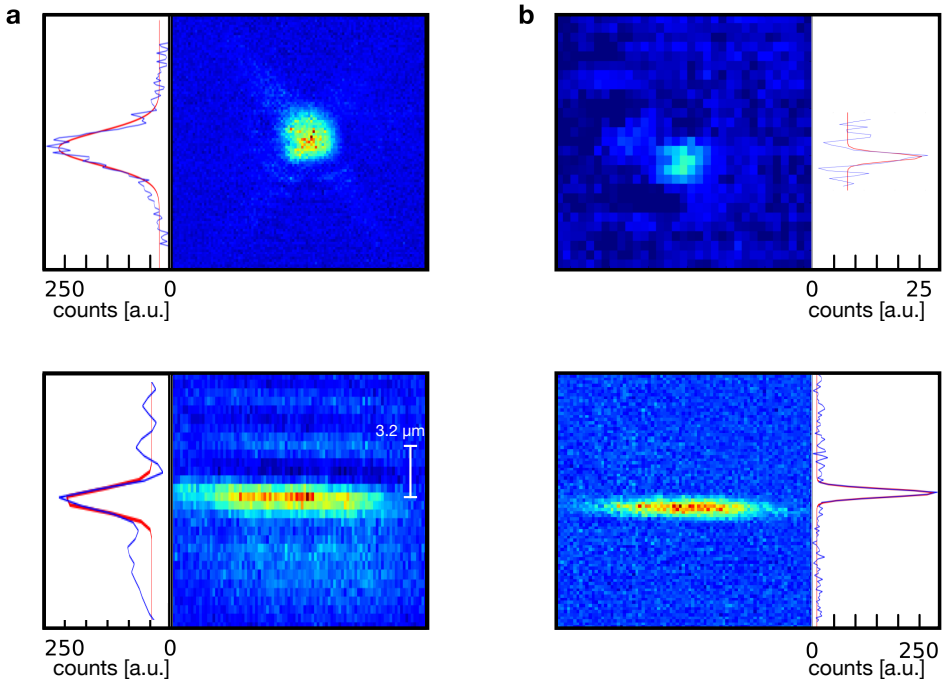

Figure 4.2: **Effect of dimple spill out on plane loading process.** Absorption images of different cloud realizations. **(a)** Fully loaded dimple trap (top left, $P = 1\,\mathrm{mW}$) containing about 10^4 atoms. After adiabatic release into the long scale z-Lattice (bottom, $V_z = 178\,E_R$) atoms populate not only the central but also the neighboring planes. **(b)** Spilling out the dimple trap (top right) by reducing its power to $P = 0.1\,\mathrm{mW}$, reduces the number of atoms and the size of the cloud, such that only a single plane of the vertical lattice gets populated (bottom right).

4.1.2 Magnetic evaporation

Since we needed to maintain the single plane character of the system usual evaporation techniques where the optical confinement along all directions is gradually lowered could not be applied. Otherwise the atoms would be able to tunnel along the vertical direction and therefore repopulate neighboring planes. Therefore the evaporation process was magnetically driven along the transverse direction. It made use of the high field seeking character of the two states in the Paschen-Back regime when applying large magnetic fields. The large Feshbach field of $599\,\mathrm{G}$, which corresponds to a scattering length of $a_s = +353\,a_B$, was set before the evaporation process started and brought us well in the Paschen-Back regime. By adding the magnetic field gradient along the direction of the homogeneous field, the effective transverse trapping frequencies are lowered. When the applied magnetic field gradient was large enough, atoms escaped the trap and the remaining atoms thermalized at a lower temperature.

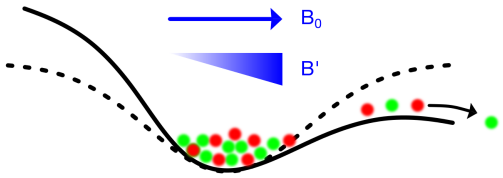

Figure 4.3: **Schematic view on the magnetic evaporation.** The optical trapping potential is tilted along the direction of the applied gradient B', since the atoms were prepared in the states $|1\rangle$ and $|2\rangle$, which are high field seeking at the magnetic field value $B_0 = 599\,\mathrm{G}$.

The magnetic field gradient was ramped quickly to $6\,\mathrm{G/cm}$ at the beginning of the evaporation. This value was experimentally determined by keeping the atoms in the presence of different gradient fields for $100\,\mathrm{ms}$. We picked the value for which the number of atoms start to diminish as the initial evaporation gradient. The evaporation proceeded by slowly ramping the magnetic field gradient towards its maximum strength of $27\,\mathrm{G/cm}$ in $2.5\,\mathrm{s}$. The exact final value sets the final number of atoms as well as the temperature of the system. For all experiments described in chapter 6, the magnetic evaporation stopped at $25\,\mathrm{G/cm}$ leaving about 100 atoms which were loaded into the optical lattice. At the end of the evaporation process, the magnetic field gradient was ramped down to zero before the atoms were allowed to spread transversally by reducing the cross trap confinement. All ramp durations, scattering lengths and field gradients were optimized by minimizing the number of holes and doublons in a two-dimensional Mott-insulator in the short lattice observed under the microscope. Special care was taken to avoid three body losses and heating of the gas. Especially the timing of Feshbach field ramps was important. Due to the location of the narrow Feshbach resonance at $543.286\,\mathrm{G}$ the system had to cross this region when the 3D scattering length was changed from moderately attractive to repulsive. This step was necessary anyway, since the Hubbard-chains were studied at the

repulsive region of the Fermi-Hubbard phase diagram. The three body loss rate $\dot{n}$ scales as [124]:

$$\dot{n} = -L_3 \cdot n^3, \tag{4.1}$$

whereas n is the density of the system and L_3 the three-body loss coefficient. Due to the cubic dependence on density, it was essential to ramp across the resonance only in cases where the atoms were allowed to spread transversally or when they were trapped in isolated lattice wells.

4.1.3 Hubbard chain preparation

Low enough temperatures of the two-dimensional sample below $T/T_F < 0.1$ is only one of the requirements to realize low entropy Hubbard chains. It is of the similar importance to load the gas into the optical lattice sites without heating it, for example by parametric heating. Since this heating process scales with ω^2_{trap} [131] this process is much more severe for atoms in lattices than in simple traps where the trapping frequencies are usually lower. Therefore we carefully adjusted the parameters of the PID controller to avoid oscillatory or overshooting behavior of the intensity stabilizations. After the evaporation ended and the transverse confinement was reduced, we set the scattering length (and thus the final interaction strength U in the lattice) by varying the Feshbach field between $529\,\text{G}$ and $657\,\text{G}$.[132]. Usually the atoms were kept as short as possible at these strong interactions to minimize heating due to three-body recombination.

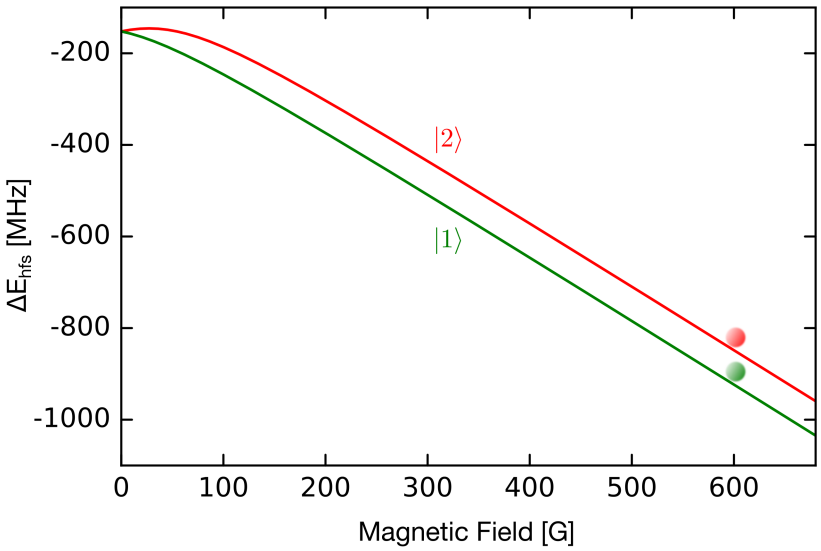

Figure 4.4: **Breit Rabi diagram of the two lowest spin states.** At the magnetic field of $599\,\text{G}$ set by the Feshbach field, both states are high field seeking, which we used for magnetically driven evaporation.

For some measurements, we used this holding time to heat the gas actively and measured the entropy dependence of antiferromagnetic correlations (chapter 6).

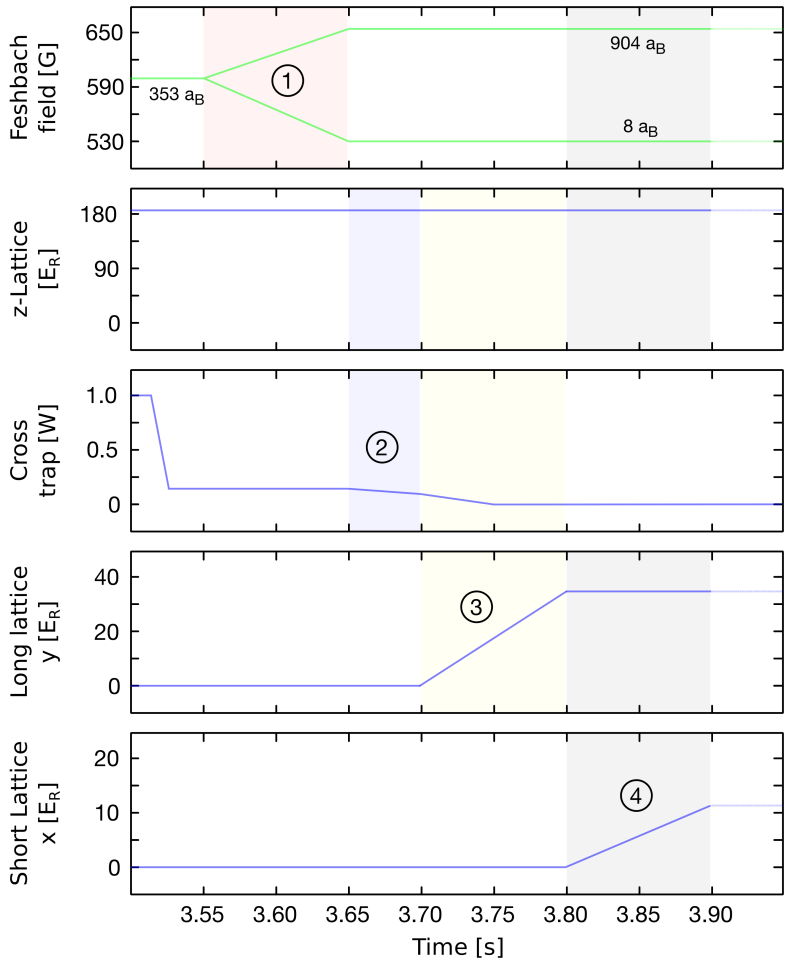

Figure 4.5: **Timetable of the Hubbard chain preparation.** ①: After decreasing the transverse confinement to lower density by lowering the cross trap power, the desired scattering length was adjusted by ramping the Feshbach field in 100 ms. The scattering lengths varied between $a_s = 8a_B$ and $a_s = 904a_B$. ②: The transverse profile of the cloud was shaped by lowering the cross trap power even more. ③: The long scale component of the superlattice along the y-direction was ramped up to $34E_R$in 100 ms and the cross trap was ramped to zero in the first 50 ms of this ramp. ④: The atoms, being trapped in isolated 1-dimensional tubes, were adiabatically loaded into the short scale lattice potential along the x-direction with a depth of $11E_R$.

4.2 Calibration of the Hubbard parameters

To gain precise knowledge about the energy scales of the Hubbard Hamiltonian one needs to calibrate the parameters. The full Hamiltonian is characterized by the tunneling, a measure of the mobility of the atoms in the optical lattice, and the interaction energy, describing the collisions between two atoms. The tunneling can be calculated as the overlap integral of Wannier functions of the lowest band from neighboring lattice sites. To be able to calculate the Wannier functions the optical lattices have to be characterized. The sizes of the lattice beams as well as the lattice depths were measured for different powers. Since we are working in the so called ultracold temperature regime, the scattering process can be parametrized by a single parameter, the so called s-wave scattering length [92]. The interaction can be assumed to be purely onsite, since the lattice spacing is much larger than the maximum expected scattering length ($d_L = 1.15\,\mu\text{m} \gg 1000\,a_B \approx 47$ nm).

4.2.1 Lattice parameter calibration

The beam sizes were determined by using each lattice beam as a single beam which was crossed with the transport trap, containing about 10^5 atoms. The lattice beam was abruptly turned on at a certain power. This initialized a breathing mode oscillating with twice the trap frequency [133]. Since the crossing angles between the lattice beams and the transport trap is either 65° (short lattice) or 77° degree (long lattice) and the axial trapping frequency of the transport trap is very low, one of the radial components of the breathing mode oscillation represents the radial trap frequency of the lattice beam. The oscillation frequency was extracted by fitting the Gaussian cloud width versus time with a damped cosine oscillation for three different lattice beam powers and taking the average. Given the measured powers and the oscillation frequencies one can calculate the beam waists of the lattice beams. Under ideal conditions one would be able to calculate also the depth of the lattice wells because the single beams are fully characterized. But since the visibility of the interference pattern also depends on the polarizations as well as the overlap of the individual lattice beams, it was important to measure the lattice depths with a different method.

To calibrate the depth of the various lattices we performed lattice modulation spectroscopy [134]. By modulating the amplitude of the periodic potential, atoms from the ground band get transferred to the second excited band [1]. To this end, we used a spin polarized sample in the $|1\rangle = |F = 1/2, m_F = -1/2\rangle$ state to avoid effects of the interparticle interaction trapped in the crossed dipole trap. After the lattice was ramped to the desired value, we modulated its intensity for $300\,\text{ms}$ with an amplitude of 3%. We probed the band structure by recording the number of trapped atoms versus the modulation frequency. The number of lost atoms is a measure for the number of transferred atoms from the ground ($\nu = 0$) to the second excited band ($\nu = 2$). Since our system is fermionic the transitions include different transition frequencies belonging

[1] Due to the conservation of parity, the excitations to the first excited band are suppressed.

to different quasimomenta $q = 0 \rightarrow q' = 0$ to $q = \pi \rightarrow q' = \pi$. We picked the lowest ($q = 0$) as well as the highest transition frequencies ($q = \pi$) to calibrate the lattice.

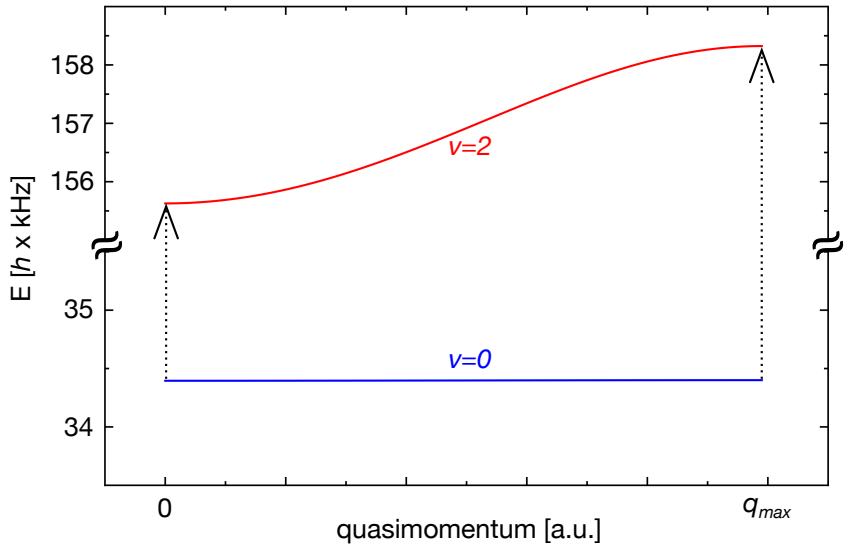

Figure 4.6: **Band structure of the lowest and the second excited band.** The curvature of the second excited band, given by its dispersion relation, broadens the spectrum of the excitation frequencies. We assign the lowest and highest transition frequencies to excitations $q = 0 \rightarrow q' = 0$ and $q = \pi \rightarrow q' = \pi$, respectively. The equivalent band structure and transitions also apply for $q < 0$, since the bands scale as $\sim q^2$.

We used the center of the falling (rising) edge of the loss feature (figure 4.7) as the lowest (highest) frequency. The beam powers as well their Gaussian widths were used as free fit parameters to minimize the differences between the calculated transition frequencies from band structure and the measured values. We performed these calibrations for all beams of the transverse as well as the vertical superlattice.

4.2.2 Interaction strength calibration

The s-wave scattering length a_s can be tuned via the Feshbach resonance by controlling the magnetic field B. The Feshbach resonances of the two lowest hyperfine levels of the electronic ground state of ^{6}Li have been characterized in detail [123, 124]. The results of these studies were used to calibrate the magnetic field as well as the scattering length a_s.

To calibrate the magnetic field we used the narrow Feshbach resonance between the states located at $543.286\,\mathrm{G}$ [124] which has only a width of $100\,\mathrm{mG}$ and a background scattering length of $a_{bg} = 62\,a_B$. We identified the location of the narrow resonance with a spectroscopic

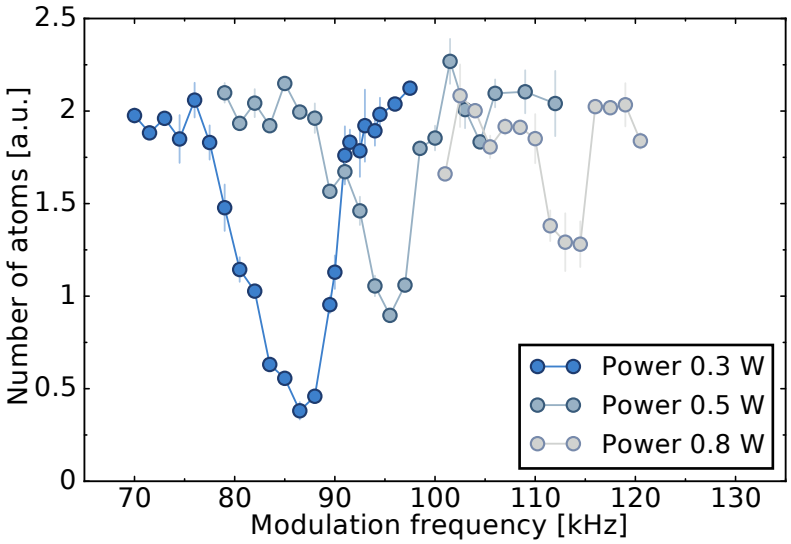

Figure 4.7: **Modulation spectroscopy of the short lattice component along the x-direction.** The loss measurement was performed for three different powers per beam. We measured the number of atoms with absorption imaging after modulating the lattice beam intensity for $300\,\mathrm{ms}$ with an amplitude of 3%.

measurement. We kept 10^5 atoms at $T/T_F \approx 0.25$ in a crossed dipole trap and varied the magnetic field by changing the current through the Feshbach coils. Holding the atoms at this field for $100\,\mathrm{ms}$ and measuring the number of atoms with absorption imaging at zero magnetic field resulted in an asymmetric loss feature (figure 4.8). In the vicinity of the resonance we expect a strongly enhanced three body loss of atoms [124]. The applied current was measured with a current transducer [2]. The asymmetry of the obtained loss feature can be explained with the finite temperature of the system. The resonance condition to produce a molecule was hit when relative kinetic energy of the colliding atoms in states $|1\rangle$ and $|2\rangle$ with relative momentum k_{rel} is equal to the energy difference of the molecular state relative to threshold energy given by the magnetic field of the Feshbach resonance:

$$\frac{\hbar k_{\mathrm{rel}}^2}{2m} = E_{\mathrm{mol}} - E_{\mathrm{threshold}} = 2\mu_B \left(B - B_{\mathrm{res}}\right) \tag{4.2}$$

If differences of the magnetic field relative to the resonance field are positive this energy can be equalized by collisions with larger relative momenta and therefore temperatures, whereas the resonance is sharp for magnetic fields B smaller than the resonance B_{res}. We located the maximum loss at $213.62(1)\,\mathrm{A}$. In absence of a Feshbach current, the magnetic field was zeroed via microwave spectroscopy [135] by applying current to offset coils surrounding the setup.

[2] IT 700-SB current transducer by LEM

The knowledge of this second point enabled us to calibrate the magnetic field with a precision of $\pm 0.2\,\mathrm{G}$. With knowledge of the magnetic field, the precise results of Selim Jochims group

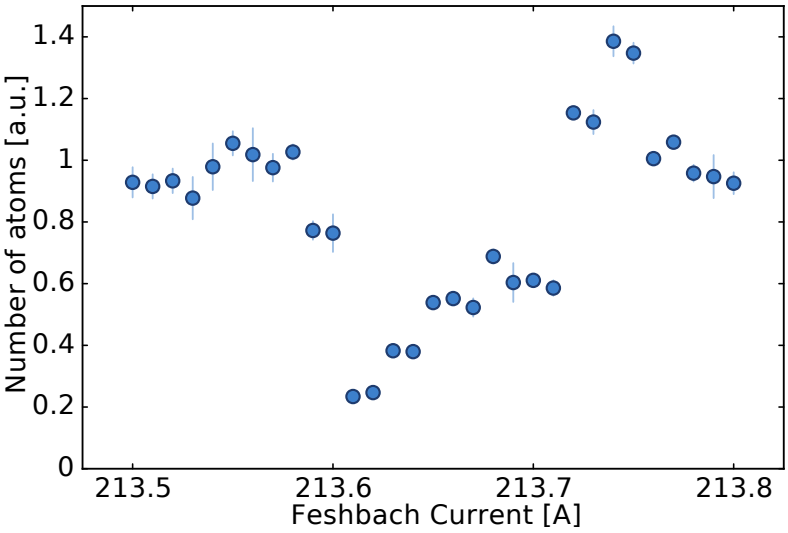

Figure 4.8: **Magnetic field calibration by locating the narrow Feshbach resonance.** The figure shows the leftover number of atoms after keeping them trapped for 100ms in a two-dimensional trap in the vicinity of different magnitudes of the homogeneous offset field. The narrow Feshbach resonance is identified via a strongly enhanced three body loss rate which shows up as a strongly reduced number of atoms.

[123] were used to convert the magnetic field to a s-wave scattering length based on the broad resonance of the states $|1\rangle$ and $|2\rangle$. The onsite interaction U was then calculated using the Wannier function of the lowest band for our measured lattice depths [136]. Because of the large lattice spacing, we expect only small corrections to the interaction strength due to multi-band effects [137].

Chapter 5

Spin and charge resolving quantum gas microscope

As pointed out in the theory section, for entropies lower than $s < \ln(2)$, the full characterization of the Hubbard Hamiltonian requires not only knowledge of the charge degrees of freedom but also the spin distribution. Since for our system the spins are decoded in two different hyperfine levels of the ^{6}Li $F = 1/2$ electronic ground state, an experimental method that distinguishes these two states during the imaging process had to be developed. Other groups have tried to circumvent this point by removing one of the spin components optically already before the imaging process while not disturbing the other. Taking one image of each spin component and one with both components in the lattice, allows them to extract information about the distribution of spins as well as singly occupied sites [138, 142]. In contrast to that, the method we chose allows to image both spin components in one shot, deterministically separating different spins spatially before imaging. Since possible doubly occupied sites are also split before the imaging process, this avoids the common problem of parity projection due to light assisted collisions [65, 66]. In this way we not only access the distribution of spins but also to the full charge statistics, including doubly occupied sites. Technically we make use of an optical superlattice in combination with opposite magnetic moments of the two hyperfine levels representing the different spins. In the following chapter I will summarize the required technical ingredients and show how a single component spin polarized gas was used to benchmark the fidelity of the spin separation process. Beforehand, I will recapitulate the basic working principle of our charge resolving quantum gas microscope [79, 83] and update the obtained size of the point-spread-function of a single atom. Additionally, a method to avoid parity projection by employing strong repulsive interactions during the transfer into the Pinning lattice, will be discussed.

5.1 Charge resolving quantum gas microscope

5.1.1 Working principle of our quantum gas microscope

To probe lattice gases of ^{6}Li with single atom and single-site sensitivity, we performed fluorescence imaging. We collected photons which the trapped atoms scatter, with our high resolution objective ($f = 28.1\,$mm, see in figure 3.1 indicated from below). The collected photons were imaged with a lens of focal length of $f = 1700\,$mm onto a EMCCD camera [1]. The resolution of the microscope objective was independently determined before with a star test to be $\approx 1\,\mu$m [126]. Since the lattice constant of the short physics lattice component is $1.15\,\mu$m, optically distinguishing two objects which populate two neighboring sites is relaxed. However, the more challenging task was to keep the atoms trapped in their original lattice site, while collecting a sufficient number of photons during the imaging process. Atom loss or tunneling processes reduce the obtained signal to noise ratio such that the occupation of the lattice sites can not be reconstructed. To avoid, or at least minimize, these processes, we need to trap the atoms in a sufficiently deep lattice potential during the imaging process. Even exacerbating these requirements, the light mass of ^{6}Li causes fast tunneling rates ($t \propto 1/m$) and a high photon recoil energy ($E_R \propto 1/m$). Since the required trap depth to avoid these processes was around $1\,$mK per lattice axis, we could not just scale up the power in our projected lattice beams (figure 3.5). Such trap depth would either require very high powers ($> 20\,$W) or small focus of the beams. Whereas the first restriction is limited by the available laser power, the second directly limits the sizes of our ultracold samples during the physics phase, due to a stronger curved trapping potential (see equation 2.9). Therefore we implemented an additional lattice, which was only used during the imaging process. this so called Pinning lattice, which was powered by one NUFERN-1064nm fiber amplifier per axis (NUA-1064-PD-0050-D0) with nominal output of $50\,$W each. After isolation of the amplifier, beam size shaping and passing through a intensity controlling AOM (I-FS080-2S2G-3-LV1 by Gooch and Housego) the remaining power was shined to the position of the atoms. By directly retro reflecting each beam onto each ingoing component respectively we got a tightly confining 3-dimensional Pinning lattice with a lattice constant of $a_{\mathrm{PL}} = \lambda/2 = 532\,$nm and size $w_{\mathrm{x,y,z}} \approx 58\,\mu$m. For stabilized powers of $20\,$W per beam the on-site trap frequency was $2\pi \cdot 1.42\,$MHz. Each physics lattice site is oversampled by minimum eight Pinning lattice sites. Together with the separation of the lattice during imaging and physics phase, this allows for arbitrary choice of the investigated geometry. The strong oversampling also allowed to avoid parity projection during the imaging process. This fact was already described for a polarized single component gas in the thesis of Ahmed Omran [83] and was extended in the framework of this thesis to interacting two component gases (chapter 5.1.2). After the atomic sample was prepared at its final physical state, we froze the distribution by quickly ramping the physics lattice to its maximal depths of $V_i = [45, 47, 178]E_R$, measured in their respective recoil energies. Afterwards the atoms were transferred into the Pinning lattices, ramped to reach the maximum on-site frequencies. Since ^{6}Li does not provide an appropriate

[1] EMCCD, ProEM1024 by Princeton Instruments

fine structure to allow for usual sub-Doppler cooling mechanisms [65, 66] to cool the atoms during the imaging process, we applied degenerate Raman sideband cooling [75, 77, 139, 140]. The ratio between a single photon recoil energy ($2\pi \cdot 74\,\mathrm{kHz}$) and the vibrational spacing of the harmonic trapping potential can be parametrized by the so-called single photon Lamb-Dicke parameter

$$\eta_1 = \sqrt{\frac{\hbar k^2}{2m\omega_{\mathrm{trap}}}} \approx 0.23 \ , \tag{5.1}$$

provided necessary conditions for Raman-sideband cooling. The large depth of the Pinning lattice not only provides resolved vibrational states for Raman sideband cooling, but moreover to suppresses tunneling events during the imaging process. Tunneling rates are not negligible anymore when an atom spends some time in a highly excited band of the Pinning lattice, since tunneling rates exponentially grow with the number of the band excitation. A detailed overview about the Raman sideband-cooling is provided in [79]. During exposing the EMCCD camera for 1 second we collected about 450 photons per atom which results in a great signal to noise ratio (see **A** in figure 5.1). In contrast to the thesis of Ahmed Omran we reconstructed the lattice population with an accelerated Richardson-Lucy deconvolution algorithm [141]. We feed the algorithm with our obtained point-spread function (PSF) from 1000 averaged realizations, with Gaussian widths of $\sigma_1 = 314\,\mathrm{nm}$ and $\sigma_2 = 363\,\mathrm{nm}$ along the principle axes (see **C** in figure 5.1). The measured size of the PSF is smaller than the one we used in our first publication [79, 83]. The reduced size of the PSF improved our imaging fidelity substantially, which allowed to reduce the exposure to 500 -$700\,\mathrm{ms}$. We estimated the fidelity of the atom number sensitive detection from the overlap of the peaks in the counting statistics (see **E** in figure 5.1). The fidelities were determined by fitting the peaks with Gaussian and calculating their overlap. The segregation of the $n = 0$, $n = 1$ and $n = 2$ peak was good enough to reach imaging fidelities of $> 99\%$ and 95% of singly and doubly occupied sites, respectively. The main limitations of the detection process are due to residual tunneling events of the atoms during the Raman-sideband cooling, which are caused by still too small Pinning lattice depths, technically limited by currently available output powers of $1064\,\mathrm{nm}$ fiber amplifiers.

5.1.2 Avoiding parity projection

Obtaining the full number statistics of the lattice occupation is one of the central aspects of quantum gas microscopy. Whereas imaging empty and singly occupied sites has been shown in multiple experimental setups, light induced collisions inhibited the direct imaging of doubly occupied sites, showing up as an empty site [65, 66, 74–77]. Therefore the obtained density distributions only reflect the parity. To avoid this so called parity projection due to light induced collisions, two atoms which populate the same lattice site need to be transferred into two different sites before starting the imaging process. One approach is realized by trapping them already in the long component of an optical superlattice configuration along one direction and splitting the atoms into the two corresponding short scale components. We realized this technique

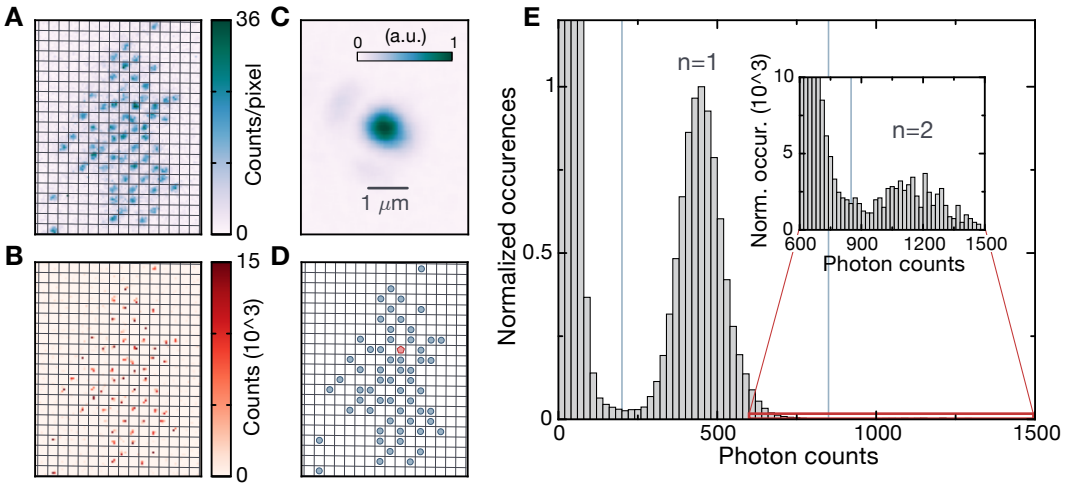

Figure 5.1: **Reconstruction algorithm. A** Raw fluorescence image backgrounded with a grid indicating the short-short lattice configuration on which the occupations are reconstructed. The color scale indicates the number of detected photons per pixel on the CCD chip. **B** Measured PSF from 1000 shots with Gaussian widths of $\sigma_1 = 314\,\mathrm{nm}$ and $\sigma_2 = 363\,\mathrm{nm}$ along the principle axes. **C** Image after applying the Lucy-Richardson deconvolution algorithm [141] with the PSF from B. The color scale represents the counts per pixel after this deconvolution. **D** Reconstructed lattice occupation. Empty sides are left empty, singly and doubly occupied sites are colored (blue and red respectively).**E** Histogram of the recorded number of occurred photon counts. The separation of empty and singly occupied sites is excellent and results in a reconstruction fidelity better than 99%. Singly and doubly occupied sites are harder to distinguish due to the low number of doublons, but still reveal a reconstruction fidelity of 95%.

even spin selectively (see section 5). Another possibility is provided by using an additional, completely independent, lattice potential, with shorter lattice constant compared to the physics lattice. In our setup the Pinning lattice ($a_{\mathrm{PL}} = 532\,\mathrm{nm}$), into which we transfer the atoms before imaging, oversampled even the short physics lattice constant of $1.15\,\mu$m. We showed already for a spin polarized sample that doubly occupied sites are always split into two different Pinning lattice sites when its potential is adiabatically ramped up [79, 83]. In this case Pauli blocking forces atoms on doubly occupied sites to populate different energy bands. For the parameters of the frozen physics lattice $V_i = [45, 47, 178]E_R$, the band gap is on the order of $72\,\mathrm{kHz}$. When ramping up the Pinning lattice, the energy levels of the states are initially dominated by the physics lattice parameters. When the Pinning lattice depth is increased further, the energy level of the neighboring pinning lattice site crosses the energy of a doubly occupied Pinning lattice site. If the Pinning lattice potential is ramped up slow enough compared to the gap, the system follows adiabatically into the state of lower energy. The doubly occupied physics lattice site is split into two Pinning lattice sites. Since the resolution of the microscope is only $1\,\mu$m

compared to the Pinning lattice constant of $532\,\text{nm}$, the atoms are assigned to the same physics lattice site. As shown in figure 5.1 a doubly occupied site is accompanied with nearly twice the fluorescence counts of a singly occupied site. In case of a two component mixture the larger fraction of doubly occupied sites contains two atoms in different states. Therefore the Pauli blocking does not apply and doubly occupied sites are energetically degenerate when the interaction between the two states is zero. But as soon as the interaction is finite and repulsive the degeneracy is lifted and a doubly occupied site is increased by the interaction energy U. Since the occupation in the physics lattice does not change anymore when the distribution is frozen by ramping its depth to the maximum, the interaction parameter can be ramped to a value which is on the same order of magnitude as the band splitting in the case of a polarized gas. For the lattice parameters of the frozen physics lattice $V_i = [45, 47, 178]E_R$ and an interparticle scattering length of $a_s = +3000\,a_B$ the interaction energy is $39\,\text{kHz}$. The required timescale of the Pinning lattice ramp was therefore expected to be larger than in the case of a polarized gas. In a test measurement, we set the interparticle interactions to nearly zero (Feshbach field at $527.8\,\text{G}$) and tuned the evaporation and trapping potential parameters at the end of the preparation sequence (see 4.1) such that we expected a band insulating core in the center of the trap with an average filling of $n_{i,\sigma} = 1$ per spin state σ. When applying strong repulsive interactions during the transfer to the Pinning lattices, we could suppress major amount of the parity projection if the Pinning lattice is ramped up slow enough (figure 5.1.2). We compared the number of imaged doublons for the case of strong repulsive and zero interparticle interactions. To benchmark the number of doublons and holes we reference the measurement results to a $n = 1$ Mott insulator realized in the short-short lattice configuration at strong repulsive interactions.

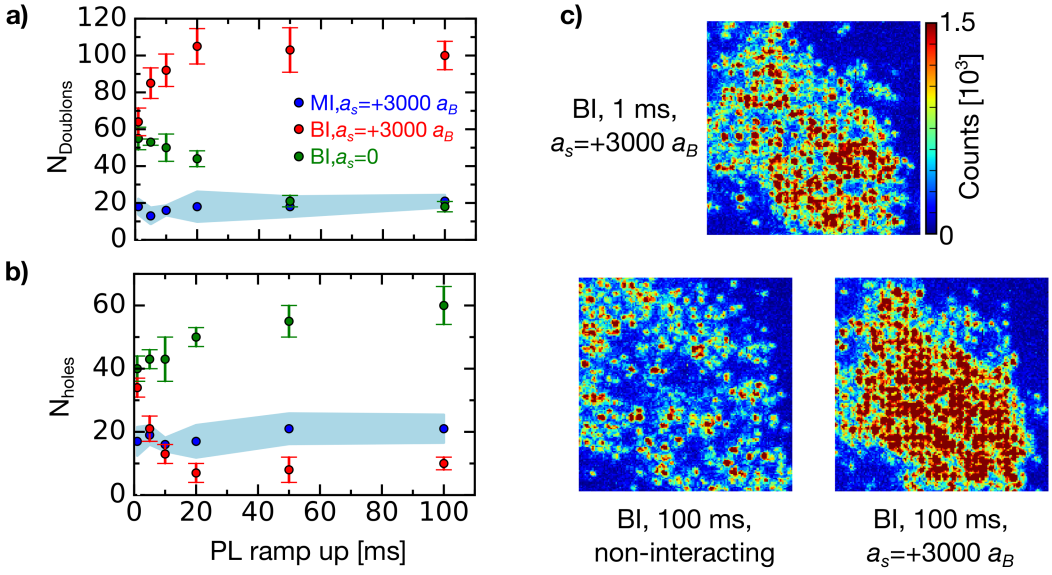

Figure 5.2: **Suppressing parity projection by strong repulsive interactions.** We prepared clouds which populated about $N = 120$ lattice sites. **(a)** We investigated the number of detected doubly occupied sites of a non-interacting two component lattice gas depending on applied strong repulsive interactions during the transfer into the Pinning lattice. Additionally the influence of the Pinning lattice ramp duration was checked. As a reference a nearly perfect half filled sample (blue data, Mott insulator at strong repulsion) is shown. It is clearly observable that the number of detected doublons increases and finally saturates when applying strong interactions (red data) and ramping up the Pinning lattice slow enough ($> 20\,$ms) whereas for zero interactions (green data) the number of detected doublons decreases. **(b)** At the same time the number of detected holes behaves reversed. Strong repulsive interactions in combination with slow enough ramps avoid the production of artificial holes by parity projecting originally doubly occupied sites. **(c)** Raw CCD fluorescence images for three extreme cases of a and b. The effect of interactions in combination with slow ramps is clearly visible. The color scale, representing CCD fluorescence counts, is set such that it saturates for doubly occupied sites.

5.2 Spin resolving quantum gas microscope

For interacting two component gases below entropies per particle of $s = \ln(2)k_B$, the spin degree of freedom is not random anymore [86, 88, 119, 120] and the knowledge about their distribution is required to characterize the full Fock space of the system. In the following section the extension of our quantum gas microscope to the ability of identifying the spin of an imaged atom is presented. The development was driven in parallel to two other groups [138, 142], who succeeded in reconstruction of the spin distribution by removing one of the spin components optically before imaging them with the quantum gas microscope. In contrast to this approach we kept both spin components but separated them spatially by a Stern-Gerlach like splitting process into different sites of double wells before imaging [38, 58]. The upcoming subsections describe first the general idea of the splitting process and inform about possible lattice configurations as well as possible measurement results. The subsequent subsections concentrate more on technical details such as the experimental implementation as well as the benchmarking of the splitting process.

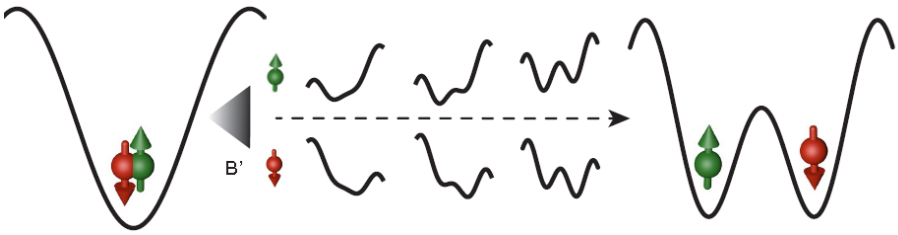

Figure 5.3: **Sequential view on the splitting process on an exemplary doubly occupied site.** Two atoms, one of spin up and the other down, are trapped in a large spaced physics lattice site. Due to their opposite magnetic moments the different spin states experience a spatially dependent energy offset after ramping up the magnetic field gradient B'. With a relative phase of $\varphi_{\text{rel}} = 0$, which guarantees symmetric double wells (see figure 3.4), the short scale component of the superlattice is adiabatically ramped up while the long scale component is ramped down. Given this combination of the symmetric double wells and the spatial spin-dependent energy offset, the spin states experience an effectively tilted lattice potential of opposite direction, transferring the spin down component in the left site and vice versa.

5.2.1 Spin resolution through spatial spin separation

The described splitting scheme works for lattice configurations which constrain the atoms to populate only the long component of the superlattice in the y-direction. The chosen lattice configuration along the x-direction played no role. Before and after the splitting process every atom can be uniquely assigned to a single site of the long lattice component along the y-direction. To gain information about the spin of an atom we made use of our superlattice potentials. We separated the two spin components spatially into different sites of symmetric double wells before

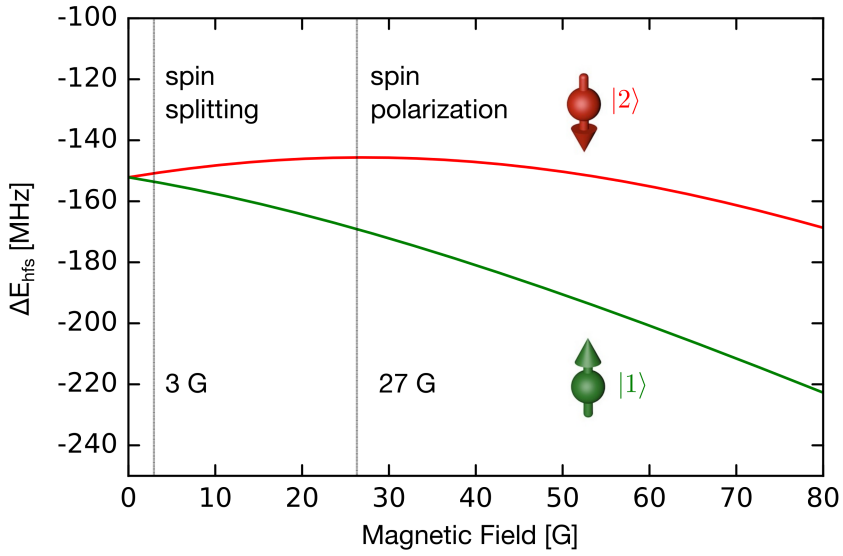

Figure 5.4: **Breit Rabi diagram of the two lowest hyperfine levels. Spin separation:** In the linear Zeeman regime (approximately up to 10 G) the magnetic moments of the two spin states (decoded in green and red) are of opposite sign but same magnitude. A magnetic offset field of about 3 G was set in addition to the magnetic field gradient B' to persist the quantization axis during the splitting process. **Spin polarization:** To benchmark the splitting process (see subsection 5.2.5) we used a spin polarized sample. We polarized the sample at 27 G homogeneous offset field where the magnetic moment of the down spins vanishes. By applying a magnetic field gradient on top of the offset field we polarized the sample by reducing the trap depth of the up-spin to zero [79].

imaging them with the quantum gas microscope. We distinguish the two different sites of the double well by making use of the opposite magnetic moments of the used spin states in the linear Zeeman regime (figure 5.4). By applying a magnetic field gradient along the y-direction the atoms experienced a spin dependent force of the same magnitude but opposite sign. This leads to effectively tilted double wells when ramping up the the short component while reducing the long component of the optical superlattice along the y-direction (see figure 5.3). If the induced Zeeman-shifts are sufficiently high compared to fluctuations of the relative superlattice phase, spin down atoms are transferred to the left well and vice versa with unity probability.

Afterwards the trapping lattice potentials are ramped up to their maximum value and the atoms get transferred into the Pinning lattices and our usual imaging fluorescence imaging technique with the quantum gas microscope starts (section 5.1.1). Figure 5.5 shows the general process and illustrates typical spin resolved and non spin resolved images of decoupled one-dimensional Hubbard chains, which were also the main physical system studied in the framework of this thesis (chapter 6).

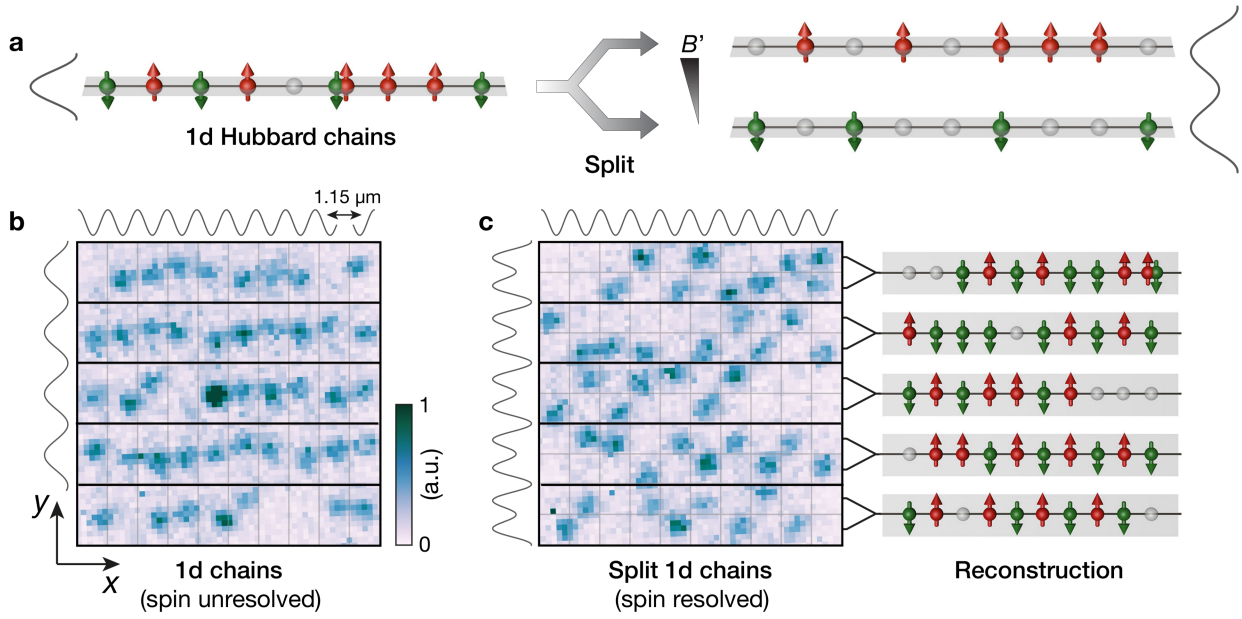

Figure 5.5: **Working principle of the spin and density resolved detection (a)** Schematic of spin resolved imaging. Each site of a Hubbard chain was split spin-dependently into a local double well potential. During the splitting process a magnetic field gradient B was present to separate the two spins spatially. This allows for the simultaneous detection of $|\uparrow\rangle$ (green), $|\downarrow\rangle$ (red) spins, doublons (red and green spins overlapping) and holes (gray spheres) and thus for a full characterization of the Hubbard chains. **(b)** Typical fluorescence image of atoms in five mutually independent one-dimensional tubes imaged prior to splitting. The lattice potentials are indicated by the black lines next to the images with a spacing along the tubes oriented in x-direction of $1.15\,\mu$m and a transverse inter-tube separation of $2.3\,\mu$m. The increasing fluorescence level is shown by darker colors in relative units as represented by the color bar. Our imaging slightly displace the atoms from their original positions and also allows for the detection of doubly occupied sites (saturated signal in the center) [79]. **(c)** Typical image with spin resolved detection. A superlattice in y-direction (indicated on the left of the image) was used to split each chain in a spin dependent manner. The $|\downarrow\rangle$ spins were pulled down, while the $|\uparrow\rangle$ spins were pulled upwards. The right image illustrates the reconstructed Hubbard chains.

5.2.2 Power of a spin and density resolving quantum gas microscope

Realizable lattice configurations

As already mentioned, the class of lattice systems we were able to investigate with spin resolution was limited to systems which populate only the long lattice component along the y-direction whereas we are free to choose the superlattice configuration along the x-direction (see figure 5.6).

Even within these configurations two-dimensional strongly correlated systems can be realized. Since we want to observe spin-spin interactions in our systems, two requirements have to be fulfilled. The interactions should be the dominate the kinetic energy of the atoms, but at the same time the superexchange coupling which drives spin-spin interactions ($J \sim 4t^2/U$) needs to remain finite. A large lattice spacing of $d_{\mathrm{l,y}} = 2.3\,\mu$m leads to reduced tunneling rates, since the overlap of the Wannier-functions is weakened. In the case of ^{6}Li, the light mass counters this

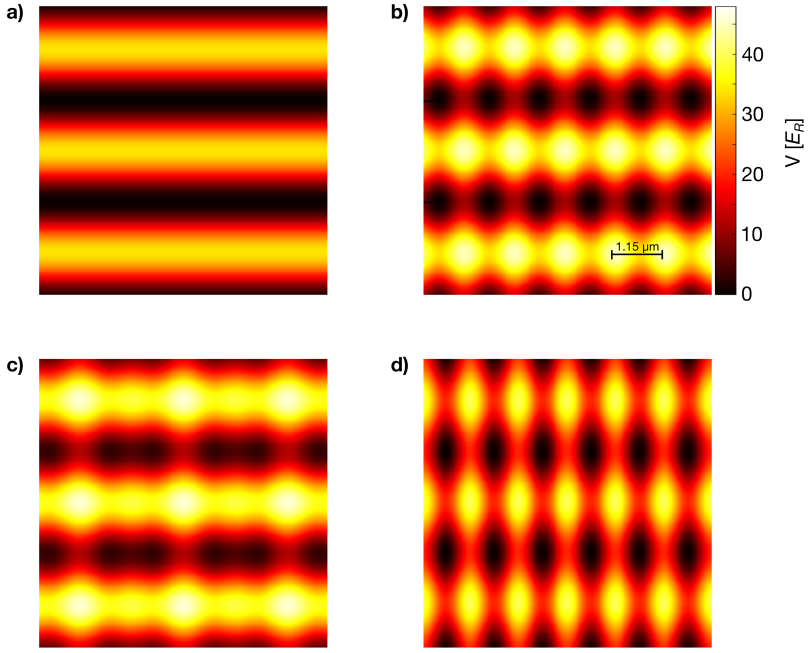

Figure 5.6: **Density plots of exemplary lattice configurations possible to investigate with our spin resolving quantum gas microscope. a)** Decoupled one-dimensional tubes with spacing of $d_{\mathrm{l,y}} = 2.3\,\mu$m. This system would require fast freezing within short (x) lattice sites prior to the splitting process. **b)** Decoupled one-dimensional Hubbard chains with short intra lattice spacing of $d_{\mathrm{s,x}} = 1.15\,\mu$m (used for all measurements in chapter 6) **c)** Decoupled one-dimensional double wells or coupled double wells. **d)** Two dimensional lattice in the configuration $d_{\mathrm{s,x}} = 1.15\,\mu$m, $d_{\mathrm{l,y}} = 2.3\,\mu$m.

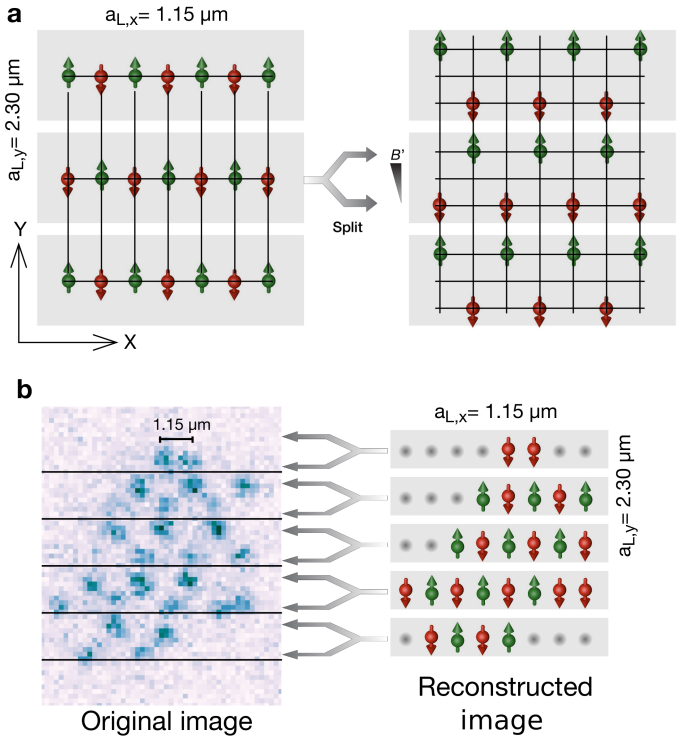

Figure 5.7: **View on detection of two-dimensional antiferromagnetic correlations. a:** Perfect pattern of two-dimensional Néel-state in the short (x)-long(y) lattice configuration via the one-dimensional vertical splitting technique. **(b)** Single experimental realization of almost perfectly ordered small cloud in the short (x) -long (y) lattice configuration. The two lattice axis set to realize final tunnel couplings of $t_{x,y} \approx 200\,\mathrm{Hz}$.

effect ($t \sim 1/m$) and sufficient tunneling rates, at trap depths which are still large compared to the temperatures of the systems, were experimentally realized. The relatively low confinement parameters to reach sufficient tunneling rates increases the size of the on-site wavefunctions. Following equation 2.8, interparticle interactions are strongly reduced. Again, the characteristics of ^{6}Li (see figure 3.3), allowing to tune the on-site interactions via Feshbach resonances, enable to access to the strongly correlated regime. In first experimental efforts antiferromagnetic correlations in two dimensions with lattice configuration 5.6 **(d)** were realized. In figure 5.7 the perfect theoretically expected and an experimentally recorded pattern are shown.

Once the occupation and the spin of a lattice site is measured, there is in principle no limit to evaluate any arbitrary correlation function. The relevant correlators which are under investigation in our systems are illustrated in figure 5.8. A pure spin-spin correlator versus the distance can be calculated (figure 5.8 **(a)**), as well as local and non-local density density correlations (figure 5.8 **(b)**). However, the full strength of the microscope is played, when the read-out spin and density distributions are combined. For example the spin-spin correlations with distance two

can be evaluated under the constraint of a hole located in between these two sites. Such spin-hole-spin correlations are expected to behave different in one and two dimensions (see figures 2.4 and 2.3). In contrast to condensed matter systems, we can not only tune the dimensionality of the system, but also reconstruct the relevant multi-point spin-hole-spin correlations with our spin and charge-resolving quantum gas microscope.

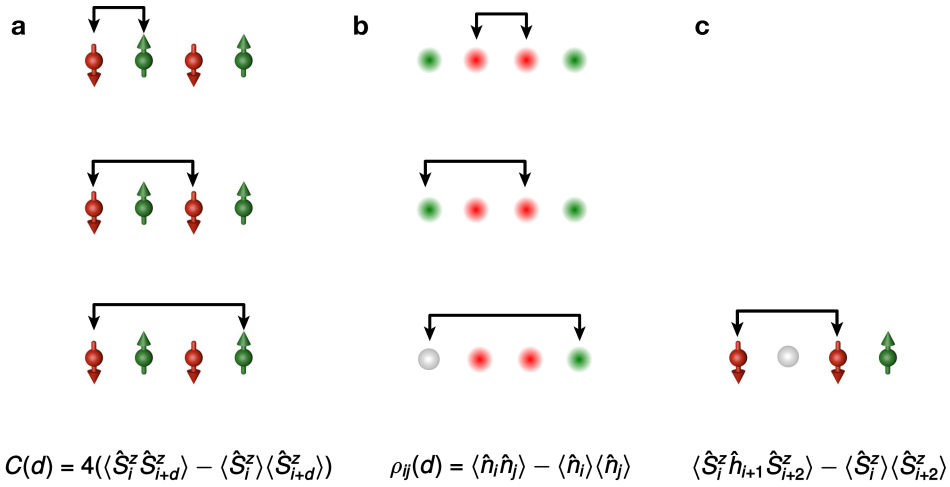

Figure 5.8: **Possible correlator in one dimension** After assignment of the local occupation and spin the correlation functions can be calculated. **(a)** Correlations in the spin sector versus the distance. The uncorrelated part is subtracted. **(b)** Density-density correlations. Since the full number statistics can be measured directly, no assumptions regarding particle hole symmetry have to be used. **(c)** Spin-hole(excitation)-spin correlations. Measures the influence of a hole on the d $= 2$ correlator. All correlation functions shown here can be easily extended to two dimensions.

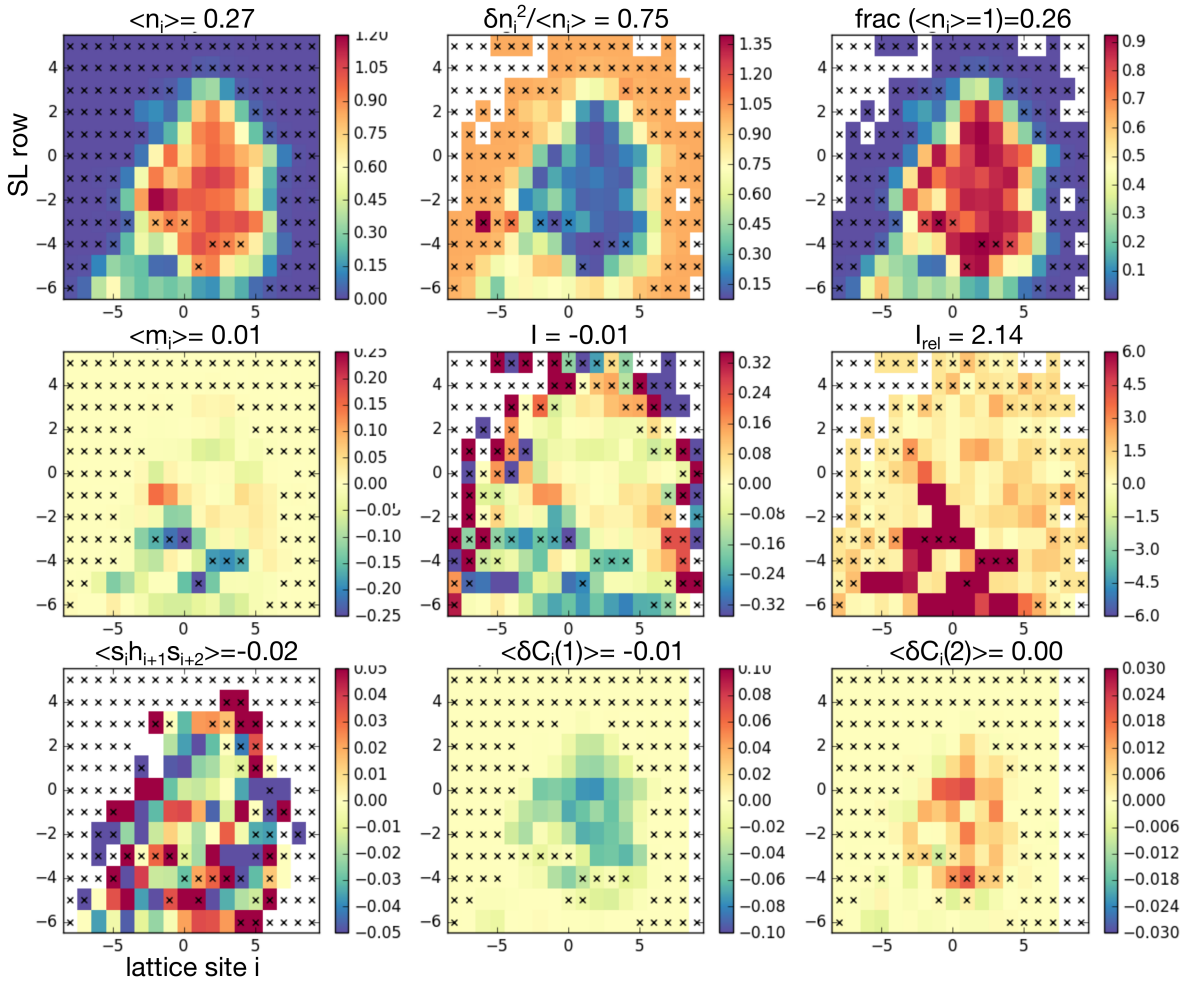

Figure 5.9: **Full potential of the quantum gas microscope- selection of relevant lattice sites** The average occupations and spins of each lattice site i per row can be used to filter the data. Some measurements in 6 were filtered depending on the average filling (top,left). If the average population was outside the filter the site was dismissed for the statistical analysis. In the same way the particle number fluctuations (top, center) can be used to the filter the data. Reduced fluctuations are a sign for insulating phases. Together with the average filling around one a Mott-insulating phase within the system can be preselected. The second row illustrates for data selection which assesses the local fidelity of the splitting process. If the average magnetization m_i (middle, left) is non-zero this is a sign for local defect of the lattice potential, like an interference fringe which locally prohibits a symmetric double well for spin splitting. The imbalance I (middle,center) focus on chains and captures global phases gradients and errors. The bottom row shows exemplary read out of different correlators after filtering. Maps showing the occurrence of spin-hole(doublon)-spin events (left), the most prominent regions of nearest (center) and next-nearest neighbor correlations.

5.2.3 Influence of phase errors on spin splitting process

As already mentioned in 3.2.4, the induced tilt of a double well due to phase fluctuations needs to be smaller than the state dependent tilt which we imprint with the magnetic field gradient. If this is not the case an atom will be transferred to the wrong site, resulting in a wrong spin detection. We benchmark the fidelity in section 5.2.5 with a single spin component sample. In contrast to the lattice independent spatial energy offset due to the gradient, the energy offset due to fluctuations of the relative phase depend on the depth of the lattice components. For a set of lattice ramps (which actually correspond to the ones we finally used for our measurements in [82], see figure 5.11) the evolution of the energy offsets was calculated for the cases of rms-phase fluctuations of 50 mrad and 200 mrad 5.10. In addition the evolution of the inter- and intra double well tunnel couplings are shown. The couplings between different double wells have to be very small compared to any timescales of the ramp durations, to avoid mixing of different physical lattice sites. The couplings in a double well itself has to be decreased slowly so that the atom is given enough time to undergo a tunneling process. The transition probability can be calculated from Landau-Zener theory, whereas the temporal evolution of the energy states corresponding to the left and the right site has to be known. In the extreme case of suddenly turning on the short lattice potential to a depth which does not allow for tunneling anymore, an atom would just be projected with nearly equal probabilities to the left and the right site of a double well. The lattices have to be ramped adiabatically, whereas the timescale is set by the energy gap of the adiabatic crossing between the left and the right site. The evolution of the tunneling parameters as well the energy offsets due to phase fluctuations, which set together with the magnetic field offset the coupling between the left and the right site, were calculated for a simple double well potential using mathematica.

The system can be handled as a two level problem, assuming the spin of the atom such that the magnetic field lowered the energy of the right site. The evolution of the states as well as the probability for an atom to end up on the right site (successful splitting) can be calculated. For an adiabatic sweep the Landau-Zener formula [143] is used to obtain quantitative results. The system is defined as follows: The left and the right site are effectively coupled with an Rabi frequency

$$\Omega_{\text{eff}} = \sqrt{t_{\text{short}}^2(t) + \Delta_{\text{tilt}}^2(t)} \ , \tag{5.2}$$

whereas the time-dependent tilt of the double well is assumed to be lowered by phase fluctuations $\Delta_{\text{tilt}}(t) = \Delta_B - \Delta_{\text{phase}}(t)$. Even if the directions of the tilts due to the magnetic field and the phase fluctuations would agree with each other for one spin component, the situation would be maximally bad for the second component. The adiabaticity criterion is fulfilled if the coupling Ω_{eff} is larger than the temporal change of the mixing angle, which describes the contributions of the left and the right lattice site to the total wavefunction [144]:

$$\Omega_{\text{eff}} >> \left| \frac{d}{dt} \left(\tan^{-1} \left(\frac{\Delta_{\text{tilt}}}{t_{\text{short}}} \right) \right) \right| \ . \tag{5.3}$$

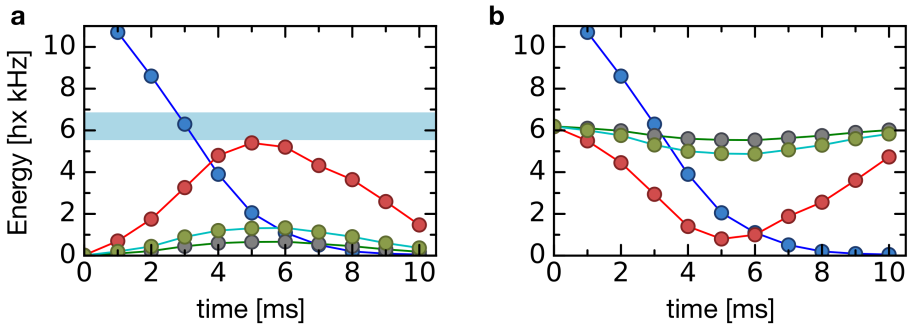

Figure 5.10: **Influence of phase fluctuations on the splitting process. a:** Shown is the evolution of the tunneling energy within double wells (blue) for linear ramps of 10ms duration of the short ($0E_R \rightarrow 17E_R$) and long superlattice component ($84E_R \rightarrow 10E_R$) along the y-direction. Additionally the corresponding evolution of the tilt energy Δ_{phase} is plotted for relative phase errors of $\varphi_{\text{rel}} = (25, 50, 200)$ mrad (grey,green,red). As a reference, the lattice independent spatial energy offset of $\Delta_B = (6.2 \pm 0.6)$ kHz due to the magnetic field gradient, is illustrated in light blue. **b:** Temporal evolution of combined tilts $\Delta_{\text{tilt}} = \Delta_B - \Delta_{\text{phase}}$ for the same errors of the relative phase (same color coding). When hitting the resonance condition of equal coupling and tilt (crossing points with the blue curve), the influence of the phase fluctuations are apparent: In case of strong phase fluctuations (red) the resonance is passed very quick, even though the residual coupling (blue) is weak. For small phase fluctuations instead, the change of the tilt is very small and the corresponding coupling at is still very strong, resulting in an effective transfer of the atom.

For the regions of the ramps where these condition is met, the Landau-Zener formula,

$$P_{\text{r}} \approx 1 - \exp\left(-\pi \frac{\omega_{\text{eff}}^2}{2\dot{\Delta}_{\text{tilt}}}\right) \tag{5.4}$$

gives the probability of a transfer to the right site. For the three values of the phase fluctuations one gets therefore:

$$P_{\text{r}}(200 \text{ mrad}) = 0.49 \tag{5.5}$$
$$P_{\text{r}}(\ 50 \text{ mrad}) = 0.91 \tag{5.6}$$
$$P_{\text{r}}(\ 25 \text{ mrad}) = 0.99 \tag{5.7}$$

These number show already, what was expected from the qualitative picture. In the case of 200 mrad the double wells are not tilted on average and the probability to end up on the left or the right site is equal. Only if the energy scale due to phase fluctuations is much smaller than the tilt due to field gradient, the probability increases towards one. Technically one should not only consider phase fluctuations but also a mismatch of the lattice constants of the superlattice. If they are not commensurable it leads to a phase gradient along the lattice potential. Typically

our systems extend over ten one-dimensional tubes along the y-direction. Assuming a maximal allowed phase gradient of ± 25 mrad between the central and the most outer chains to obtain a successful splitting processes in the whole cloud, the parallelism of the lattice components we sent into the objective has to be better than $0.03°$. Since this corresponds to an alignment precision of about $10\,\mu$m, we had to fine-align on a signal of the atoms to fix the mismatch of the lattice constants (see section 5.2.5).

5.2.4 Splitting sequence and assignment of a spin

In this section, the parameters of the splitting sequence we used in the measurements of chapter 6 is given. In these experiments we investigated decoupled Hubbard chains (figure 5.6 **(b)**). The

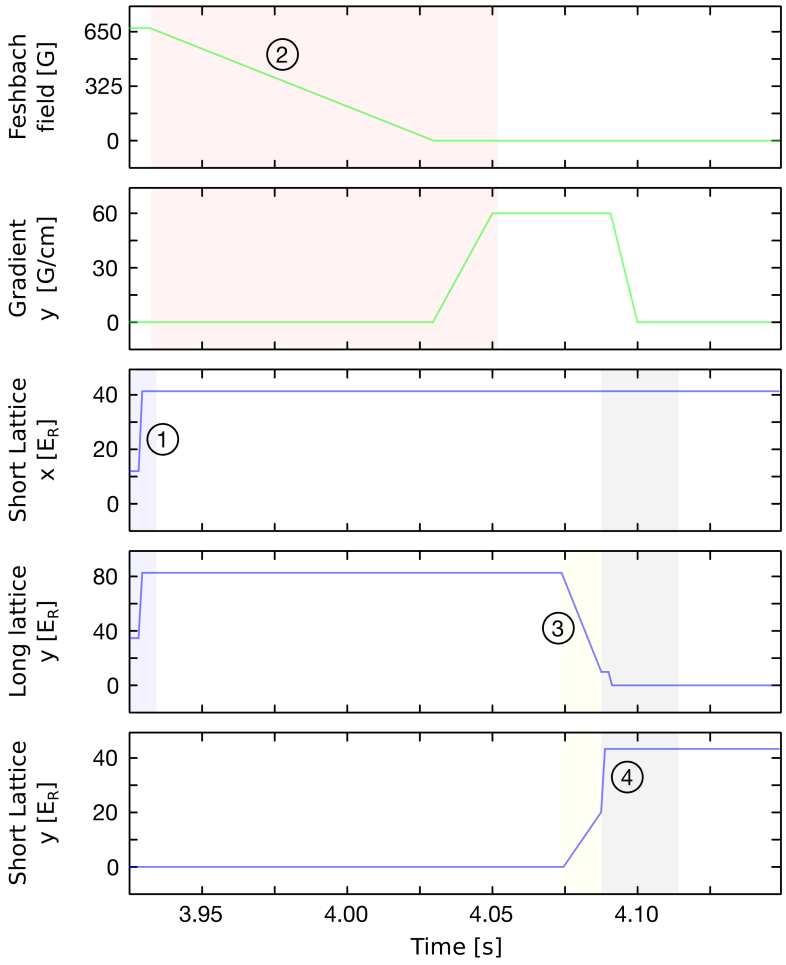

Figure 5.11: **Timetable of the splitting process.** ① Once the atomic distribution is frozen in the investigated lattice configuration (here one-dimensional tubes), ② the interactions are ramped to basically zero within 100 ms, followed by turning on the magnetic field gradient of 60(2) G/cm in 20 ms. ③ Atoms of different spins are split into different sites of local double wells by ramping up the short scale component along the y-direction while ramping down the long scale component in 10 ms. ④ Afterwards the distribution is frozen by ramping the short scale components along both directions to their maximum depth, before transferring them into the Pinning lattice and imaging them as described in section 5.1.1.

splitting sequence was initiated by freezing out the dynamics along the tubes with an abrupt (1 ms) increase of the lattice depths to $[42, 84, 278]\ E_R$ in the x- , y- and z- direction. Then we ramped down the magnetic Feshbach field to 1 G to enter the Zeeman regime, where both spin components have equal and opposite magnetic moments. The field had to be finite to persist the quantization axis, relative to which the spins are defined. We set the relative phase φ_{rel} of the superlattice potential along the y-direction (compare to equation 3.2) to $\pi/2$, ensuring the symmetric double well configuration. The magnetic field gradient was first set to $60(5)$ G/cm. The corresponding energy offset due to the Zeeman shift between the left and the right lattice wells was $\Delta E_{\text{LR}} = \pm h \times 6.2(6)$ kHz for the spin up and down value respectively. Adiabatically ramping up the short scale superlattice component with spacing $a_l = a_{\text{sl}}/2$ to $V_{\text{l}} = 17\, E_R$ in 10 ms while ramping down the long scale component to $V_{\text{sl}} = 10\, E_R$ resulted in the spin splitting. Afterwards the short scale component along the y-direction was set to its maximum value in 1 ms to avoid any tunnel coupling while the magnetic field gradient was ramped back to zero. The resulting sample was afterwards transferred to the Pinning lattice and imaged with the quantum gas microscope as described in 5.1.1. The timetable of the involved channels is presented in figure 5.11.

The resulting local distribution of atoms was reconstructed as described in section 5.1.1. Given the local occupations, we still had to assign the split atoms to their original lattice sites. This process also contains the knowledge, whether an atom was transferred to the left (spin down) or the right (spin up) site of the double well. Since the obtained density distribution is invariant under a 2π phase shift of the short lattice (compare to 3.4), a direct assignment of the spins is not possible. In addition, the absolute phase of the optical superlattice potential was drifting, which excludes it determination by comparing to reference pictures of split single component gases (see section 5.2.5). How we assigned the short component sites is shown in figure 5.12. Since the wrong choice of the absolute phase leads to an enhanced number of doubly occupied sites, we can rule out the wrong short scale site to double well assignment. The fraction of doubly occupied sites in the system was measured, skipping the splitting process, with the usual density resolving quantum gas microscope, giving full access to local and global particle number statistics. Within one long measurement set the choice of the phase stayed correct, since the absolute phase drift of the lattices was small, once the experimental system was thermalized, as shown in figure 3.8.

5.2.5 Spin separation fidelity

The process of splitting the atoms in different sites of double wells needs to be benchmarked. Besides a quantitative estimation of the transfer probability for a given phase stability 5.2.3, which was measured optically, a separation fidelity was measured directly with the atoms. The same type of measurement was also used to find the phase which ensure a symmetric double well configuration. Optical measurements of the lattice potentials before the science cell were used to calibrate the phase versus the voltage applied to the phase shifter. Since the relative phase φ_{rel} of the superlattice is set by setting the absolute phase of the short lattice component,

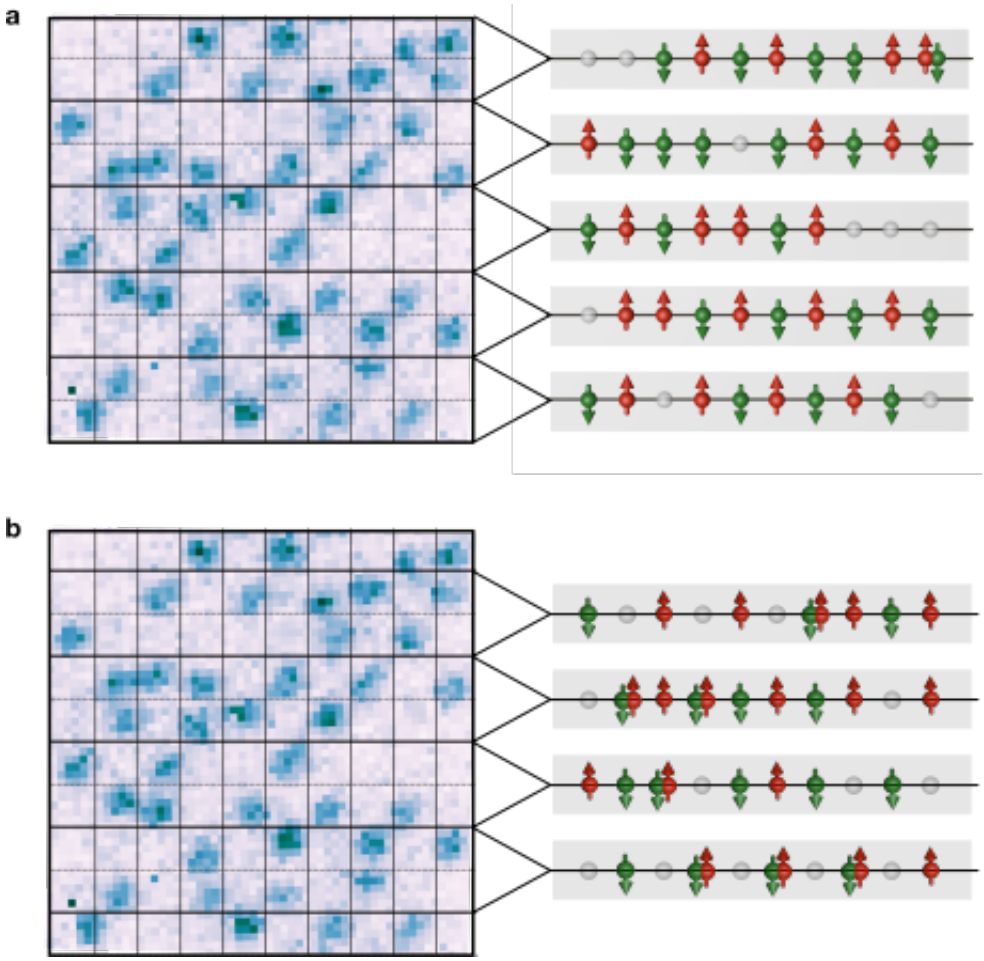

Figure 5.12: **Outcome of two different absolute phases.** The cases **(a)** and **(b)** just differ in the absolute phase we picked for the evaluation. The black thick horizontal lines represent where we determined the barrier between two chains. In **(b)** our choice lead to mixing up short scale sites which in reality belonged to different double wells. Since the read out spin only depends in which direction an atom got transferred to during the splitting process, this would lead to wrong spins. Fortunately, picking the wrong phase also increases the number of assigned doublons dramatically (for this particular picture from 1 to 7) and we can rule out this configuration, since we know from measurements with the density resolved quantum gas microscope how many doubly occupied sites on average we have to expect. The correct configuration becomes unambiguous once we take a series of shots, which have to have the same superlattice configuration as the lattices only fluctuates by a small fraction of a lattice constant from shot to shot (compare to figure 3.8).

which drifts depending on how well the setup is thermalized, the symmetric point of the double wells had to be adjusted on a regular basis. We used a single component spin polarized Fermi

gas [79] to calibrate and finally benchmark the splitting process. The fermi gas was prepared in the state $|F = 1/2, m_F = -1/2\rangle$ (spin down) after the the usual evaporation process. Ramping the Feshbach field to $27.1\,\mathrm{G}$, the magnetic moment of only the $|F = 1/2, m_F = -1/2\rangle$ state vanishes but the second spin state $|F = 1/2, m_F = +1/2\rangle$ remains still high field seeking (see figure 5.4). When lowering the transverse confinement by reducing the cross beam power in presence of an additional magnetic field gradient of $20\,\mathrm{G/cm}$, this spin-up component was selectively removed from the trap. The remaining spin down sample was transferred into the optical lattice potential. We checked the efficiency of the spill-out process independently via absorption imaging after a Stern-Gerlach separation process [145] and found no remaining atoms in the state $|F = 1/2, m_F = +1/2\rangle$. To determine the phase of the short scale lattice which represents a symmetric double well configuration, we loaded this polarized sample in the short (x)-long (y) lattice configuration. We performed the splitting process, as described, but without any magnetic field gradient present. We repeat this experiment for different values of the absolute phase of the short lattice along the y-direction. We read out the population imbalance between the left (L) and the right (R) sites of the double wells after the splitting process. The imbalance I is defined as

$$I = \frac{n_L - n_R}{n_L + n_R} \ , \tag{5.8}$$

with the number of atoms on left (right) sites n_L (n_R). Since the magnetic field gradient is zero, any tilt of a double well is directly linked to the relative phase phi_{rel}. For a tilt of zero the population imbalance should also be zero, since the energies of the left and the right site are the same, resulting in equal transfer probabilities to both sites. For strongly tilted double wells the whole population should be completely shuffled to the respective sites with lower energies. The red curve in figure 5.14 shows a typical dependence of the imbalance on the phase φ_{rel}. Initially these curves were saturating at absolute imbalances smaller than one. One reason for the offset were doubly occupied sites, which even for a spin polarized sample were not completely suppressed. Doubly occupied sites will always end up on opposite sites of the double well, when the energy level of the excited band of the long scale lattice crosses the energy level of the short scale site with higher energy adiabatically during the ramping process. Detected doublons are therefore removed from the statistics before calculating the imbalance. In addition we looked into the spatial dependence of the measured imbalance (figure 5.13). Since the quantum gas microscope provides us with single atom resolution we are in principle able to determine the symmetric phase of every single double well. As the potential landscape is not completely free of interference fringes, which change the local relative phase quiet dramatically, we could use this method to exclude certain sites from the measurement results by this method. Since the differences in the local imbalance signals reflects phase gradients along the cloud, we used the signal to fix the ratio of the lattice constants as good as possible to two. The projection angle in equation 3.1 has a horizontal and a vertical component, which we were both able to control with a motor driven mirror mount. As indicated in figure 5.13, we used the fluorescence images in the style of a quadrant photodiode. To align the vertical (horizontal) component of the angle, we zeroed the difference in the vertical (horizontal) imbalances $I_{1+2} - I_{3+4} \rightarrow 0$

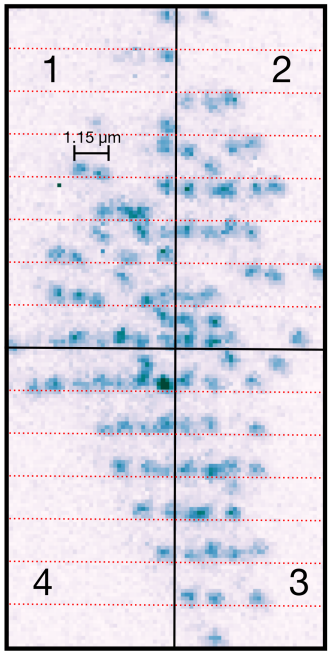

Figure 5.13: **Phase gradient due to non-perfect commensurate superlattice components** In this single shot realization of a band insulator loaded to one-dimensional Hubbard chains (the different chains are indicated by the red, thin, dashed line) after splitting into short scale sites along the vertical direction. Obviously the, the atoms in the lower regions 3 and 4 were transferred to the lower short scale site, whereas the more and more atoms got transferred to short site above, the further up the Hubbard chain was (regions 1 and 2). We used the imbalances in the regions 1 to 4 to fix the ratio of the lattice constants as perfect as possible to two. In this realization the local imbalances were deviating a lot ($I_{1+2} = 1/50$ and $I_{3+4} = 35/39$).

($I_{1+4} - I_{2+3} \to 0$). The influence of the magnetic field gradient was tested afterwards. If the phase was adjusted to the symmetric point without the gradient, turning it on should result in all atoms transferred to the lower sites of the double wells. The imbalance in this case is a measure of the separation fidelity. To quantify the fidelity we fitted the curves with a error function:

$$I(\varphi_{\text{rel}}) = A \cdot erf\left(\left(x - \varphi_{\text{rel},\pi/2}\right)/\sigma\right) \tag{5.9}$$

with the free fit parameters amplitude A, which should be close to one, the phase $\varphi_{\text{rel},\pi/2}$ giving the symmetric point of the double wells and the width σ, which is a measure of the maximum distraction of the phase one can allow for, to still realize a successful splitting process. The difference of the symmetric points with and without the magnetic field gradient display the energy offset the atoms experience due to their magnetic moments. The fidelity is given by the difference of the evaluated the error-functions for the symmetric phase $\varphi_{\text{rel},\pi/2}$ in the case of an

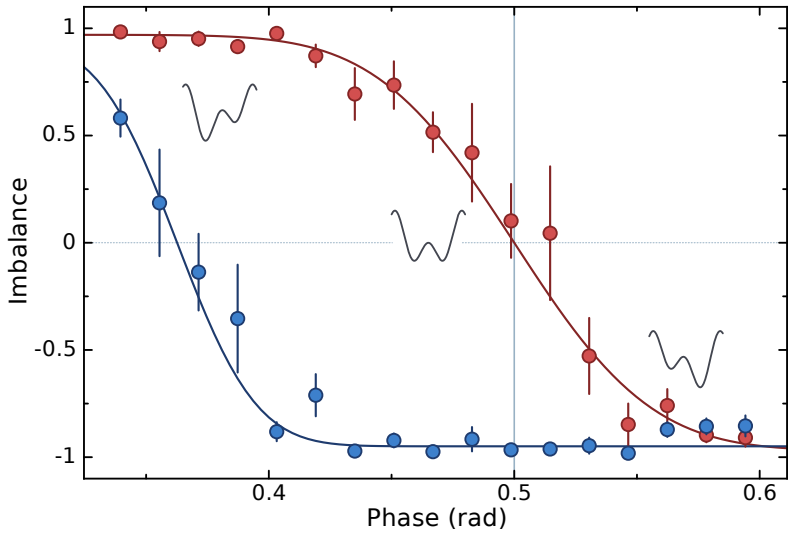

Figure 5.14: **Measured imbalance for different relative phases φ_{rel}** The figure shows the imbalance in the local double wells for the central region of the cloud versus the superlattice phase φ_{rel} which sets the symmetry of the double wells. For this measurement a spin polarized sample was used. The red data was taken without, the blue data with the magnetic gradient field of $60(5)$ G/cm, and the solid lines are error function fits to the data. The splitting was done at the symmetric point ($\varphi_{\mathrm{rel}} = \pi/2$) of the superlattice potential, where the gradient-free measurement showed zero imbalance (gray line). Taking into account our detection fidelity of 95%, the splitting fidelity of 98% is estimated from the value of the imbalance in presence of the magnetic field gradient at $\varphi_{\mathrm{rel}} = \pi/2$.

absent field gradient. We got this phase from the fit results of the case for zero field gradient (red curve). If we take into account the finite tunneling rates during the imaging process with the quantum gas microscope of 5%, which can reshuffle population from the left to the right double well sites and vice versa, we state the splitting fidelity to 98%. During the writing of this thesis the magnetic field gradient was raised to 75 G/cm which increases the robustness of the splitting process against phase fluctuations even more.

Chapter 6

Spin and charge resolved microscopy of fermionic Hubbard chains

To prove the power of our spin and density resolving quantum gas microscope we investigated one-dimensional Hubbard chains, which we prepared as described in chapter 4.1.3. Since the Hubbard Hamiltonian theoretically accessible in one dimension, we could benchmark our results to theoretical predictions which the group of Prof. Pollet obtained for our systems via Quantum-Monte Carlo (QMC) simulations 7. We read out the occupation and the spin of every lattice site and observed antiferromagnetic correlations, reaching up to a distance of three lattice sites. We investigated the behavior of spin correlations depending on the interparticle interactions U, the filling of the system as well as the entropy, which we extracted by comparing the experimental realized correlations to the QMC results. The comparison of the behavior of the density and the spin sector for different entropies and interactions shows the feasibility of our setup as a thermometric tool. Besides the interactions which were tuned via the Feshbach resonance, other experimental parameters as the occupation varied spatially within a single realization of the system. By applying filters bases on these experimentally obtained local parameters as the average filling of a lattice site, we were able to select the lowest entropy regions of the trap, which showed antiferromagnetic correlations up to three sites. Finally an evaluation of nearest and next-nearest neighbor correlations depending on the filling, which shows first hints to the influence of density excitations on antiferromagnetic correlations.

6.1 Accessed parameter regime and selection of one-dimensional tubes

The experimentally accessed parameter range is listed in table 6.1. The total number of atoms (see figure 6.1) varied slightly between $\langle N \rangle = 51$ and $\langle N = 62 \rangle$ for different values of the probed interaction U. For each interaction parameter at least 250 data points were taken. Global atom number fluctuations were in all cases smaller than shot-noise $\sqrt{N}$ (grey shaded area).

Magnetic field (G)	Scattering length (a_B)	On-site interaction U/h (Hz)	U/t	J_{ex} (Hz)
529	8	19	0.1	3200
573	200	463	3.7	134
586	272	630	5.1	99
598	353	820	6.6	76
611	445	1034	8.4	60
624	550	1279	10.3	49
637	671	1560	12.6	40
649	810	1883	15.2	33
657	904	2101	17.0	30

Table 6.1: **Experimental regime for all measurements regarding one-dimensional Hubbard chains** The final hopping strength along the tubes was fixed to $\mathbf{t_x} = h\,\mathrm{x}\,125(9)$ Hz.

This is linked to the nature of fermions and our evaporation scheme using the magnetic field gradient, which deeply cuts into the Fermi sea.

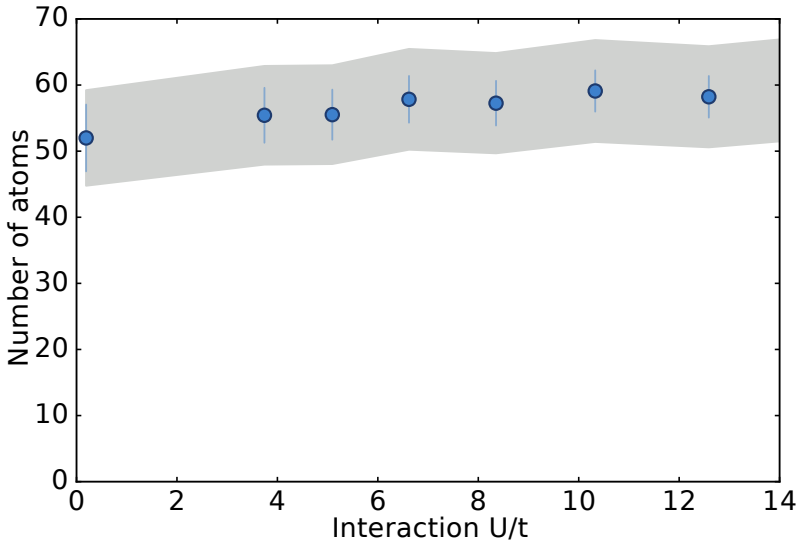

Figure 6.1: **Total number of atoms and their fluctuations** The average number of atoms was calculated by counting the number of detected atoms in every shot and averaging them over all realizations. For every value of the interaction at least 250 samples were realized. For U/t= 10 we took a high statistical sample of 1200 shots.

The typical one-dimensional tube in the center of the two-dimensional system contained about $n_{1d,c} = 9 \pm 1$ atom. On average a two-dimensional realization provided eight one-dimensional chains of slightly different length due to the trapping potential. For all measure-

ments the hopping along the tubes (x) was ramped to the same final value of $V_x = 11\,E_r$, corresponding to $\mathbf{t_x} = h\,\mathrm{x}\,125(9)$ Hz. The interaction parameter was varied, the largest probed scattering length was $a_s = 904(6)a_B$. Since the lattice constant is still large compared to this scattering length ($a_s/a_l = 0.04$), multi band effects which would lead to corrections of the Hubbard model can be neglected [137]. To every site of every realization we assigned an occupation and spin. Using both quantities, we were able to construct $n_{i,\sigma}$. Using this information we could calculate local particle number fluctuations, which we used to apply different filters to our data in the fashion of 5.9. To use only the lines with a certain filling (corresponding to the central region of the trap were the entropies are expected to be the lowest), we only took into account which showed an average filling in a certain range 6.2 **(A)**. Secondly lattice sites which showed errors in the splitting process due to local imperfections of the used superlattice potential as interference fringes, were removed 6.2 **(B)**.

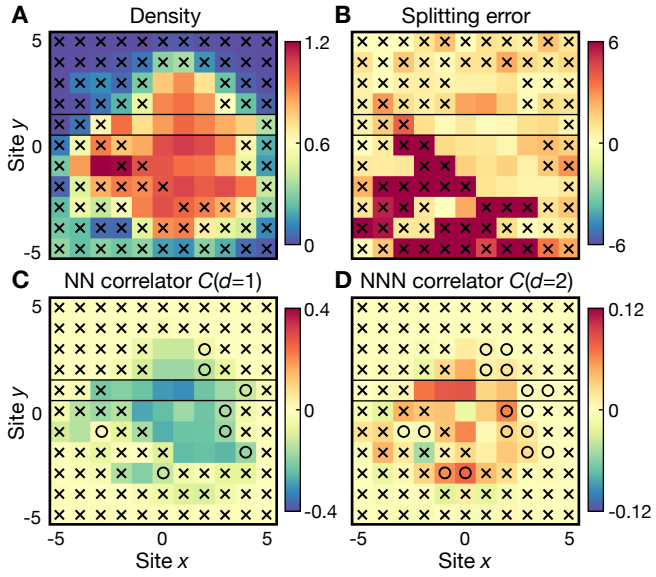

Figure 6.2: **Post selection of spin correlation data (A)** The region of interest is defined dependent on the average local density. In the shown case the filter selected only sites with densities in the range $\langle \hat{n}_i \rangle \in [0.9, 1.1]$. All other sites (marked with an **'x'**), were not considered for the statistical analysis. **(B)** On the selected subset of lattice sites, eventual errors of the splitting process were taken into the account. If the mean spin imbalance of a site i, normalized to the RMS mean, strongly deviates from zero, this is a strong sign for local splitting errors. These sites were also dismissed from the statistical analysis. **(C)** and **(D)** show the correlation maps of the nearest and next-nearest neighbor correlations, respectively. The average values of the correlations itself can also be used to filter the data.

We have extracted the following quantities out of the reconstructed lattice occupations $n_{i,\sigma}$:

- **Local number fluctuations:** with $\hat{n}_i = \hat{n}_{i,\downarrow} + \hat{n}_{i,\uparrow}$ the fluctuations are given by

$$\delta n^2 = \text{var}\left(\langle \hat{n}_i \rangle\right) / \langle \hat{n}_i \rangle \tag{6.1}$$

  . The brackets $\langle . \rangle$ denote the averaging all involved samples after the filtering.

- **Spin-Spin correlations:** The spin operator $\hat{S}_i^z$ on a site i is defined by the local occupation imbalance $\hat{S}_i^z = (\hat{n}_{i,\uparrow} - \hat{n}_{i,\downarrow})/2$. Two point spin-spin correlation functions for different distances d were built like:

$$C(d) = 4(\langle \hat{S}_i^z \hat{S}_{i+d}^z \rangle - \langle \hat{S}_i^z \rangle \langle \hat{S}_{i+d}^z \rangle) \tag{6.2}$$

6.2 Antiferromagnetic correlations in Hubbard chains

6.2.1 Charge sector

First, the charge sector was investigated. We expected the system to be for very small interactions in the metallic phase and undergo an transition to the Mott insulating state for interactions being larger than the bandwidth of the system. There are two observables which have been used to characterize the transition to a Mott insulator. A metallic state should remain compressible, whereas for strong interactions the system can not be compressed unless increasing the confinement until the underlying trapping potential overcomes the Mott gap set by the interactions and atoms could tunnel to the center of the trap to form doublons [54]. Microscopically, the number of doublon excitations should be strongly strongly suppressed [55]. Given the possibility of local access, we were able to measure directly the effect of strong correlations on the particle number statistics [78, 146, 147]. For a metallic state, the occupation of a single site follows a binomial distribution. The local occupation should scale like [78]:

$$\delta n^2 = 1 - \langle \hat{n} \rangle / 2 \tag{6.3}$$

However, when increasing U, not only fermions in the same spin state (Pauli's principle) are not allowed to populate the same lattice site, but the repulsive interactions between the two components reduces fluctuations even more. In the extreme case of infinite interactions δn^2 scales as:

$$\delta n^2 = 1 - \langle \hat{n} \rangle \quad \text{for } \langle \hat{n} \rangle \leq 1 \tag{6.4}$$

$$\delta n^2 = 3 - \langle \hat{n} \rangle - 2/\langle \hat{n} \rangle \quad \text{for } \langle \hat{n} \rangle > 1 \tag{6.5}$$

The measured fraction of doublons and holes, as well as the local particle number fluctuations are shown in figure 6.3. The presented data was filtered on the average density. The so called loose filter (blue data points) only takes into account sites with average occupations between $\langle \hat{n}_i \rangle \in [0.7, 1.3]$. Tight filtered data even constrained the average local occupations to $\langle \hat{n}_i \rangle \in [0.9, 1.1]$. For the case of nearly vanishing interactions the average density was $\langle \hat{n} \rangle = 1.07$, which would lead to an expected value of local number fluctuations of $\delta n^2_{\mathrm{U=0}} = 0.495$. We measured $\delta n^2_{0.1,loose} = 0.48(2)$, which reproduced the theoretical expectation for an ideal fermi gas pretty well. For the highest interaction of U/t= 16.8 one can estimate the expected fluctuations by averaging equations 6.5 weighted with the distribution of average occupation. For the tightly filtered case one would expect local fluctuations of $\delta n^2_{U=\infty} = 0.04$, which is clearly smaller than the experimentally measured value of $\delta n^2_{U=16.8,tight} = 0.096(5)$. In addition the total fraction of doublons and holes are different. For most interactions the number of holes was larger than the number of doublons, whereas excitations should obey a particle hole symmetry. One possible explanation can be the asymmetry of tunneling and loss rates during the imaging process. We measured tunneling rates of $0.02\,\mathrm{s}^{-1}$ and loss rates of $0.038\,\mathrm{s}^{-1}$, which would enhance the number of detected holes and reduce the number of detected doublons compared to the balanced case. The process of tunneling would also explain

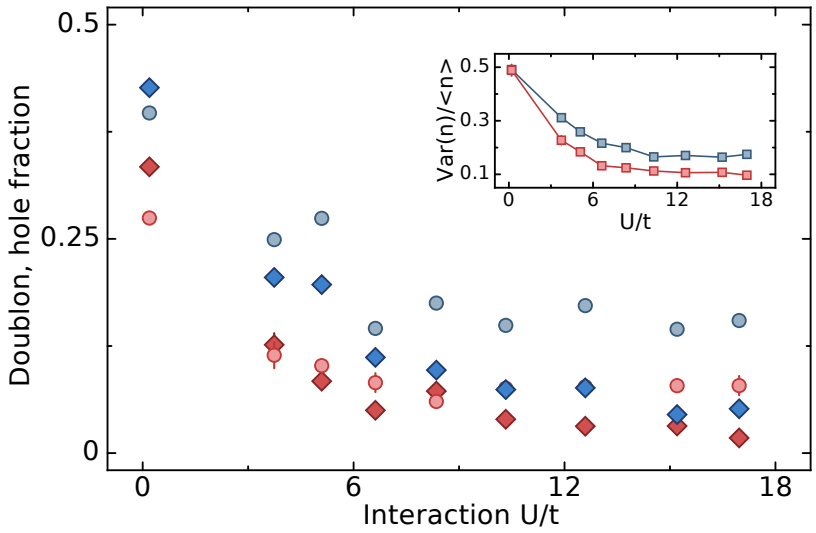

Figure 6.3: **Evolution of the density degree of freedom for different interactions U** The fraction of holes (circles) and doublons (diamonds) initially drops when increasing the interactions Ubut finally saturate. Blue (red) data points belong to the loose (tight) filter on the average occupation. Not surprisingly, the fraction of excitations is always smaller for the tighter filtered data, which chooses a closer region around average density of 1. **Inlet** Local number fluctuations are already suppressed at small interactions, due to effects of Pauli blocking in the metallic regime. When increasing the influence of the interactions onto the system, density excitations become more unlikely and finally saturate in the tight (loose) filtered case at $\delta n^2 \approx 0.1\,(0.2)$.

the overall discrepancy to the QMC results (see figure 2.5), which predicted a generally lower level of doublon excitations. The qualitative behavior of strongly reduced particle excitations when the interaction overcomes the bandwidth of the system was recovered. A more detailed view on the view on charge excitations is given in chapter 6.2.3, where the interplay of spin and charge are discussed.

6.2.2 Spin sector

In the one-dimensional Hubbard model charge and spin excitations to be separated. Measuring spin spin correlations was of great importance for two reasons. So far, only short range antiferromagnetic correlations were experimentally probed with ultracold fermions in optical lattices [56, 57]. Secondly, as theory and also our measurements point out, the charge sector freezes for temperatures which are only a fraction of the Mott gap. This has the consequence that a further decreased temperature only shows up very weakly in the number fluctuations. Instead, the entropy the system looses when reducing the temperature even further, was stored in the spin sector. When reaching the entropy (temperature) regime below $s^* \sim 1$ ($T \sim J_{\mathrm{ex}}$) already nearest-neighbor correlations increase rapidly. Measuring the correlators is therefore a perfect tool to probe the relative temperature of the system. Together with perfect knowledge of the trapping potential, even an exact quantitative thermometry of the trapped sample is possible. Since good theoretical predictions in one dimension can be delivered, also a quantitative thermometry of our samples were possible. This opens the possibility to exploit novel cooling techniques and optimize evaporation and lattice ramp performances with higher precision.

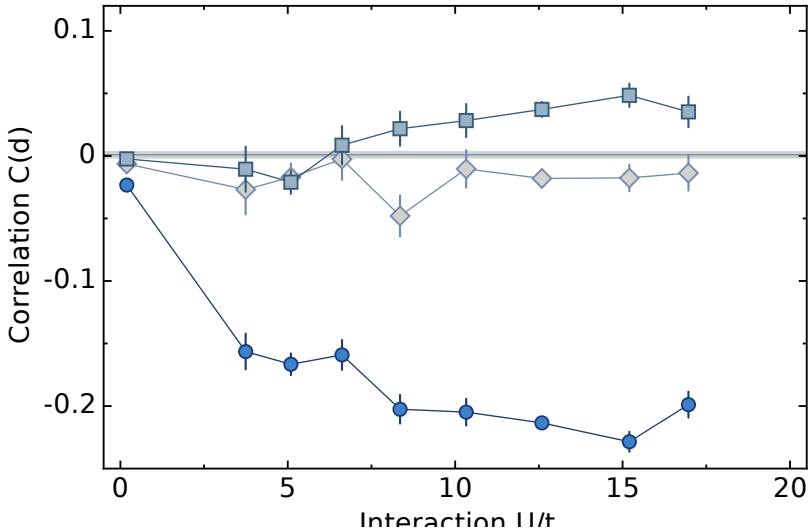

Figure 6.4: **Influence of interactions on spin correlations** Spin correlations $C(d)$ at different distances d versus interaction strength U/t. Starting from zero at vanishing interactions the finite range spin correlations develop and saturate for interaction strengths $U/t > 8$. Circled data points represent the nearest neighbor (NN) correlations ($d = 1$), quadratic- the next-nearest neighbor (NNN, $d = 2$) and diamond-shaped the next-next nearest neighbor (NNNN, $d = 3$) correlations. The connecting lines are shown as a guide to the eye. The gray line with surrounding lighter shading around zero represents vertical nearest neighbor correlations and its uncertainty ($\mathrm{NN}_y = 0.0009 \pm 0.0030$).

First, we investigated the influence of interactions on the spin sector. The dependence of the correlations on the interactions is expected to differ for isothermal and isentropic state preparation. In the former case, a maximum of the correlations is expected at intermediate interactions U/t(as shown in the phase diagram 2.1), where part of the entropy is carried by charge modes [122]. In the latter case spin correlations saturate towards strong interactions, where the energetic gap between spin and charge modes is large. In figure 6.4 the measured influence of the interaction parameter on the one-dimensional correlation functions up to the next-next-nearest neighbor (NNNN) correlator, is shown. The shown data was post-selected with the loose filter ($\langle \hat{n}_i \rangle \in [0.7, 1.3]$). The zero line of correlations was set by measuring correlations along the vertical (y-) direction. Since the one-dimensional systems were decoupled in the first step before slowly ramping up the lattice potential along the tubes, no correlations along the vertical direction should exist. We evaluated the vertical correlations as $NN_y = 0.0009 \pm 0.0030$ and present them grey shaded in the plot. Nearest neighbor (NN) correlations increase with interactions up to $U/t = 8$ and saturate for larger values within the errorbars. NNN correlations start to show up for interactions around $U/t = 8$ and further increase before they seem also to saturate for the largest interactions, the same as for correlations extending over three sites (NNNN). The measured behavior indicates towards adiabatic evolution during the lattice ramp up. To investigate this in more detail, we compared these results to QMC predictions in a homogeneous system at half-filling. Homogeneity can be assumed, since correlations were only

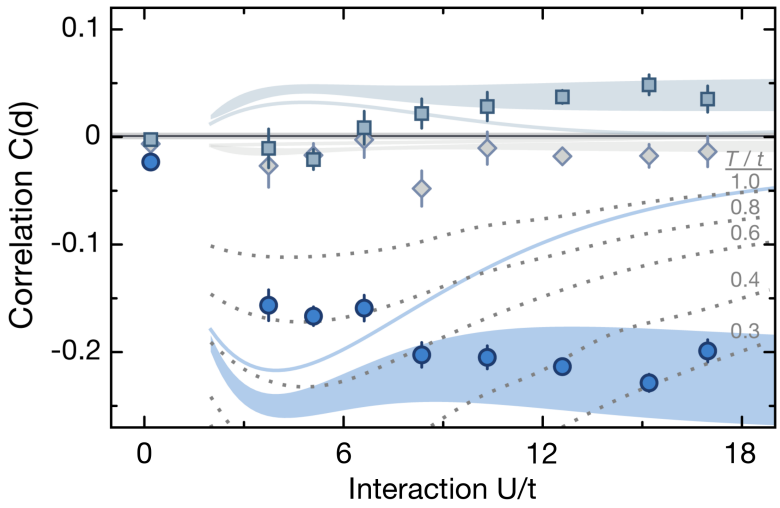

Figure 6.5: **Comparison to QMC predictions**The shaded areas indicate the QMC predictions in a homogeneous system at half-filling for an entropy per particle between $s^* = 0.60$ (lower bound) and 0.65 (upper bound); the solid line is the prediction for C(1) at $s^* = \ln(2)$. Dotted lines are isothermals for C(1) at the indicated temperatures. For large U/t, we observed adiabatic cooling, whereas both temperature and entropy decrease in the analyzed spatial region at intermediate U/t. Comparison of the data to the predictions is given in the main text.

measured up to distances of three lattice sites. The QMC predictions together with the data from 6.4 are shown in figure 6.5. Dashed lines indicate an isothermal evolution for different temperatures in the range of $T/t_x \in [0.3, 1.0]\, k_\mathrm{B}$ whereas the tunneling was fixed to the value used for all measurement $t_x = h \times 125\,\mathrm{Hz}$. One can clearly observe that the system does not develop along these isothermal lines since the temperatures of the samples is about $0.6 t_x k_\mathrm{B}$ at small interactions and decreases down to $0.3 t_x k_\mathrm{B}$ for the highest probed interactions U/t= 18. When comparing the data points with an isentropic evolution (shaded areas in figure 6.5) the measured correlations match the predictions for an entropy range of $s^* = 0.60$ to $s^* = 0.65$ for interactions ($U/t > 8$) quiet well. For these entropies the correlations show only a very weakly pronounced maximum at intermediate interactions ($U/t \approx 4$) and saturate towards high interactions. In strong contrast to this behavior, nearest neighbor correlations decay monotone when increasing the interaction for an entropy of $s^* = \ln(2)$. At intermediate interactions, $U/t \approx 6$,

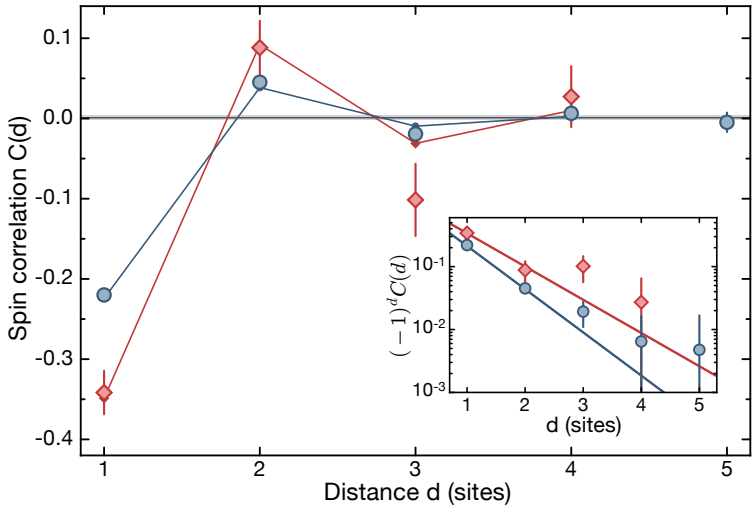

Figure 6.6: **Correlations versus distance** Measured spin correlations at $U/t = 12.6$ for the loosely (blue circles) and more tightly filtered data (red diamonds). The staggered behavior directly visualizes the antiferromagnetic nature of the correlations C(d). Correlations up to three sites are statistically significant. The vertical correlations (gray line) vanish within their 1 SEM uncertainty (light gray shading). The red and blue lines connecting filled symbols are QMC results for a homogeneous system at half-filling corresponding to entropies per particle of $s^* = 0.51(5)$ and $s^* = 0.61(1)$, respectively. **(Inlet)** Decay of the staggered spin correlator $C_s(d) = (-1)^d C(d)$ in a logarithmic plot together with an exponential fit $C_s(d) \propto \exp(-d/\zeta)$, revealing decay lengths of $\zeta = 0.69(6)$ sites and $\zeta = 1.3(4)$ sites for the two data sets. For low entropies, an exponential decay is expected to be strictly valid only at large distances. However, within the statistical uncertainty of the experimental data, the fit captures the observed behavior. All error bars represent 1 SEM.

we observed reduced spin correlations compared to the isentropic prediction at half filling. We attribute this to a changing entropy distribution in the trap [148]. This assumption is supported by a dropping number of detected excitations at the same interactions. For strong interactions of $U/t = 12.6$ we took a high statistical sample with 2000 realizations. This allows to filter the data again more tightly $\langle \hat{n}_i \rangle \in [0.9, 1.1]$ while keeping enough data points. For these two cases the measured correlations are plotted versus the distance d between lattice sites (see figure 6.6). This way of presenting the correlations visualizes the expected staggered spin order of an antiferromagnet. The lines in between the data points are again QMC predictions for half filling at entropies of $s^* = 0.51(5)$ (red line) and $s^* = 0.61(1)$ (blue line). For distances up to three lattice sites correlations are significantly distant from the zero-line, which again was set by transverse correlations and their uncertainty (grey line). Besides the NNNN correlator in the case of the tight filtered data fit the QMC predictions quite well. Since the magnitude of the measured correlator is even larger than the prediction, we can safely state down that the entropy of $s^* = 0.51(5)$ is a upper bound. The correlations of $C(1) = -0.34(9)$ we obtained in the tightly filtered tubes correspond to 58% of the zero temperature expectation in the limit of the Heisenberg model [119, 120]. For low entropies, an exponential decay of the magnitude of correlations $C_s(d) \propto exp(-d/\zeta)$ is expected to be strictly valid only at large distances. However, when plotting the logarithm of the demodulated correlations $C_s(d) = (-1)^d C(d)$ versus the distance, a linear fit captures the behavior quite well within the errorbars, as shown in the inlet. The extracted correlation lengths are $\zeta_{s=0.51} = 1.3(4)$ and $\zeta_{s=0.61} = 0.69(6)$ sites respectively. We can also use these entropies to translate them to other energy scales in the system. If one assumes a uniform system at half filling the entropy of $s = 0.51(5)k_\mathrm{B}$ corresponds to a temperature of $k_\mathrm{B}T/t_x = 0.22(4)$. For the given interaction the superexchange coupling is $J_{\mathrm{ex},U=12.6t} \approx 0.32$. This means the temperature in these one-dimensional tubes was as low as two thirds of the exchange. In absolute numbers the temperature is nearly as low as one nano-Kelvin $T = 1.32(5)$ nK. To stress the possibility of using the measured correlations as a thermometric tool even more QMC results of the NN and NNN correlator for different entropies and a fixed interaction value of $U/t = 10$ is compared to the measured correlations at $U/t = 10.3$. As shown in figure 6.7 read out of the correlations is perfectly tailored to optimize cooling of the systems for entropies below $s^* = 1k_\mathrm{B}$ [101, 149].

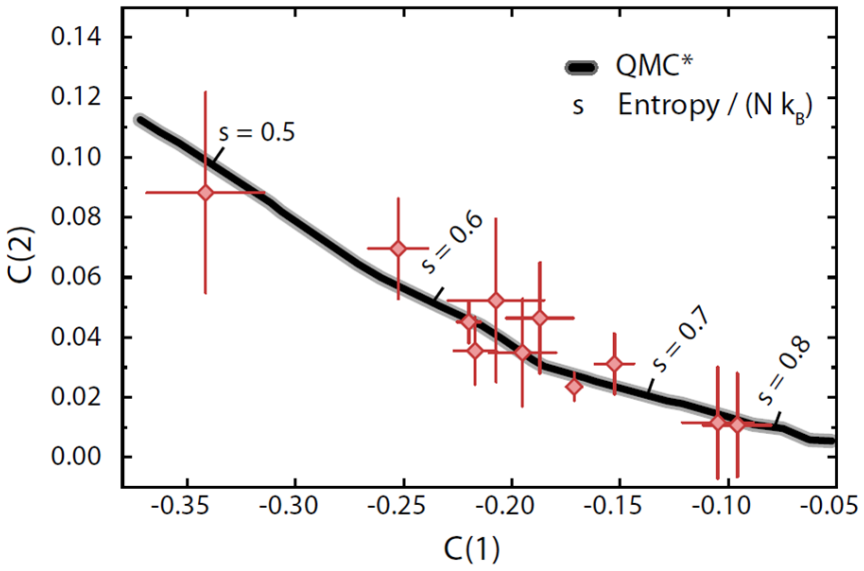

Figure 6.7: **Using correlations as a thermometric tool** Combining the measured nearest neighbor C(1) and next nearest neighbor correlator C(2) can be used as a thermometric tool. The data points (red) for U/t= 10.3 fit well to QMC predictions for U/t=10 (black line, with grey shading presenting the error of the prediction) for an uniform one-dimensional system at different entropies per particle within the errorbars (1 SEM).

6.2.3 Interplay of spin and charge

All presented data in this chapter so far, have been filtered on their average density. All experimental results regarding spin correlations were compared to half filled systems. To obtain more insight into the behavior of the spin correlations when adding excitations to the system, we make use of our full microscopic characterization of the system. As described in the theory chapter, we expect for one-dimensional systems, charge and spin excitations to propagate independent, based on spin-charge separation [88]. To study the antiferromagnetic spin correlations away from half filling, we show the nearest neighbor correlator $C(1)$ per pair of sites versus their mean density in figure 6.8. This data combines different datasets taken at $U/t = 10.3$ and

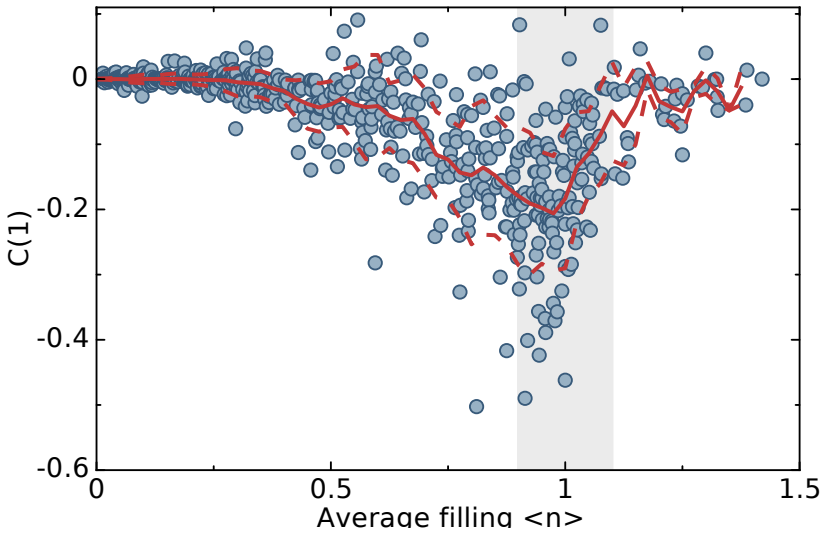

Figure 6.8: **Nearest neighbor correlations for different average filling** We show the nearest-neighbor spin correlations C(1) for different densities corresponding to different positions in the trap. The data combine several measurements at an interaction strength of $U/t = 10.3$, also including higher-temperature data. Every data point corresponds to two neighboring sites, where between 30 and 2000 samples contribute. The red solid curves indicates the mean correlation at the given density. The red dashed lines illustrate the mean plus/minus the standard deviation. The strength of spin correlations C(1) peaks just below densities of one ($\langle \hat{n} \rangle = 0.96$) is consistent with the half-filling regime taking the detection efficiency of $\sim 95\%$ into account. Inside the grey shaded ($\langle \hat{n}_i \rangle = 1 \pm 0.1$) one observes strong vertical scattering of the nearest neighbor correlations. We expect this to be linked to the large spread of density fluctuations hidden in the same average filling. Errorbars are omitted for reasons of clarity of the presentation.

also contains measurements at different temperatures, obtained by holding the cloud for up to $2.5\,\mathrm{s}$ in the vertical lattice plane before transferring them into the one-dimensional lattice tubes. We observe a clear dependence of the spin correlator on the local density, with strongest correla-

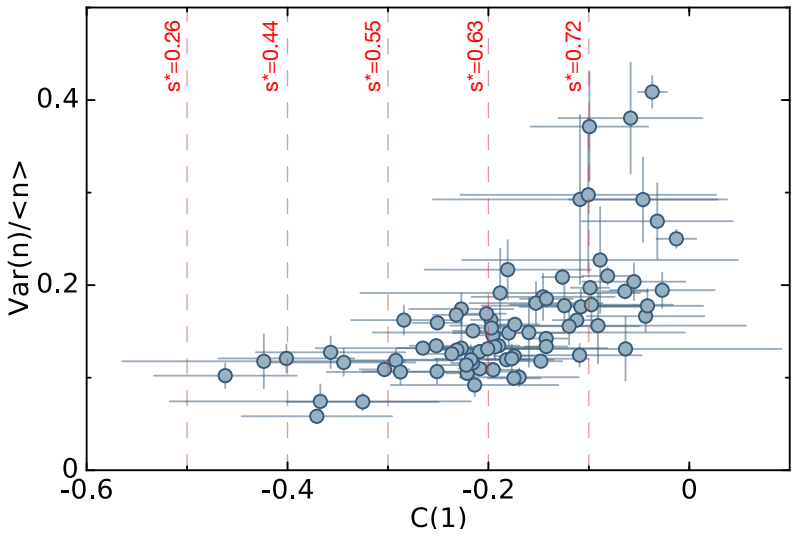

Figure 6.9: **Particle number fluctuations versus correlations** For average fillings of $\langle \hat{n}_i \rangle = 1 \pm 0.1$ and interactions of U/t=10.3 we analyzed the dependence of number fluctuations on the nearest neighbor correlations. Again, QMC results were used to convert NN correlation into entropies (red, vertical dashed lines). At the onset of nearest neighbor correlations also number fluctuations decrease, whereas decreasing the entropy below ln(2) does not show up strongly in reduced particle number fluctuations anymore. The charge sector is frozen, entropy is carried by spin excitation modes.

tions close to an average filling of 1. On average the highest correlations were found at densities of $\langle \hat{n} \rangle = 0.96$. When taking the finite detection efficiency (tunneling and losses) into account this agrees quiet well with the regime of half filling. The spread of the correlations increases and is the highest for nearly half filling. We assign this large vertical spread to different density fluctuations, which represent different entropy regimes. To investigate this in more detail, we selected the area of densities $\langle \hat{n}_i \rangle = 1 \pm 0.1$ and probe the effect of number fluctuations on the correlations, shown in figure 6.9. The large spread of NN correlations in the investigated area can only partly be explained via different number fluctuations. Whereas at the onset of antiferromagnetic correlations $0 > C(1) > -0.15$ the number fluctuations strongly decrease, further increased spin correlations seem not be linked to number fluctuations anymore. The charge sector is frozen. We used the obtained correlations to extract entropies from QMC predictions at half filling, indicated with red dashed vertical lines. Lowering the entropy shows no effect on the particle number fluctuations below $s^* \approx 0.6$. When the system is further cooled, the extracted entropy was stored in excitations of the spin sector. As pointed out in the theory section in one-dimensional systems spin and density excitations are expected to propagate independently. In figure 6.8 the effect of doping the system weakens the nearest neighbor correlations. This is not surprising, since a hole excitation next to an atom contributes zero to the nearest neighbor corre-

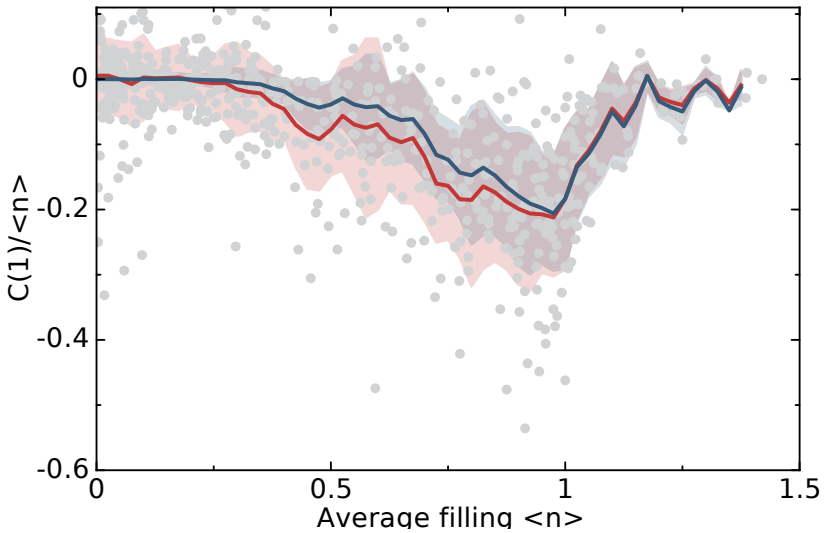

Figure 6.10: **Normalized spin correlations** When normalizing the correlations to the average density of the realization (grey data points) also very strong NN correlation events at very small average densities occur. Quantitatively the standard deviation of the normalized correlations (red shaded) is always larger compared to the case of normalizing to $\langle \hat{n} \rangle = 1$ (blue shaded).

lator. When we normalize the nearest-neighbor correlations to the probability of finding a hole (inverse average density) (figure 6.10). Obviously the normalization brings up events of large NN correlations even for very small densities. This might be already an indication that there are low entropy samples carrying density excitations which only split the antiferromagnetic chains into antiferromagnetic domain walls. When analyzing the next-nearest neighbor correlations versus the average filling, this indication can be supported (figure 6.11). The correlations peak again at nearly the same average density as the nearest neighbor correlators. More interesting seems the area of average fillings of $0.3 < \langle \hat{n}_i \rangle < 0.7$. A large amount of realizations show negative NNN correlations, which corresponds to the case of opposite spins with one lattice site in between. If there is a hole located in between the two atoms, this would support the expected behavior of a hole in one dimension. The hole moves freely and cuts the spin chain remains antiferromagnetically ordered on the subset of singly occupied sites.

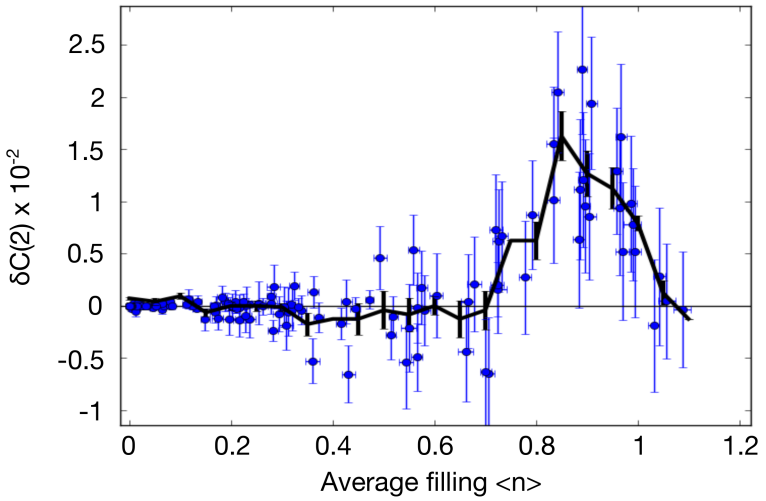

Figure 6.11: **NNN correlations at different fillings** The correlations (blue datapoints) peak again at nearly the same average density as the nearest neighbor correlators (figure 6.10), as indicated by the running average (black line). However, for average fillings of $0.3 < \langle \hat{n}_i \rangle < 0.7$ a remarkable amount of datapoints indicate negative NNN-correlations. This might indicate configurations where an excitation just breaks the antiferromagnetic order into domain walls, whereas inside themselves the spin-order remains.

Chapter 7

Conclusion and outlook

In the framework of this thesis a spin and density resolving quantum gas microscope for fermionic lithium atoms was realized. We realized a spin resolution by spatially separating opposite spin states before fluorescence imaging with a fidelity of 98%. Our technique enabled us to investigate the full density and spin statistics of a strongly correlated many body systems with tunable interactions.Low entropy samples of $^6\mathrm{Li}$ were trapped in optical superlattice potentials, mimicking strongly correlated one-dimensional Hubbard systems. We experimentally observed antiferromagnetic correlations in Hubbard chains extending up to three lattice sites. By comparing the obtained results to QMC predictions, we could state the lowest entropies to $s = 0.51(4)\,k_\mathrm{B}$. Qualitatively it could be revealed that density and spin excitations in one-dimensional systems are independent. To make a quantitative statement about the interplay of spin and charge degrees of freedom larger sets of data and different experimental situations need to be probed. The use of spin correlations as a relative '*spin thermometer*' opens the route to benchmark novel cooling techniques, which are required to investigate the entropy regime being under debate to support d-wave superconductivity [93, 101].

Technical developments

Technically, the experimental setup was further improved compared to the status presented in [83]. In detail, the production of two-dimensional Fermi gases was simplified by direct loading of a single plane of the vertical lattice, getting rid of the process of radio-frequency slicing in a magnetic field gradient. Furthermore, the resolution of the high-resolution imaging was improved, leading to a smaller size of the accumulated point-spread function. This allowed to shorten the imaging durations to $600\,\mathrm{ms}$, which reduces the small, but finite, amount of tunneling processes and losses during the fluorescence imaging. In addition, fluctuations of the relative superlattice phase were improved from $\varphi_\mathrm{rel} \approx 300\,\mathrm{mrad}$ down to $\varphi_\mathrm{rel} \approx 30\,\mathrm{mrad}$, by shielding the setup as much as possible from all sources of airflow and ambient noise. This allowed for a fidelity of the spin-splitting process of 98% and opened the route towards the deterministic preparation of spin-singlets in a dimerized lattice potential [150].

Current developments

During the writing of this thesis one dimensional systems were taken and two dimensional samples were experimentally investigated. All current approaches in our experimental setup investigate the origin of quantum magnetism. Our highly flexible setup, including superlattices along all directions of space, enables us to enter this strongly correlated regime in more than one dimension, but still persisting the possibility to use the presented spin-resolution technique.

- One approach used lattice configurations which allowed for two dimensional spin correlations. These spin-spin correlations have been experimentally already shown in [138] for NN and [142] for longer ranged correlations up to three lattice sites. We could show correlations which reached up to two lattice sites, mainly limited by a non-perfect lattice potential, where strong local defects shape the filling, which induce regions of high entropy in region of interest. Flattening the lattice potentials by improving the lattice beam quality or actively correcting for defects by using a digital mirror device [65].

- Therefore current approaches focused on one-dimensional systems. The link of dimerized singlets, so called valence bonds, to longer-ranged antiferromagnets, as pointed out by Affleck et. al [151] is of central interest in quantum magnetism. The dimerized configuration is produced by initially loading a low entropy double band insulating state into the large-scale large-scale configuration of our optical superlattice, only allowing for tunneling along the x-direction. After turning on repulsive interactions, the doublons were adiabatically split into two short-scale lattice sites in the fashion of our spin-splitting process 5.11, but with absent magnetic field. This process leads to decoupled one-dimensional valence bonds with high probability of half filling per spin component. It was found, that a sufficient slow connection of these dimers could reveal NN correlations to a high degree and even NNN correlations were build. This approach is also highly connected to a more detailed study of the interplay between spin and charge, which was qualitatively mentioned in this thesis. The stability of the machine was even further improved which allowed to take huge statistical datasets. These are required, since in our samples hole excitations within the regions of lowest entropy are very rare. My colleagues could observe that the probability to find opposite spins on two lattice sites which are separated by an empty site is enhanced, as it would be expected in one-dimensional systems due to spin-charge separation.

Future developments and experiments

Technically, a few weak points of the experimental setup are still present. Even though the depth of the Pinning lattices is immense, losses and tunneling events during the imaging sequence remain finite. This is mainly limited by a spatially non-stable Pinning lattice potential, caused by pointing-instabilities of the fiber-amplifier. Their replacement with more stable lasers as well as an improved optical setup, handling the peculiarities of high-power laser setups, will

solve this issue. Another remaining challenge is the production of lattice potentials which are free of defects. The lower the entropies of the investigated samples are, the more important this issue gets. It will be of central interest to improve the lattice potentials themselves and have the possibility to correct for smallest imperfections with a Digital Mirror Device (DMD). The latter will also provide the possibility to address a single site or an arbitrary pattern of the lattice potential. This has been realized already in bosonic quantum gas microscopes and triggered a tremendous amount of experimental results [67, 152, 153]. One possible experimental scheme could directly unfold the nature of spin and charge separation in one dimension and show the expected change when allowing for two dimensional couplings. Such an experiment would probe the dynamics of two holes, each produced in another one-dimensional chain and observe their dynamics when allowing for coupling of the two one-dimensional chains [88].

Appendix- QMC simulations

To understand the basic method and give the precise parameter range of the QMC simulations, the subsection from the supplementary information of our publication [82] will be given in the following section. The numerics were done and kindly provided by Lode Pollet and Jacopo Nespolo. The numerical results of the QMC simulations build on the mapping between the one-dimensional fermionic Hubbard model and a system of two hard-core bosonic species with on-site interspecies interactions [154]. Path integral Monte Carlo simulations with worm-type updates [155], here employed in the implementation of reference [156], have a linear scaling in the system volume when simulating the resulting bosonic model. The method overcomes critical slowing down for systems near a phase transition, and also allows to treat the trap efficiently. The charge C_c (atomic density) and spin density wave C_s are both diagonal observables with respect to the Fock basis $\{|..., n_j, ...\rangle\}$ used in the algorithm, and can readily be computed as

$$C_{c(s)}(i,j) = \frac{1}{4}\langle\left(n_{\uparrow}^{i} \pm n_{\downarrow}^{i}\right)\left(n_{\uparrow}^{j} \pm n_{\downarrow}^{j}\right)\rangle$$

Here, the arrows distinguish between the two species of hard-core bosons, the upper (lower) sign refers to the charge c (spin s) density wave, and i and j are site indices. All the homogeneous simulations were carried out in the grand-canonical ensemble on chains of size $\mathrm{L} = 20$, which was checked to be already large enough to rule out finite size corrections for the (local) quantities and the parameters regimes we are interested in. In the experiment, the atom number as well as the total magnetization in each tube fluctuates from shot to shot justifying the use of the grand-canonical approach. Note that in the canonical ensemble some quantities, for example, the nearest-neighbor spin-spin correlator, show very strong finite size effects at half filling and large values of U/t. For the system sizes and temperatures of interest here, the values can differ up to 50% from the grand-canonical values, the latter being much closer to the thermodynamic limit. The computation of the entropy per particle $s = S/Nk_{\mathrm{B}}$ is usually more cumbersome in Monte Carlo simulations. At infinite temperature it is $s(\beta = 0) = 2\ln(2)$, while at zero temperature $s(\beta = \infty) = 0$. All energies are measured in units of the hopping t and the inverse temperature $\beta = 1/k_{\mathrm{B}}T$. For intermediate temperatures, the entropy is obtained by numerical integration of the thermodynamic relation

$$S(\beta) = S(\beta_{\mathrm{ref}}) + \int_{\beta_{\mathrm{ref}}}^{\beta} \beta' \frac{dE}{d\beta'} d\beta'$$

where β_{ref} is a reference inverse temperature for which $s(\beta_{\text{ref}})$ is known. The total energy $E(\beta)$ is obtained from the Monte Carlo simulations and interpolated using a cubic spline, which reduces the error. The standard choice was $\beta_{\text{ref}} = 0$, but we crosschecked the results by using high temperature series expansion methods [157] for $\beta < 0.1$ and by repeating the integration procedure starting from $\beta_{\text{ref}} = \infty$, ,finding very good agreement between the different methods. The error on s is dominated by the uncertainty on $E(\beta)$, and was quantified by bootstrapping the Monte Carlo energy samples and the integration procedure. Simulations of the trapped system were carried out with a harmonic confining potential $V(r) = vr^2$ coupled to the particle density, effectively modifying the local effective chemical potential, $\epsilon(r) = \mu - V(r)$. We set the trap so that $V = 0$ at the central site of each chain and kept the trapping amplitude fixed to $v = 0.05$. The total entropy was computed in the same way as described for the homogeneous case but with $\beta_{\text{ref}} = 0.01$. This temperature is still sufficiently high that the use of the high temperature series in combination with the local density approximation remains justified to obtain the reference entropy. Similarly to the experimental conditions, the measurements of local observables were restricted to the sites at the bottom of the trap (sites $i = -5, ..., s5$ with respect to the center of the trap), where we verified that the average filling is close to one for large U/t. Furthermore, we adjusted the chemical potential for each interaction strength U/t to keep the total number of particles in the trap approximately constant ($N \approx 22$ for $\beta > 2$ corresponding to $s_t < 0.9$).This results in the central region of the trap being slightly doped towards higher densities for low U/t.

Bibliography

[1] J. G. Bednorz and K. A. Müller, "Possible high tc superconductivity in the ba la cu o system," in *Ten Years of Superconductivity: 1980–1990*, pp. 267–271, Springer, 1986.

[2] L. Landau, "The theory of a fermi liquid," *Soviet Physics Jetp-Ussr*, vol. 3, no. 6, pp. 920–925, 1957.

[3] D. Pines and P. Nozières, *The Theory of Quantum Liquids: Normal Fermi Liquids*, vol. 1. WA Benjamin, 1966.

[4] E. Dagotto, "Correlated electrons in high-temperature superconductors," *Reviews of Modern Physics*, vol. 66, no. 3, p. 763, 1994.

[5] K. Chao, J. Spałek, and A. Oleś, "Canonical perturbation expansion of the hubbard model," *Physical Review B*, vol. 18, no. 7, p. 3453, 1978.

[6] P. W. Anderson, "Localized magnetic states in metals," *Physical Review Letters*, vol. 124, no. 1, p. 41, 1961.

[7] J. Hubbard, "Electron Correlations in Narrow Energy Bands," *Proceedings of the Royal Society of London A: Mathematical, Physical and Engineering Sciences*, vol. 276, pp. 238–257, Nov. 1963.

[8] N. Mott, "Metal-insulator transition," *Reviews of Modern Physics*, vol. 40, no. 4, p. 677, 1968.

[9] A. Montorosi, *The Hubbard Model*. Singapore: World Scientific, 1992.

[10] R. P. Feynman, "Simulating physics with computers," *International journal of theoretical physics*, vol. 21, no. 6, pp. 467–488, 1982.

[11] D. Jaksch, C. Bruder, J. I. Cirac, C. W. Gardiner, and P. Zoller, "Cold bosonic atoms in optical lattices," *Physical Review Letters*, vol. 81, no. 15, p. 3108, 1998.

[12] I. Bloch, J. Dalibard, and S. Nascimbène, "Quantum simulations with ultracold quantum gases," *Nature Physics*, vol. 8, pp. 267–276, Apr. 2012.

[13] M. Lewenstein, A. Sanpera, V. Ahufinger, B. Damski, A. Sen, and U. Sen, "Ultracold atomic gases in optical lattices: mimicking condensed matter physics and beyond," *Advances in Physics*, vol. 56, no. 2, pp. 243–379, 2007.

[14] K. B. Davis, M.-O. Mewes, M. R. Andrews, N. Van Druten, D. Durfee, D. Kurn, and W. Ketterle, "Bose-einstein condensation in a gas of sodium atoms," *Physical review letters*, vol. 75, no. 22, p. 3969, 1995.

[15] M. Anderson, J. Ensher, M. Matthews, C. Wieman, and E. Cornell, "Bose-einstein condensation in a dilute atomic vapor," *science*, vol. 269, p. 14, 1995.

[16] C. C. Bradley, C. Sackett, J. Tollett, and R. G. Hulet, "Evidence of bose-einstein condensation in an atomic gas with attractive interactions," *Physical Review Letters*, vol. 75, no. 9, p. 1687, 1995.

[17] M. Greiner, O. Mandel, T. W. Hänsch, and I. Bloch, "Collapse and revival of the matter wave field of a Bose–Einstein condensate," *Nature*, vol. 419, pp. 51–54, Oct. 2002.

[18] M. Girardeau, "Relationship between systems of impenetrable bosons and fermions in one dimension," *Journal of Mathematical Physics*, vol. 1, no. 6, pp. 516–523, 1960.

[19] B. Paredes, A. Widera, V. Murg, O. Mandel, S. Fölling, I. Cirac, G. V. Shlyapnikov, T. W. Hänsch, and I. Bloch, "Tonks–Girardeau gas of ultracold atoms in an optical lattice," *Nature*, vol. 429, pp. 277–281, May 2004.

[20] T. Kinoshita, T. Wenger, and D. S. Weiss, "Observation of a one-dimensional tonks-girardeau gas," *Science*, vol. 305, no. 5687, pp. 1125–1128, 2004.

[21] H. Feshbach, "Unified theory of nuclear reactions," *Annals of Physics*, vol. 5, no. 4, pp. 357–390, 1958.

[22] C. Chin, R. Grimm, P. Julienne, and E. Tiesinga, "Feshbach resonances in ultracold gases," *Reviews of Modern Physics*, vol. 82, no. 2, p. 1225, 2010.

[23] K. Aikawa, A. Frisch, M. Mark, S. Baier, A. Rietzler, R. Grimm, and F. Ferlaino, "Bose-einstein condensation of erbium," *Physical review letters*, vol. 108, no. 21, p. 210401, 2012.

[24] A. Griesmaier, J. Werner, S. Hensler, J. Stuhler, and T. Pfau, "Bose-einstein condensation of chromium," *Physical Review Letters*, vol. 94, no. 16, p. 160401, 2005.

[25] M. Lu, N. Q. Burdick, S. H. Youn, and B. L. Lev, "Strongly dipolar bose-einstein condensate of dysprosium," *Physical review letters*, vol. 107, no. 19, p. 190401, 2011.

[26] R. Heidemann, U. Raitzsch, V. Bendkowsky, B. Butscher, R. Löw, L. Santos, and T. Pfau, "Evidence for coherent collective rydberg excitation in the strong blockade regime," *Physical Review Letters*, vol. 99, no. 16, p. 163601, 2007.

[27] P. Schauß, M. Cheneau, M. Endres, T. Fukuhara, S. Hild, A. Omran, T. Pohl, C. Gross, S. Kuhr, and I. Bloch, "Observation of spatially ordered structures in a two-dimensional Rydberg gas," *Nature*, vol. 491, no. 7422, p. 87, 2012.

[28] J. Zeiher, R. van Bijnen, P. Schauß, S. Hild, J.-y. Choi, T. Pohl, I. Bloch, and C. Gross, "Many-body interferometry of a Rydberg-dressed spin lattice," *Nature Physics 12, 1095–1099*, Feb. 2016.

[29] K.-K. Ni, S. Ospelkaus, M. De Miranda, A. Pe'er, B. Neyenhuis, J. Zirbel, S. Kotochigova, P. Julienne, D. Jin, and J. Ye, "A high phase-space-density gas of polar molecules," *science*, vol. 322, no. 5899, pp. 231–235, 2008.

[30] A. Chotia, B. Neyenhuis, S. A. Moses, B. Yan, J. P. Covey, M. Foss-Feig, A. M. Rey, D. S. Jin, and J. Ye, "Long-lived dipolar molecules and feshbach molecules in a 3d optical lattice," *Physical review letters*, vol. 108, no. 8, p. 080405, 2012.

[31] S. A. Moses, J. P. Covey, M. T. Miecnikowski, B. Yan, B. Gadway, J. Ye, and D. S. Jin, "Creation of a low-entropy quantum gas of polar molecules in an optical lattice," *Science*, vol. 350, no. 6261, pp. 659–662, 2015.

[32] J. W. Park, S. A. Will, and M. W. Zwierlein, "Ultracold dipolar gas of fermionic na 23 k 40 molecules in their absolute ground state," *Physical review letters*, vol. 114, no. 20, p. 205302, 2015.

[33] J. M. Kosterlitz and D. J. Thouless, "Ordering, metastability and phase transitions in two-dimensional systems," *Journal of Physics C: Solid State Physics*, vol. 6, no. 7, p. 1181, 1973.

[34] V. Berezinskii, "Destruction of long-range order in one-dimensional and two-dimensional systems having a continuous symmetry group i. classical systems," *Soviet Journal of Experimental and Theoretical Physics*, vol. 32, p. 493, 1971.

[35] Z. Hadzibabic, P. Krüger, M. Cheneau, B. Battelier, and J. Dalibard, "Berezinskii–kosterlitz–thouless crossover in a trapped atomic gas," *Nature*, vol. 441, no. 7097, pp. 1118–1121, 2006.

[36] P. Soltan-Panahi, J. Struck, P. Hauke, A. Bick, W. Plenkers, G. Meineke, C. Becker, P. Windpassinger, M. Lewenstein, and K. Sengstock, "Multi-component quantum gases in spin-dependent hexagonal lattices," *Nature Physics*, vol. 7, no. 5, pp. 434–440, 2011.

[37] J. Struck, C. Ölschläger, R. Le Targat, P. Soltan-Panahi, A. Eckardt, M. Lewenstein, P. Windpassinger, and K. Sengstock, "Quantum simulation of frustrated classical magnetism in triangular optical lattices," *Science*, vol. 333, no. 6045, pp. 996–999, 2011.

[38] J. Sebby-Strabley, M. Anderlini, P. Jessen, and J. Porto, "Lattice of double wells for manipulating pairs of cold atoms," *Physical Review A*, vol. 73, p. 033605, Mar. 2006.

[39] S. Trotzky, P. Cheinet, S. Folling, M. Feld, U. Schnorrberger, A. M. Rey, A. Polkovnikov, E. A. Demler, M. D. Lukin, and I. Bloch, "Time-Resolved Observation and Control of Superexchange Interactions with Ultracold Atoms in Optical Lattices," *Science*, vol. 319, pp. 295–299, Jan. 2008.

[40] T. Uehlinger, G. Jotzu, M. Messer, D. Greif, W. Hofstetter, U. Bissbort, and T. Esslinger, "Artificial graphene with tunable interactions," *Physical review letters*, vol. 111, no. 18, p. 185307, 2013.

[41] Y.-J. Lin, K. Jiménez-García, and I. Spielman, "Spin-orbit-coupled bose-einstein condensates," *Nature*, vol. 471, no. 7336, pp. 83–86, 2011.

[42] L. Duca, T. Li, M. Reitter, I. Bloch, M. Schleier-Smith, and U. Schneider, "An Aharonov-Bohm interferometer for determining Bloch band topology," *Science*, vol. 347, pp. 288–292, Jan. 2015.

[43] L. Tarruell, D. Greif, T. Uehlinger, G. Jotzu, and T. Esslinger, "Creating, moving and merging dirac points with a fermi gas in a tunable honeycomb lattice," *Nature*, vol. 483, no. 7389, pp. 302–305, 2012.

[44] M. Atala, M. Aidelsburger, J. T. Barreiro, D. Abanin, T. Kitagawa, E. Demler, and I. Bloch, "Direct measurement of the Zak phase in topological Bloch bands," *Nature Physics*, vol. 9, no. 12, pp. 795–800, 2013.

[45] M. Atala, M. Aidelsburger, M. Lohse, J. T. Barreiro, B. Paredes, and I. Bloch, "Observation of chiral currents with ultracold atoms in bosonic ladders," *Nature Physics*, vol. 10, pp. 588–593, July 2014.

[46] M. Aidelsburger, M. Lohse, C. Schweizer, M. Atala, J. T. Barreiro, S. Nascimbène, N. R. Cooper, I. Bloch, and N. Goldman, "Measuring the Chern number of Hofstadter bands with ultracold bosonic atoms," *Nature Physics*, vol. 11, pp. 162–166, Feb. 2015.

[47] M. Lohse, C. Schweizer, O. Zilberberg, M. Aidelsburger, and I. Bloch, "A thouless quantum pump with ultracold bosonic atoms in an optical superlattice," *Nature Physics*, vol. 12, pp. 350–354, Apr. 2016.

[48] B. DeMarco and D. S. Jin, "Onset of fermi degeneracy in a trapped atomic gas," *Science*, vol. 285, no. 5434, pp. 1703–1706, 1999.

[49] R. A. Ogg, "Bose-einstein condensation of trapped electron pairs. phase separation and superconductivity of metal-ammonia solutions," *Phys. Rev.*, vol. 69, pp. 243–244, Mar 1946.

[50] J. Bardeen, L. N. Cooper, and J. R. Schrieffer, "Theory of superconductivity," *Physical Review*, vol. 108, no. 5, p. 1175, 1957.

[51] C. Regal, M. Greiner, and D. S. Jin, "Observation of resonance condensation of fermionic atom pairs," *Physical Review Letters*, vol. 92, no. 4, p. 040403, 2004.

[52] T. Bourdel, L. Khaykovich, J. Cubizolles, J. Zhang, F. Chevy, M. Teichmann, L. Tarruell, S. Kokkelmans, and C. Salomon, "Experimental study of the bec-bcs crossover region in lithium 6," *Physical Review Letters*, vol. 93, no. 5, p. 050401, 2004.

[53] M. Bartenstein, A. Altmeyer, S. Riedl, S. Jochim, C. Chin, J. H. Denschlag, and R. Grimm, "Collective excitations of a degenerate gas at the bec-bcs crossover," *Physical review letters*, vol. 92, no. 20, p. 203201, 2004.

[54] U. Schneider, L. Hackermuller, S. Will, T. Best, I. Bloch, T. A. Costi, R. W. Helmes, D. Rasch, and A. Rosch, "Metallic and Insulating Phases of Repulsively Interacting Fermions in a 3d Optical Lattice," *Science*, vol. 322, pp. 1520–1525, Dec. 2008.

[55] R. Jördens, N. Strohmaier, K. Günter, H. Moritz, and T. Esslinger, "A Mott insulator of fermionic atoms in an optical lattice," *Nature*, vol. 455, pp. 204–207, Oct. 2008.

[56] R. A. Hart, P. M. Duarte, T.-L. Yang, X. Liu, T. Paiva, E. Khatami, R. T. Scalettar, N. Trivedi, D. A. Huse, and R. G. Hulet, "Observation of antiferromagnetic correlations in the Hubbard model with ultracold atoms," *Nature*, vol. 519, pp. 211–214, Mar. 2015.

[57] D. Greif, T. Uehlinger, G. Jotzu, L. Tarruell, and T. Esslinger, "Short-Range Quantum Magnetism of Ultracold Fermions in an Optical Lattice," *Science*, vol. 340, pp. 1307–1310, May 2013.

[58] S. Trotzky, Y.-A. Chen, U. Schnorrberger, P. Cheinet, and I. Bloch, "Controlling and Detecting Spin Correlations of Ultracold Atoms in Optical Lattices," *Physical Review Letters*, vol. 105, p. 265303, Dec. 2010.

[59] R. Brown, "Xxvii. a brief account of microscopical observations made in the months of june, july and august 1827, on the particles contained in the pollen of plants; and on the general existence of active molecules in organic and inorganic bodies," *Philosophical Magazine Series 2*, vol. 4, no. 21, pp. 161–173, 1828.

[60] C. Eggeling, C. Ringemann, R. Medda, G. Schwarzmann, K. Sandhoff, S. Polyakova, V. N. Belov, B. Hein, C. von Middendorff, A. Schönle, *et al.*, "Direct observation of the nanoscale dynamics of membrane lipids in a living cell," *Nature*, vol. 457, no. 7233, pp. 1159–1162, 2009.

[61] G. Kucsko, P. Maurer, N. Y. Yao, M. Kubo, H. Noh, P. Lo, H. Park, and M. D. Lukin, "Nanometre-scale thermometry in a living cell," *Nature*, vol. 500, no. 7460, pp. 54–58, 2013.

[62] W. Neuhauser, M. Hohenstatt, P. Toschek, and H. Dehmelt, "Localized visible ba+ mono-ion oscillator," *Physical Review A*, vol. 22, no. 3, p. 1137, 1980.

[63] N. Schlosser, G. Reymond, I. Protsenko, and P. Grangier, "Sub-poissonian loading of single atoms in a microscopic dipole trap," *Nature*, vol. 411, no. 6841, pp. 1024–1027, 2001.

[64] K. D. Nelson, X. Li, and D. S. Weiss, "Imaging single atoms in a three-dimensional array," *Nature Physics*, vol. 3, no. 8, pp. 556–560, 2007.

[65] W. S. Bakr, J. I. Gillen, A. Peng, S. Fölling, and M. Greiner, "A quantum gas microscope for detecting single atoms in a hubbard-regime optical lattice," *Nature*, vol. 462, no. 7269, pp. 74–77, 2009.

[66] J. F. Sherson, C. Weitenberg, M. Endres, M. Cheneau, I. Bloch, and S. Kuhr, "Single-atom-resolved fluorescence imaging of an atomic Mott insulator," *Nature*, vol. 467, pp. 68–72, Aug. 2010.

[67] C. Weitenberg, M. Endres, J. F. Sherson, M. Cheneau, P. Schauß, T. Fukuhara, I. Bloch, and S. Kuhr, "Single-spin addressing in an atomic Mott insulator," *Nature*, vol. 471, pp. 319–324, Mar. 2011.

[68] M. Cheneau, P. Barmettler, D. Poletti, M. Endres, P. Schauß, T. Fukuhara, C. Gross, I. Bloch, C. Kollath, and S. Kuhr, "Light-cone-like spreading of correlations in a quantum many-body system," *Nature*, vol. 481, p. 484, Jan. 2012.

[69] S. Hild, T. Fukuhara, P. Schauß, J. Zeiher, M. Knap, E. Demler, I. Bloch, and C. Gross, "Far-from-Equilibrium Spin Transport in Heisenberg Quantum Magnets," *Physical Review Letters*, vol. 113, p. 147205, 2014.

[70] J. Simon, W. S. Bakr, R. Ma, M. E. Tai, P. M. Preiss, and M. Greiner, "Quantum simulation of antiferromagnetic spin chains in an optical lattice," *Nature*, vol. 472, no. 7343, pp. 307–312, 2011.

[71] M. Endres, M. Cheneau, T. Fukuhara, C. Weitenberg, P. Schauß, C. Gross, L. Mazza, M. C. Bañuls, L. Pollet, I. Bloch, and S. Kuhr, "Observation of Correlated Particle-Hole Pairs and String Order in Low-Dimensional Mott Insulators," *Science*, vol. 334, no. 6053, p. 200, 2011.

[72] T. Fukuhara, S. Hild, J. Zeiher, P. Schauß, I. Bloch, M. Endres, and C. Gross, "Spatially Resolved Detection of a Spin-Entanglement Wave in a Bose-Hubbard Chain," *Physical Review Letters*, vol. 115, p. 035302, July 2015.

[73] R. Islam, R. Ma, P. M. Preiss, M. E. Tai, A. Lukin, M. Rispoli, and M. Greiner, "Measuring entanglement entropy in a quantum many-body system," *Nature*, vol. 528, no. 7580, pp. 77–83, 2015.

[74] E. Haller, J. Hudson, A. Kelly, D. A. Cotta, B. Peaudecerf, G. D. Bruce, and S. Kuhr, "Single-atom imaging of fermions in a quantum-gas microscope," *Nature Physics*, vol. 11, pp. 738–742, Sept. 2015.

[75] L. W. Cheuk, M. A. Nichols, M. Okan, T. Gersdorf, V. V. Ramasesh, W. S. Bakr, T. Lompe, and M. W. Zwierlein, "Quantum-Gas Microscope for Fermionic Atoms," *Physical Review Letters*, vol. 114, p. 193001, May 2015.

[76] G. J. A. Edge, R. Anderson, D. Jervis, D. C. McKay, R. Day, S. Trotzky, and J. H. Thywissen, "Imaging and addressing of individual fermionic atoms in an optical lattice," *Physical Review A*, vol. 92, p. 063406, Dec. 2015.

[77] M. F. Parsons, F. Huber, A. Mazurenko, C. S. Chiu, W. Setiawan, K. Wooley-Brown, S. Blatt, and M. Greiner, "Site-Resolved Imaging of Fermionic $^{6}\mathrm{Li}$ in an Optical Lattice," *Physical Review Letters*, vol. 114, p. 213002, May 2015.

[78] J. Drewes, E. Cocchi, L. Miller, C. Chan, D. Pertot, F. Brennecke, and M. Köhl, "Thermodynamics versus local density fluctuations in the metal–mott-insulator crossover," *Physical Review Letters*, vol. 117, no. 13, p. 135301, 2016.

[79] A. Omran, M. Boll, T. A. Hilker, K. Kleinlein, G. Salomon, I. Bloch, and C. Gross, "Microscopic Observation of Pauli Blocking in Degenerate Fermionic Lattice Gases," *Physical Review Letters*, vol. 115, p. 263001, Dec. 2015.

[80] D. Greif, M. F. Parsons, A. Mazurenko, C. S. Chiu, S. Blatt, F. Huber, G. Ji, and M. Greiner, "Site-resolved imaging of a fermionic Mott insulator," *Science*, vol. 351, pp. 953–957, Feb. 2016.

[81] L. W. Cheuk, M. A. Nichols, K. R. Lawrence, M. Okan, H. Zhang, and M. W. Zwierlein, "Observation of 2d fermionic mott insulators of ^{40}K with single-site resolution," *Physical Review Letters*, vol. 116, p. 235301, Jun 2016.

[82] M. Boll, T. A. Hilker, G. Salomon, A. Omran, J. Nespolo, L. Pollet, I. Bloch, and C. Gross, "Spin-and density-resolved microscopy of antiferromagnetic correlations in fermi-hubbard chains," *Science*, vol. 353, no. 6305, pp. 1257–1260, 2016.

[83] A. Omran, *A microscope for Fermi gases*. PhD thesis, May 2016.

[84] A. Georges, "Condensed-matter physics with light and atoms," *Proceedings of the International School of Physics "Enrico Fermi," Course CLXIV, Varenna*, 2006.

[85] T. Esslinger, "Fermi-Hubbard Physics with Atoms in an Optical Lattice," *Annual Review of Condensed Matter Physics*, vol. 1, pp. 129–152, Aug. 2010.

[86] A. Auerbach, *Interacting Electrons and Quantum Magnetism*. Springer Science & Business Media, Jan. 1994.

[87] P. W. Anderson, "Antiferromagnetism. theory of superexchange interaction," *Physical Review Letters*, vol. 79, pp. 350–356, Jul 1950.

[88] T. Giamarchi, *Quantum Physics in One Dimension*. Clarendon Press, 2004.

[89] D. C. Mattis, *The Many-Body Problem: An Encyclopedia of Exactly Solved Models in One Dimension (3rd Printing with Revisions and Corrections)*. World Scientific, 1993.

[90] I. Bloch, J. Dalibard, and W. Zwerger, "Many-body physics with ultracold gases," *Reviews of Modern Physics*, vol. 80, p. 885, July 2008.

[91] N. W. Ashcroft, "Nd mermin solid state physics," *Saunders College, Philadelphia*, p. 120, 1976.

[92] J. Weiner, V. S. Bagnato, S. Zilio, and P. S. Julienne, "Experiments and theory in cold and ultracold collisions," *Reviews of Modern Physics*, vol. 71, no. 1, p. 1, 1999.

[93] W. Hofstetter, J. I. Cirac, P. Zoller, E. Demler, and M. D. Lukin, "High-Temperature Superfluidity of Fermionic Atoms in Optical Lattices," *Physical Review Letters*, vol. 89, p. 220407, Nov. 2002.

[94] A. Klein and D. Jaksch, "Simulating high-temperature superconductivity model hamiltonians with atoms in optical lattices," *Physical Review A*, vol. 73, no. 5, p. 053613, 2006.

[95] F. Bloch, "Quantum mechanics of electrons in crystal lattices," *Z. Phys*, vol. 52, pp. 555–600, 1928.

[96] L. D. Landau, E. M. Lifshitz, J. Sykes, J. S. Bell, and M. Rose, "Quantum mechanics, non-relativistic theory," *Physics Today*, vol. 11, p. 56, 1958.

[97] E. Kozik, E. Burovski, V. W. Scarola, and M. Troyer, "Néel temperature and thermodynamics of the half-filled three-dimensional hubbard model by diagrammatic determinant monte carlo," *Phys. Rev. B*, vol. 87, p. 205102, May 2013.

[98] J. Sethna, *Statistical mechanics: entropy, order parameters, and complexity*, vol. 14. Oxford University Press, 2006.

[99] U. Schneider, *Interacting fermionic atoms in optical lattices-A quantum simulator for condensed matter physics*. PhD thesis, Johannes Gutenberg-Universität Mainz, 2010.

[100] S. Taie, R. Yamazaki, S. Sugawa, and Y. Takahashi, "An su (6) mott insulator of an atomic fermi gas realized by large-spin pomeranchuk cooling," *Nature Physics*, vol. 8, no. 11, pp. 825–830, 2012.

[101] T.-L. Ho and Q. Zhou, "Squeezing out the entropy of fermions in optical lattices," *Proceedings of the National Academy of Sciences*, vol. 106, no. 17, pp. 6916–6920, 2009.

[102] D. McKay and B. DeMarco, "Cooling in strongly correlated optical lattices: prospects and challenges," *Reports on Progress in Physics*, vol. 74, no. 5, p. 054401, 2011.

[103] A. Ho, M. Cazalilla, and T. Giamarchi, "Quantum simulation of the hubbard model: The attractive route," *Physical Review A*, vol. 79, no. 3, p. 033620, 2009.

[104] L. Hackermuller, U. Schneider, M. Moreno-Cardoner, T. Kitagawa, T. Best, S. Will, E. Demler, E. Altman, I. Bloch, and B. Paredes, "Anomalous Expansion of Attractively Interacting Fermionic Atoms in an Optical Lattice," *Science*, vol. 327, pp. 1621–1624, Mar. 2010.

[105] A. L. Gaunt, T. F. Schmidutz, I. Gotlibovych, R. P. Smith, and Z. Hadzibabic, "Bose-einstein condensation of atoms in a uniform potential," *Physical review letters*, vol. 110, no. 20, p. 200406, 2013.

[106] Y. Nagaoka, "Ferromagnetism in a narrow, almost half-filled s band," *Physical Review Letters*, vol. 147, pp. 392–405, Jul 1966.

[107] A. Auerbach and B. E. Larson, "Small-polaron theory of doped antiferromagnets," *Physical review letters*, vol. 66, no. 17, p. 2262, 1991.

[108] J. Spalek, "t-j model then and now: a personal perspective from the pioneering times," *arXiv preprint arXiv:0706.4236*, 2007.

[109] E. Lieb and F. Wu, "Absence of Mott Transition in an Exact Solution of the Short-Range, One-Band Model in One Dimension," *Physical Review Letters*, vol. 20, pp. 1445–1448, June 1968.

[110] C. Kim, A. Matsuura, Z.-X. Shen, N. Motoyama, H. Eisaki, S. Uchida, T. Tohyama, and S. Maekawa, "Observation of spin-charge separation in one-dimensional srcu o 2," *Physical review letters*, vol. 77, no. 19, p. 4054, 1996.

[111] S.-i. Tomonaga, "Remarks on bloch's method of sound waves applied to many-fermion problems," *Progress of Theoretical Physics*, vol. 5, no. 4, pp. 544–569, 1950.

[112] D. C. Mattis and E. H. Lieb, "Exact solution of a many-fermion system and its associated boson field," *Journal of Mathematical Physics*, vol. 6, no. 2, pp. 304–312, 1965.

[113] F. Haldane, "'luttinger liquid theory of one dimensional quantum fluids'," *Journal of Physics C: Solid state physics*, vol. 14, no. 19, p. 2585, 1981.

[114] N. D. Mermin and H. Wagner, "Absence of ferromagnetism or antiferromagnetism in one- or two-dimensional isotropic heisenberg models," *Physical Review Letters*, vol. 17, pp. 1133–1136, Nov 1966.

[115] J. Sirker and A. Klümper, "Thermodynamics and crossover phenomena in the correlation lengths of the one-dimensional t-j model," *Physical Review B*, vol. 66, p. 245102, Dec. 2002.

[116] F. H. L. Essler, H. Frahm, F. Göhmann, A. Klümper, and V. E. Korepin, *The One-Dimensional Hubbard Model*. Cambridge University Press, Feb. 2005.

[117] M. W. Ketterle, Wolfgang und Zwierlein, "Making, probing and understanding ultracold fermi gases," *arXiv preprint arXiv:0801.2500*, 2008.

[118] M. Rigol and A. Muramatsu, "Quantum monte carlo study of confined fermions in one-dimensional optical lattices," *Phys. Rev. A*, vol. 69, 2004.

[119] E. V. Gorelik, D. Rost, T. Paiva, R. Scalettar, A. Klümper, and N. Blümer, "Universal probes for antiferromagnetic correlations and entropy in cold fermions on optical lattices," *Physical Review A*, vol. 85, p. 061602, June 2012.

[120] B. Sciolla, A. Tokuno, S. Uchino, P. Barmettler, T. Giamarchi, and C. Kollath, "Competition of spin and charge excitations in the one-dimensional Hubbard model," *Physical Review A*, vol. 88, p. 063629, Dec. 2013.

[121] T. Paiva, R. Scalettar, M. Randeria, and N. Trivedi, "Fermions in 2d Optical Lattices: Temperature and Entropy Scales for Observing Antiferromagnetism and Superfluidity," *Physical Review Letters*, vol. 104, p. 066406, Feb. 2010.

[122] F. Werner, O. Parcollet, A. Georges, and S. R. Hassan, "Interaction-Induced Adiabatic Cooling and Antiferromagnetism of Cold Fermions in Optical Lattices," *Physical Review Letters*, vol. 95, p. 056401, July 2005.

[123] G. Zürn, T. Lompe, A. Wenz, S. Jochim, P. Julienne, and J. Hutson, "Precise Characterization of Li6˜Feshbach Resonances Using Trap-Sideband-Resolved RF Spectroscopy of Weakly Bound Molecules," *Physical Review Letters*, vol. 110, p. 135301, Mar. 2013.

[124] E. L. Hazlett, Y. Zhang, R. W. Stites, and K. M. O'Hara, "Realization of a resonant fermi gas with a large effective range," *Physical Review Letters*, vol. 108, p. 045304, Jan 2012.

[125] J. Wong-Campos, K. Johnson, B. Neyenhuis, J. Mizrahi, and C. Monroe, "High resolution adaptive imaging of a single atom," *Nature Photonics*, vol. 10, 2016.

[126] M. Lohse, "Large-spacing optical lattice from many-body physics with degenerate quantum gases," Master's thesis, 2012.

[127] N. Bobroff, "Residual errors in laser interferometry from air turbulence and nonlinearity," *Applied optics*, vol. 26, no. 13, pp. 2676–2682, 1987.

[128] J. Levinsen, M. Parish, *et al.*, "Strongly interacting two-dimensional fermi gases," *Annual Review of Cold Atoms and Molecules: Volume 3*, vol. 3, p. 1, 2015.

[129] D. Petrov and G. Shlyapnikov, "Interatomic collisions in a tightly confined bose gas," *Physical Review A*, vol. 64, no. 1, p. 012706, 2001.

[130] V. Makhalov, K. Martiyanov, and A. Turlapov, "Ground-state pressure of quasi-2d fermi and bose gases," *Physical review letters*, vol. 112, no. 4, p. 045301, 2014.

[131] M. E. Gehm, K. M. O'Hara, T. A. Savard, and J. E. Thomas, "Dynamics of noise-induced heating in atom traps," *Phys. Rev. A*, vol. 58, pp. 3914–3921, Nov 1998.

[132] F. Heidrich-Meisner, S. R. Manmana, M. Rigol, A. Muramatsu, A. E. Feiguin, and E. Dagotto, "Quantum distillation: Dynamical generation of low-entropy states of strongly correlated fermions in an optical lattice," *Phys. Rev. A*, vol. 80, p. 041603, Oct 2009.

[133] H. Moritz, T. Stöferle, M. Köhl, and T. Esslinger, "Exciting collective oscillations in a trapped 1d gas," *Physical review letters*, vol. 91, no. 25, p. 250402, 2003.

[134] C. Kollath, A. Iucci, I. McCulloch, and T. Giamarchi, "Modulation spectroscopy with ultracold fermions in an optical lattice," *Physical Review A*, vol. 74, no. 4, p. 041604, 2006.

[135] C. H. Townes and A. L. Schawlow, *Microwave spectroscopy*. Courier Corporation, 2013.

[136] U. Bissbort, *Dynamical effects and disorder in ultracold bosonic matter*. PhD thesis, 2013.

[137] H. P. Büchler, "Microscopic derivation of hubbard parameters for cold atomic gases," *Physical Review Letters*, vol. 104, p. 090402, Mar 2010.

[138] L. W. Cheuk, M. A. Nichols, K. R. Lawrence, M. Okan, H. Zhang, E. Khatami, N. Trivedi, T. Paiva, M. Rigol, and M. W. Zwierlein, "Observation of spatial charge and spin correlations in the 2d fermi-hubbard model," *Science*, vol. 353, no. 6305, pp. 1260–1264, 2016.

[139] Y. Patil, S. Chakram, L. Aycock, and M. Vengalattore, "Nondestructive imaging of an ultracold lattice gas," *Physical Review A*, vol. 90, no. 3, p. 033422, 2014.

[140] B. J. Lester, A. M. Kaufman, and C. A. Regal, "Raman cooling imaging: Detecting single atoms near their ground state of motion," *Physical Review A*, vol. 90, no. 1, p. 011804, 2014.

[141] D. S. C. Biggs and M. Andrews, "Acceleration of iterative image restoration algorithms," *Applied Optics*, vol. 36, pp. 1766–1775, Mar 1997.

[142] M. F. Parsons, A. Mazurenko, C. S. Chiu, G. Ji, D. Greif, and M. Greiner, "Site-resolved measurement of the spin-correlation function in the fermi-hubbard model," *Science*, vol. 353, no. 6305, pp. 1253–1256, 2016.

[143] L. Landau, "Physik z. sowjetunion 2, 46 (1932); c. zener," vol. 137, p. 696, 1932.

[144] V. Malinovsky and J. Krause, "General theory of population transfer by adiabatic rapid passage with intense, chirped laser pulses," *The European Physical Journal D-Atomic, Molecular, Optical and Plasma Physics*, vol. 14, no. 2, pp. 147–155, 2001.

[145] W. Gerlach and O. Stern, "Der experimentelle nachweis der richtungsquantelung im magnetfeld," *Zeitschrift für Physik A Hadrons and Nuclei*, vol. 9, no. 1, pp. 349–352, 1922.

[146] D. Greif, G. Jotzu, M. Messer, R. Desbuquois, and T. Esslinger, "Formation and Dynamics of Antiferromagnetic Correlations in Tunable Optical Lattices," *Physical Review Letters*, vol. 115, p. 260401, Dec. 2015.

[147] N. Gemelke, X. Zhang, C.-L. Hung, and C. Chin, "In situ observation of incompressible mott-insulating domains in ultracold atomic gases," *Nature*, vol. 460, no. 7258, pp. 995–998, 2009.

[148] R. Jördens, L. Tarruell, D. Greif, T. Uehlinger, N. Strohmaier, H. Moritz, T. Esslinger, L. De Leo, C. Kollath, A. Georges, V. Scarola, L. Pollet, E. Burovski, E. Kozik, and M. Troyer, "Quantitative Determination of Temperature in the Approach to Magnetic Order of Ultracold Fermions in an Optical Lattice," *Physical Review Letters*, vol. 104, p. 180401, May 2010.

[149] J.-S. Bernier, C. Kollath, A. Georges, L. De Leo, F. Gerbier, C. Salomon, and M. Köhl, "Cooling fermionic atoms in optical lattices by shaping the confinement," *Physical Review A*, vol. 79, p. 061601, June 2009.

[150] M. Lubasch, V. Murg, U. Schneider, J. I. Cirac, and M.-C. Bañuls, "Adiabatic Preparation of a Heisenberg Antiferromagnet Using an Optical Superlattice," *Physical Review Letters*, vol. 107, p. 165301, Oct. 2011.

[151] I. Affleck, T. Kennedy, E. H. Lieb, and H. Tasaki, "Rigorous results on valence-bond ground states in antiferromagnets," *Physical Review Letters*, vol. 59, pp. 799–802, Aug 1987.

[152] T. Fukuhara, A. Kantian, M. Endres, M. Cheneau, P. Schauß, S. Hild, D. Bellem, U. Schollwock, T. Giamarchi, C. Gross, I. Bloch, and S. Kuhr, "Quantum dynamics of a mobile spin impurity," *Nature Physics*, vol. 9, p. 235, Apr. 2013.

[153] T. Fukuhara, P. Schauß, M. Endres, S. Hild, M. Cheneau, I. Bloch, and C. Gross, "Microscopic observation of magnon bound states and their dynamics," *Nature*, vol. 502, no. 7469, p. 76, 2013.

[154] P. Jordan and E. Wigner, "About the pauli exclusion principle," *Zeitschrift für Physik*, vol. 47, pp. 631–651, Feb 1928.

[155] N. V. Prokof'ev, B. V. Svistunov, and I. S. Tupitsyn, "Exact, complete, and universal continuous-time worldline monte carlo approach to the statistics of discrete quantum systems," *Journal of Experimental and Theoretical Physics*, vol. 87, no. 2, pp. 310–321, 1998.

[156] L. Pollet, K. V. Houcke, and S. M. Rombouts, "Engineering local optimality in quantum monte carlo algorithms," *Journal of Computational Physics*, vol. 225, no. 2, pp. 2249 – 2266, 2007.

[157] K.-K. Pan and Y.-L. Wang, "Magnetic susceptibility of the strongly correlated hubbard model," *Physical Review B*, vol. 43, pp. 3706–3709, Feb 1991.

Danksagung

An erster Stelle danke ich meinem Doktorvater Prof. Immanuel Bloch dafür, dass er mir die Möglichkeit gegeben hat, in dessen Forschungsgruppe diese Promotion anfertigen zu dürfen. Seine Begeisterung für das Forschungsfeld spürte ich bereits während der ersten Vorlesung in Mainz, die ich bei Ihm hören durfte und dieser Enthuisiasmus ist bis heute ungebrochen. Vielen Dank für den Vetrauensvorschuss, der mir als Doktoranden mit dem Auftrag zum Erstellen des *Quantengasmikroskops*, zu Teil wurde. Nicht minder wichtig war die direktere Betreuung durch meinen Experimentleiter Dr. Christian Gross. Durch seine *hands-on* Mentalität habe ich sehr viel innerhalb und außerhalb des Labors lernen und bewegen können. Er bat mir in jeglichen Situationen ein offenes Ohr und stand mit Rat und Verständnis zur Seite.
Meinen direkten Laborkollegen, Ahmed Omran, Timon Hilker und Guillaume Salomon. Wir haben zusammen alle Höhen und Tiefen während des Aufbaus des Experiments durchgemacht. Alle drei sind exzellente Physiker und darüberhinaus, aus meiner Sicht noch viel wichtiger, sehr hilfsbereite und gute Jungs. Es war mir immer eine Freude mit euch zusammenzuarbeiten. Den weiteren Personen, die bei der erfolgreichen Umsetzung des Experiments mitgewirkt haben: Michael Lohse, Thomas Gantner, Konrad Viebahn, Leo Stenzel, Thomas Reimann und Katharina Kleinlein. Besonderer Dank gilt den Personen im Hintergrund, die unsere Arbeit technisch oder administrativ ermöglichen. Kristina Schuldt, Ildiko Keskesi, Anton Meyer, Karsten Förster und Oliver Mödl. Danke für euren Einsatz, der weit über den 'Dienst nach Vorschrift' hinaus geht.
Meinen Eltern,Großeltern und Schwiegereltern, die in jeder Situation an mich geglaubt haben und durch ihre Unterstützung überhaupt erst die Anfertigung einer Doktorarbeit ermöglicht haben. Ich wusste das immer zu schätzen und bin froh, dass es euch alle gibt. Meinen Freunden, die mich auch in Zeiten in denen es am Experiment mal nicht so lief, erheitert haben. Hervorzuheben sei hier mein Freund und ehmaliger Mitbewohner Nikolaus Buchheim. Danke für deine Hilfe, unsere Bergtouren und die überaus delikaten Menüs und Weine am Abend. Der Gruppe '*Munich mountaineering*' für unsere unzähligen Erlebnisse am Berg, sowie Guillaume Salomon für's Mitnehmen zum klettern.
Der größte Dank gilt jedoch meiner Frau Hannah. Du bist die Liebe meines Lebens. Danke für Alles.